DOCTOR OF PHILOSOPHY

The Application of Pulsed Electron Paramagnetic Resonance to the Investigation of Protein Structure

Stevens, Michael

Award date:
2018

The Application of Pulsed Electron Paramagnetic Resonance to the Investigation of Protein Structure.

By Michael Andrew Stevens

Supervisor: Dr David Norman

A thesis submitted for the Degree of Doctor of Philosophy in the School of Life Sciences

University of Dundee

March 2018

Contents

List of Figures

Declaration

Students Declaration:

I hereby declare that this thesis is the authors' own work and has not been previously submitted for any other higher degree. In cases where the work has been performed in collaboration the authors contribution has been specified and other parties involved have been acknowledged.

Michael Stevens

Signed:

Supervisors Declaration:

I declare that Michael Stevens has fulfilled the conditions of Ordinance General No. 39 of the University of Dundee and is qualified to submit the accompanying thesis in application for the degree of Doctor of Philosophy.

David Norman

Signed:

Acknowledgements

The author would like to thank Dr Johannes McKay, Dr Ramasubramanian Sundaramoorthy and James Robinson for their contributions in determining the orientation of the spin label Rx with respect to the protein structure of Vps 75; Professor Tom Owen Hughes (Vps 75), Dr Owen Pornillos (Trim 25 and MuRF 1), Dr Barbara Franke and Dr Olga Mayans (both MuRF 1) for providing plasmids for the given protein constructs; Dr Alasdair D. J. Freeman, Katherine Mackay, Adam Leahy, Dr Anne Cecile Declais and Professor David Lilly for their work on the Endo 1 project; Dr Graham Smith and Dr Hassane El Mkami for help in running PELDOR experiments; and Dr David Norman for supervising all the projects presented here. More personally I would like to thank my parents and Elaine Mitchell for being there when I needed them.

Publications

Stevens, M.A., McKay, J.E., Robinson, J.L.S., Mkami, H.E., Smith, G.M., and Norman, D.G. (2016). The Use of the Rx Spin Label in Orientation Measurement on Proteins, by EPR. Phys. Chem. Chem. Phys. *18*, 5799–5806.

Freeman, A.D.J., Stevens, M., Declais, A.-C., Leahy, A., Mackay, K., El Mkami, H., Lilley, D.M.J., and Norman, D.G. (2016). Analysis of the Intrinsically Disordered N-Terminus of the DNA Junction-Resolving Enzyme T7 Endonuclease I: Identification of Structure Formed upon DNA Binding. Biochemistry (Mosc.) *55*, 4166–4172.

Abstract

Pulsed electron-electron double resonance (PELDOR) is a pulsed electron paramagnetic resonance (pulsed EPR) technique used for measuring distances and on rare occasions orientations within biomolecular structures. Site directed spin labelling (SDSL) has provided a method for introducing EPR active species into protein structures, the majority of these species are too flexible for the use of orientation measurements unless their introduced into sites that restrict the motion of the label. Additionally the quality of information gathered by PELDOR is dependent on the signals strength and persistence, with deuteration of both the underlying protein structure and surrounding media found to increase both the signal intensity and persistence. Within this thesis the current use of PELDOR for investigating disordered areas of protein structure along with the orientation of homodimeric domains has been demonstrated, followed by investigations into determining the extent of the increase in distance available upon deuteration of the protein backbone and the possibility of using a bifunctional spin label for making orientation measurements within protein structures.

Within this thesis chapters 1 and 2 give an introduction into the theory behind EPR. Chapter 1 introduces a brief theoretical background behind EPR and chapter 2 introduces the use of EPR for protein structure determination. Chapter 3 outlines the methods used to produce the data in chapters 4 to 7, and chapter 8 gives the overall conclusions from the thesis. The projects presented here introduce some of the current applications of EPR into structural biology (chapters 4 and 5) along

with advancements in sample preparation that allow a greater quantity of data to be collected (chapters 6 and 7).

Chapter 4 introduces the use of EPR for determining the probable binding location and intrinsically disordered structure formed by the first 16 N-terminal residues of endonuclease I (Endo I). It concludes with the proposal that residues 10 to 16 are involved in stabilising the binding of Endo I to the four-way DNA junction; and residues 1 to 10 form an intrinsically disordered helical structure that is stabilised upon binding DNA. In chapter 5 PELDOR was used to determine whether the coiled coil region of the tripartite motif (Trim) protein family member muscle regulation factor 1 (MuRF 1) formed a parallel or anti-parallel coiled coil. The pattern of distances from the various different labelled sites found the coiled coil region adopted an anti-parallel conformation, with comparisons between distance distributions from PELDOR and the homology model giving evidence that the anti-parallel homo-dimer was in a similar conformation to crystal structures of other Trim family member coiled coil regions.

Chapter 6 used a fully deuterated coiled coil region of tripartite motif family member 25 (Trim 25) to determine the effect of label-to-label distance upon the decay in the PELDOR echo. There were no significant effects of protein deuteration upon PELDOR measurements, however discrepancies found between distances from the crystal and PELDOR structure for the coiled coil region of Trim 25, which may suggest a difference in the coiling of the protein between the crystal and solution structures.

Chapter 7 uses vacuolar protein sorting-associated protein 75 (Vps 75) as a model protein structure for determining the most effective binding site for the bifunctional spin label Rx to make orientation measurements using PELDOR. It was found that binding Rx between i and i+1 on the α-helix allowed the spin label to produce a monomodal distribution allowing the site to be used for orientation measurements. In addition when bound from i to i+1 the bulk of the buttressing residues at i±3/4 have significant effects on the labels motion with the C-terminal buttressing residue having the greatest affect on the distribution of Rx.

Chapter 8 concludes the thesis, illustrating the current use of EPR within structural biology and the future prospects of the technique based upon the findings within this thesis. These prospects involve the use of orientation data in structural refinement, and the development of what information can be obtained from protein deuteration.

Chapter 1: Introduction to Electron Paramagnetic Resonance (EPR)

1.0 Summary

This chapter contains an introduction to electron paramagnetic resonance (EPR) in a historical context, covering the origins of the technique along with its application to structural biology. This introduction is followed by a brief theoretical description of the underpinning processes behind EPR, along with the experimental techniques used within this thesis. These experimental techniques include: continuous wave EPR; Tm measurements and pulsed electron-electron double resonance (PELDOR). The description within this chapter only provides a brief introduction to the theory behind EPR. For further understanding of the concepts underpinning EPR introduced within this chapter the texts "Principles of pulse electron paramagnetic resonance" (Schweiger and Jeschke, 2001) and "Electron Paramagnetic Resonance: Elementary Theory and Applications" (Weil and Bolton, 2007) are recommended.

1.1 Introduction

High-resolution techniques such as X-ray crystallography (Helliwell, 1984), cryogenic electron microscopy (cryo-EM) (Bartesaghi et al., 2014; Liao et al., 2013) and nuclear magnetic resonance (NMR) (Cavalli et al., 2007) can provide clear and unambiguous pictures of large biomolecules. There are however limitations to these techniques which can result in structural artefacts (Søndergaard et al., 2009), partial structures (D'Cruz et al., 2013; Sanchez et al., 2014) or indeed no structures at all. It is often the case that a number of complementary structural techniques must be used to build up a more complete and accurate picture of biomolecular structures (Perrakis et al., 1999; Schwieters et al., 2003). It is also

the case that some biomolecules do not exist as homogeneous structural entities, such that, lower resolution techniques must be used to extract useful information (Putnam et al., 2007).

1.1.1 EPR Introduction

The two most popular electron paramagnetic resonance (EPR) methods used for elucidating biological structures are continuous wave electron paramagnetic resonance (CW-EPR) and pulsed electron-electron double resonance (PELDOR) (Borbat et al., 2001; Jeschke and Polyhach, 2007). In the majority of cases, these techniques require the use of a spin label, i.e. a molecule containing an unpaired electron and a binding affinity to a specific site on a biomolecule (Hubbell et al., 2013).

CW-EPR is an esoteric technique where a myriad of factors can contribute to the spectral line shape including the mobility of the spin label, the spin label's environment and the solution temperature (Du et al., 1995). PELDOR is used to determine distance distributions between spin labels, although, it is difficult to extract distance distributions from raw data. The formulation of computational methods created a platform for the accessible analysis of raw PELDOR data (Jeschke, 2002; Jeschke et al., 2006). These computational methods include programs such as DeerAnalysis and MTSL-Wizard. DeerAnalysis extracts accurate distance distributions from raw PELDOR data using Tikhonov regularisation (Jeschke et al., 2006). MTSL-Wizard, (a plugin for pymol), produces a rotamer library of commonly used labels, allowing label distribution with respect to the protein backbone to be predicted with reasonable accuracy (Hagelueken et al., 2012).

1.1.2 EPR in Structural Biology

The information that can be obtained by CW-EPR and PELDOR renders the techniques useful in: piecing together structures defined using other techniques (Hammond et al., 2014); providing information on unresolved structural areas within known protein structures (Ward et al., 2009a); and revealing conformational changes within the protein structure (Mchaourab et al., 2011). A key secondary purpose of both CW-EPR and PELDOR is to either validate an existing theoretical model, or hypothesise conformations of intrinsic structures within a protein system (for example chapters 4 and 5 of this thesis). This versatility, along with the development of spin labelling as a simple to use technique, makes EPR ideal for answering specific questions within structural biology, particularly regarding the study of intrinsically disordered areas of protein structures and multimeric complexes. To increase the resolution of both CW-EPR and PELDOR, a series of different rigid spin labels have been developed. Additional increases in sensitivity of PELDOR experiments have been observed by exchanging protons within a sample to deuterons. Running PELDOR in a deuterated solvent has become commonplace for biological samples (Lindgren et al., 1997), with recent studies showing a further significant increases in resolution following deuteration of the underlying protein (El Mkami et al., 2014; Schmidt et al., 2016).

1.1.3 Thesis Layout

The layout of this thesis is as follows:

Chapters one and two present a brief introduction to the theory underlying the techniques used in this thesis.

Chapter three presents the experimental methods used for acquiring and analysing data.

The application of EPR to investigate biological questions arising from either disordered protein structures or unusual protein structural conformations are discussed in chapters four and five respectively.

Chapter six contains investigations into sample improvements that increased the quality and quantity of PELDOR data using protein deuteration.

Chapter seven investigates using a rigid spin label to develop a generic method for orientation measurements within protein structures.

Chapter eight presents an overall conclusion of the successes and shortcomings of the investigations within this thesis. A short summary of future work is also given.

It is hoped that this thesis demonstrates some of the current applications of EPR to answering biological questions. Moreover, it is hoped that this thesis raises awareness of technique improvement, from the standpoint of sample preparation.

1.2 A Brief History of EPR

Early developments in electron paramagnetic resonance (EPR) were far removed from the investigation of biomolecular structures. EPR was first discovered by the physicists Gerlach and Stern. Gerlach and Stern conducted a series of experiments that showed the spatial nature of angular momentum by the splitting of a beam of silver atoms into two when introduced to a inhomogeneous magnetic field (Gerlach and Stern, 1922a, 1922b, 1922c; Schmidt-Böcking et al., 2016). The splitting of silver atoms into two distinct populations, demonstrated the electron possesses an intrinsic, quantized magnetic moment. The inhomogeneity within the magnetic field caused the electrons (possessing the discrete quantized magnetizations) to migrate towards different magnetic poles (Schmidt-Böcking et

al., 2016). A series of different and repeated experiments of the same sort followed in order to identify the nature of this splitting-the main theoretical breakthrough being the idea of spin as an intrinsic property of a particle (Pauli, 1940). In 1939, Isidor Rabi made the first discovery of resonance frequencies in nuclear magnetic resonance (NMR). The experiment entailed a beam of hydrogen atoms being diverted using electromagnetic radiation in a narrow region of radio wave frequencies (Rabi et al., 1938). The first EPR spectrum was recorded by the Russian physicist Zavoisky in 1944 (Salikhov and Zavoiskaya, 2015; Zavoisky, 1945) one year before the first NMR spectra was recorded by Bloch et al. (Bloch et al., 1946). Despite both techniques being based upon similar theoretical concepts, the uses of NMR and EPR diverged with the discovery of the chemical shift in NMR. This allowed the regular use of NMR to solve structures of small chemical compounds. EPR, although proving extremely useful in certain circumstances, did not gain the widespread application seen for NMR due to the requirement of the presence of unpaired electrons (Bagguley and Griffiths, 1947; Gordy et al., 1955).

It can be argued, structural biology began with the proposition of the DNA double helix structure in a series of articles in 1953, specifically demonstrating the use of X-ray diffraction to reveal the molecular structure (Franklin and Gosling, 1953; Watson and Crick, 1953; Wilkins et al., 1953). X-ray crystallography was the technique used to solve the first protein structure i.e. myoglobin. X-ray diffraction has remained the gold standard for techniques used in structural biology due to the high resolution structures it can produce (Kendrew et al., 1958). NMR needed jumps in technology to higher magnetic fields, to increase sensitivity and shift dispersion. NMR also needed the development of pulsed techniques, to allow its use on more complicated molecules than before (Becker, 1993). Despite the

dominance of X-ray crystallography and NMR, there has always been a need for structural information not available to these techniques. For instance, crystallization is always a potential stumbling block for X-ray diffraction (McPherson and Gavira, 2014) and NMR has run up against limitations due to the restriction on the size of molecules that can be studied in detail, although, advancements in solid state NMR have sought to rectify this (Mainz et al., 2013). Alternative methods have been developed to increase the armoury of structural biology techniques (Cowieson et al., 2008). These included techniques such as EPR, fluorescence, and mass spectrometry.

In biology, EPR began as a continuous wave technique used to find the local environment of free radicals within the protein structure (Commoner et al., 1954; Gordy et al., 1955). Its use was expanded due to the availability of microwave sources developed during the Second World War for radar. The observation of the first pulsed EPR experiment led to the possibility of a range of new techniques being developed (Blume, 1958). The main limitation for development was the lack of commercial spectrometers and the expense of pulsed microwave components (Becker, 1993; Junk, 2012). This left only a few groups to develop pulsed EPR as a technique, such as, the group of W. B. Mims who performed the first electron spin echo envelope (ESEEM) (Mims et al., 1961) and the first pulsed electron nuclear double resonance (ENDOR) (Mims, 1965) experiments. The first commercially available pulsed EPR spectrometers were developed in the late 1980s, expanding the availability of EPR and increasing its use (Schmalbein, 1987).

Chemical modification of proteins can be said to have started with the tanning and dyeing industry, such as, the use of formaldehyde or Coomassie staining. As the

knowledge of amino acid structures advanced, there became a need to specifically target certain amino acids and determine how they affected protein function (Means and Feeney, 1990). This development of chemistries to react with specific amino acids, would prove important to the application of EPR and fluorescence techniques to structure determination. Spin labels: stable free radicals designed to associate with a protein in a specific manner, opened systems containing no natural free radicals to investigation using EPR. Spin labels were first used to report on the dynamics of protein (Berliner, 2012). Nitroxide radicals have been used for spin labelling since the 1960s (Burr and Koshland, 1964), however, one of the more significant innovations was the synthesis of the MTSL label in 1982 (Berliner et al., 1982) that is still the most commonly used spin label for biological applications today. It was the development of site directed chemistry that really expanded the use of EPR. With some of the first uses of this technique taking place in the lab of W.L. Hubble in the mid to late 80s (Altenbach et al., 1989; Todd et al., 1989).

The use of site directed mutagenesis, bacterial protein expression and spin labelling opened the protein world to analysis by EPR. Initially, continuous wave EPR (CW-EPR) was used to determine the local environment of spin labels at defined positions on protein structures. The combination of advancements in pulsed microwave techniques, particularly, the development of pulsed electron-electron double resonance (PELDOR), in combination with site directed spin labelling allowed the determination of structural restraints to protein structures. Other advancements in EPR have involved increasing sensitivity i.e. increasing the magnetic field used for EPR (Cruickshank et al., 2009); forming shaped pulses (Doll et al., 2013, 2015; Schöps et al., 2015; Spindler et al., 2012), forming composite

pulses to give a better coverage of the spectrum (Motion et al., 2016) and improvements to pulse sequences used (Breitgoff et al., 2017). Advancements have also been made in sample preparation for example, the use of techniques such as modifications to spin labels to make them more rigid (Hubbell et al., 2013); using alternative spin labels to increase sensitivity (Cunningham et al., 2015; Matalon et al., 2013); allowing measurements to be made under more native conditions; and modification of the sample conditions (El Mkami et al., 2014; Ward et al., 2010; Yong et al., 2001).

1.3 EPR Theory

In this section a brief description of the theory behind EPR is gives. For a more thorough explanation see, 'Principles of Pulse Electron Paramagnetic Resonance' by Arthur Schweiger and Gunnar Jeschke (Schweiger and Jeschke, 2001); and Electron Paramagnetic Resonance: Elementary Theory and Practical Applications by John Weil and James Bolton (Weil and Bolton, 2007).

Spectroscopy describes techniques used to monitor changes between energy levels within a system; in EPR these energy levels are caused by the interaction between an electron's dipole and an external magnetic field. Transitions between energy levels of electrons interacting with magnetic field strengths between 11 mT and 11 T are accompanied by the absorption or emission of electromagnetic radiation in the microwave region (300 MHz to 300 GHz). The interaction between an electron's dipole and the external magnetic field is related to the electron's magnetic moment ($\boldsymbol{\mu}_e$): an intrinsic property of the particle related to the spin

quantum number. The relationship between the electron dipole and a given static external magnetic field $\boldsymbol{B}_0$, is governed by the Hamiltonian operator:

$$\mathcal{H} = \boldsymbol{B}_0 \cdot \boldsymbol{\mu_e} \tag{1.1}$$

The magnetic moment, $\boldsymbol{\mu_e}$, is defined by:

$$\boldsymbol{\mu}_e = \hbar\gamma_e \boldsymbol{S} = g_{\boldsymbol{e}}\beta_e \boldsymbol{S} \tag{1.2}$$

ħ is the reduced Plank constant ($\hbar = \frac{h}{2\pi}$); $g_{\boldsymbol{e}}$ is the electrons g factor, a dimensionless correction factor for conversions between the magnetic moment and angular momentum; γ_e is the ratio between the magnetic moment and the spin angular momentum (the gyromagnetic ratio), defined by $\gamma_e = g_e \frac{e}{2m_e}$ (e is the charge on the electron, and m_e is the electrons mass); β_e is the Bohr magneton, a physical constant defined by $\beta_e = \frac{e\hbar}{2m_e}$; and $\boldsymbol{S}$ is the electron spin operator which can adopt values of $\pm\frac{1}{2}$. Altogether, this gives the electron energy levels of:

$$U = \pm\frac{1}{2} g_e \beta_e B_0 \tag{1.3}$$

Hence, the different energy levels are produced by the electron dipole aligning with or against the external magnetic field (figure 1.1). The resonance condition is the difference between these energy levels, defined by:

$$h\nu = g_e \beta_e B_0 \tag{1.4}$$

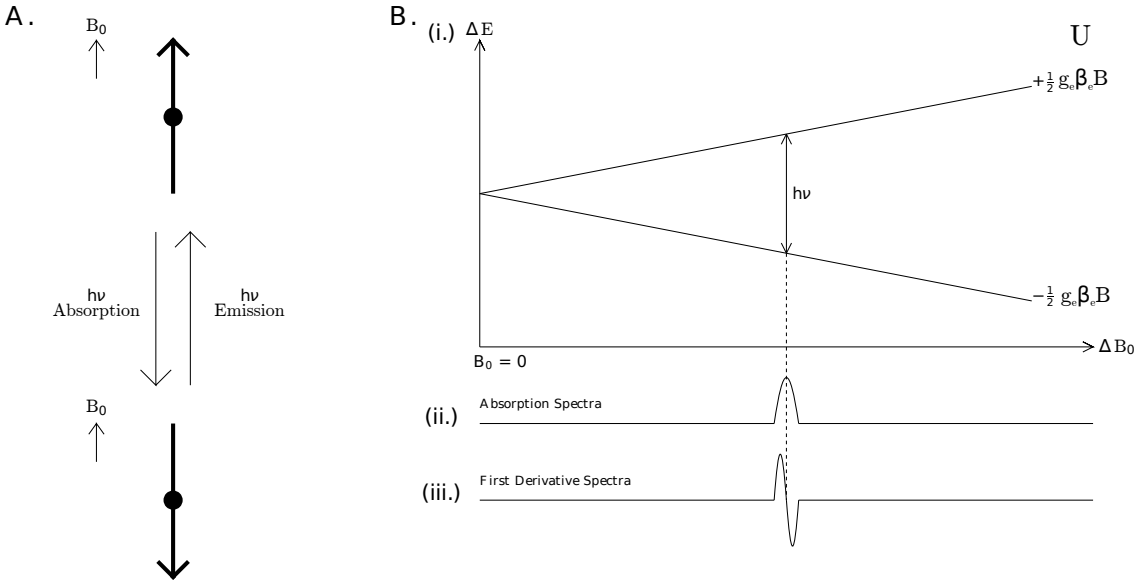

Figure 1.1: An illustration of the different energy levels for an unpaired electron in an external magnetic field (the Zeeman effect). (A) The electron is split into two states, where the z magnetization is aligned with (top) or against (bottom) the external magnetic field. The states exist at a low or high energy level with the absorption or emission of electromagnetic radiation observed upon the magnetization flipping from one state to the other. (B) (i) Energy levels (U) aligned with $(-\frac{1}{2} g_e \beta_e B_0)$ *or counter to* $(+\frac{1}{2} g_e \beta_e B_0)$ *the external magnetic field* (B_0) *against the magnetic field strength. (ii.) If a constant resonating microwave frequency (hν) is applied while the external magnetic field* (B_0) *is scanned, an absorption of electromagnetic radiation is observed when the difference between the two energy levels equals hν. (iii.) The first derivative of the CW-EPR absorption spectra, demonstrating the form an EPR spectra is recorded in.*

1.4 The Electron Spin Systems Hamiltonian Operator

An unpaired electron is seldom present isolated in a vacuum; thus, a series of different terms are added to the Hamiltonian operator that describe these different contributions to the system:

$$\mathcal{H} = \mathcal{H}_{ez} + \mathcal{H}_{nz} + \mathcal{H}_{Q} + \mathcal{H}_{hf} \tag{1.5}$$

The separation of energy levels is now a result of the electron Zeeman interaction ($\mathcal{H}_{ez}$), the nuclear Zeeman interaction ($\mathcal{H}_{nz}$), the nuclear quadrupolar interaction ($\mathcal{H}_{Q}$), and the hyperfine interaction ($\mathcal{H}_{hf}$).

1.4.1 Zeeman Interaction

Zeeman interactions act between a spins magnetic dipole and the external magnetic field; such interactions are described by the magnetic moment of the spin. Zeeman splitting is rarely isotropic, creating situations where anisotropies within the g tensor need to be considered. This anisotropy becomes more prominent as the magnetic field strength is raised. Consequently, the magnetic moment contains a matrix representing different spatial values of g:

$$\boldsymbol{\mu} = \beta_e \, \boldsymbol{g} \cdot \boldsymbol{S} \tag{1.6}$$

where:

$$\boldsymbol{g} = \begin{bmatrix} g_{xx} & g_{xy} & g_{xz} \\ g_{yx} & g_{yy} & g_{yz} \\ g_{zx} & g_{zy} & g_{zz} \end{bmatrix} \tag{1.7}$$

Values within the matrix change based upon the symmetry of the system; in the case of electrons this is due to coupling between to the electrons orbital, described by the symmetry tensor $\boldsymbol{\Lambda}$:

$$\boldsymbol{\Lambda} = \begin{bmatrix} \Lambda_{xx} & \Lambda_{xy} & \Lambda_{xz} \\ \Lambda_{yx} & \Lambda_{yy} & \Lambda_{yz} \\ \Lambda_{zx} & \Lambda_{zy} & \Lambda_{zz} \end{bmatrix} \tag{1.8}$$

Where,

$$\Lambda_{ij} = -\sum_{n \neq G} \frac{\langle n|\boldsymbol{L}_i|O\rangle\langle O|\boldsymbol{L}_j|n\rangle}{U_O^{(0)} - U_n^{(0)}} \tag{1.9}$$

$\boldsymbol{L}_i$ and $\boldsymbol{L}_j$ represent the orbital angular momentum operators, n represents all present orbitals with energy $U_n^{(0)}$ and O represents the singularly occupied orbitals with energy $U_O^{(0)}$. The matrix $\boldsymbol{g}$ can be expressed as:

$$\boldsymbol{g} = g_{iso}\mathbf{1}_3 + 2\lambda\boldsymbol{\Lambda} \tag{1.10}$$

Where g_{iso} is the isotropic g factor, $\mathbf{1}_3$ is a 3x3 unit matrix and λ is the spin-orbit coupling constant. The nitroxide radicals used within this thesis possess a rhombic symmetry in the g anisotropy; consequently, the matrix describing the g anisotropy can be diagonalized to give:

$$\boldsymbol{g} = \begin{bmatrix} g_{xx} & 0 & 0 \\ 0 & g_{yy} & 0 \\ 0 & 0 & g_{zz} \end{bmatrix} \tag{1.11}$$

Using the relevant g matrix. Hamiltonian operators for the electron ($\mathcal{H}_{ez}$) and nuclear ($\mathcal{H}_{nz}$) Zeeman interactions can be represented by:

$$\mathcal{H}_{ez} = \beta_e \boldsymbol{B_0^T} \cdot \boldsymbol{g}_e \cdot \boldsymbol{S} \tag{1.12}$$

$$\mathcal{H}_{nz} = \beta_n \boldsymbol{B_0^T} \cdot \boldsymbol{g}_n \cdot \boldsymbol{I} \tag{1.13}$$

$\boldsymbol{B_0^T}$ is the transposed external magnetic field vector, $\boldsymbol{I}$ is the nuclear spin operator, β_n is the nuclear magneton defined as $\beta_n = \frac{q_n \hbar}{2m_n}$ (q_n is the charge on the nucleus, and m_n is the mass of the nucleus), and $\boldsymbol{g}_e$ or $\boldsymbol{g}_n$ are matrices of g factors for the electron and nucleus respectively.

1.4.2 Hyperfine Coupling

Hyperfine coupling is the interaction between the unpaired electron and nearby nuclei. As with Zeeman Coupling it can be split into an isotropic and anisotropic component, the isotropic interaction is primarily a result of Fermi contact interactions that occur when the unpaired electron and the nucleus occupy the same space. This is present in cases where the unpaired electron density is non-zero at the nucleus. Anisotropic interactions result from electron-nuclear dipolar coupling, this can be further split into an isotropic and anisotropic component, with the different energy levels described by a Hamiltonian operator of the dipolar coupling:

$$\mathcal{H}_d = \frac{\mu_0}{4\pi} g_e \beta_e g_n \beta_n \left[\frac{\boldsymbol{S}^T \cdot \boldsymbol{I}}{r^3} - \frac{3(\boldsymbol{S}^T \cdot \boldsymbol{r})(\boldsymbol{I}^T \cdot \boldsymbol{r})}{r^5} \right] \tag{1.14}$$

For simplicity, the Zeeman splitting is assumed to be isotropic with g_e and g_n representing g factors for the nucleus and electron respectively; μ_0 is the magnetic permeability of the sample; r is the distance between the dipoles; and **r** is the spin-spin vector between the electron and the nearby nucleus. The hyperfine coupling can be simplified and described as:

$$\mathcal{H}_d = \frac{\mu_0}{4\pi} g_e \beta_e g_n \beta_n \boldsymbol{S}^T \cdot \boldsymbol{T} \cdot \boldsymbol{I} \tag{1.15}$$

where:

$$\boldsymbol{T} = \begin{bmatrix} \left\langle \frac{r^2-3x^2}{r^5} \right\rangle & \left\langle -\frac{3xy}{r^5} \right\rangle & \left\langle -\frac{3xz}{r^5} \right\rangle \\ & \left\langle \frac{r^2-3y^2}{r^5} \right\rangle & \left\langle -\frac{3yz}{r^5} \right\rangle \\ & & \left\langle \frac{r^2-3z^2}{r^5} \right\rangle \end{bmatrix} \tag{1.16}$$

The matrix $\boldsymbol{T}$ is symmetrical about its diagonal with $\langle \dots \rangle$ indicating spatial averaging of nucleus-electron vectors within the molecular orbital. Using the matrix $\boldsymbol{T}$, the hyperfine interaction can be defined by the matrix $\boldsymbol{A}$ where:

$$\boldsymbol{A} = A_0 \mathbf{1}_3 + \boldsymbol{T} \tag{1.17}$$

A_0 is the isotropic hyperfine coupling value and $\mathbf{1}_3$ is a 3x3 unit matrix. This allows the hyperfine coupling to be defined by the matrix:

$$\boldsymbol{A} = \begin{bmatrix} A_{xx} & A_{xy} & A_{xz} \\ A_{yx} & A_{yy} & A_{yz} \\ A_{zx} & A_{zy} & A_{zz} \end{bmatrix} \tag{1.18}$$

Like $\boldsymbol{g}$, $\boldsymbol{A}$ can be diagonalised in cases where the coupling is symmetric giving:

$$\boldsymbol{A} = \begin{bmatrix} A_{xx} & 0 & 0 \\ 0 & A_{yy} & 0 \\ 0 & 0 & A_{zz} \end{bmatrix} \tag{1.19}$$

Allowing the hyperfine coupling Hamiltonian to be written as:

$$\mathcal{H}_{hf} = \boldsymbol{S}^T \cdot \boldsymbol{A} \cdot \boldsymbol{I} \tag{1.20}$$

1.4.3 Nuclear Quadrupolar interactions

If the interacting nucleus has a spin over $\frac{1}{2}$, the electrical charge gradient across the nucleus lacks spherical symmetry, which is described by the quadrupolar coupling. If this coupling is within the same magnitude as the hyperfine coupling it affects the spin Hamiltonian. The quadrupolar interaction can be described using the matrix:

$$\boldsymbol{P} = P \begin{bmatrix} \eta - 1 & 0 & 0 \\ & -\eta - 1 & 0 \\ & & 2 \end{bmatrix} \tag{1.21}$$

with η representing the deviation of the magnetic field gradient from uniaxial symmetry and:

$$P = \frac{e^2 q_{efg} Q}{4I(2I-1)} \tag{1.22}$$

$-|e|q_{efg}$ represents the electric field gradient of the largest magnet affecting the nucleus; $|e|Q$ describes the nucleus electrical shape, giving a fixed number for each isotropic species; and I is the nuclear spin operator. The quadrupolar coupling Hamiltonian can then be described by:

$$\mathcal{H}_Q = \boldsymbol{I}^T \cdot \boldsymbol{P} \cdot \boldsymbol{I} \tag{1.23}$$

1.4.4 Relaxation

Relaxation is a key concept in EPR where it describes the process of excited electrons returning to equilibrium. In consideration of the effects and dynamics within a system exposed to an external magnetic field, it is worth defining energy level in terms of the spin temperature (T_S) and the ratio of electron spin numbers in the high energy state, N_{upper}, and the number of electrons in the low energy state, N_{lower}:

$$\frac{N_{upper}}{N_{lower}} = e^{\frac{-\Delta U}{k_B T_S}} \tag{1.24}$$

ΔU is the energy difference between electrons in the upper and lower energy states and k_B is the Boltzmann constant. In an excited system the distribution of electron spins shifts towards the high-energy state, lowering the spin temperature (T_S). This is followed by a relaxation of the system until T_S is equivalent to the temperature of the surroundings (T). Before considering mechanisms of relaxation, it is valuable to consider the electron spin as a magnetic moment

precession about the external magnetic field at the Larmor frequency (ω_l), defined by:

$$\omega_l = \gamma_e \boldsymbol{B}_0 \tag{1.25}$$

where $\boldsymbol{B}_0$ is the external magnetic field and γ_e is the gyromagnetic ratio. For determining relaxation, it is worth considering the bulk magnetization within the sample, described by the vector $\boldsymbol{M}$, with its x, y and z components labelled M_x, M_y, and M_z respectively. The system can be described in the rotating frame, where the x-y plane moves around the z-axis at the precession frequency of the bulk magnetization ($M_{x\prime}$, $M_{y\prime}$, and $M_{z\prime}$; Figure 1.2), with the evolution of the system's magnetization being described by:

$$\frac{dM_{x\prime}}{dt} = M_{y\prime}(\omega_1 - \omega_0) - \frac{M_{x\prime}}{T_2} \tag{1.26}$$

$$\frac{dM_{y\prime}}{dt} = M_{x\prime}(\omega_1 - \omega_0) + \gamma_e M_z B_1 - \frac{M_{y\prime}}{T_2} \tag{1.27}$$

$$\frac{dM_z}{dt} = -\gamma_e M_{y\prime} B_1 - \frac{M_z - M_0}{T_1} \tag{1.28}$$

These equations are named the Bloch equations after Felix Bloch, who first described them for NMR (Bloch, 1946). The longitudinal relaxation (T_1) is the time it takes for the excited longitudinal magnetisation to recover to 64 % of the longitudinal magnetization at equilibrium, and the transverse relaxation (T_2) is the time it takes for relaxation in the transverse plane to reach 36 % of its excited value. Transverse relaxation is a result of, the spin's magnetization returning to its equilibrium state, and magnetic moments from precessing spins going out of phase (dephasing). The Bloch equations only account for transverse relaxation caused by magnetic moments returning to equilibrium and do not account for relaxations due to dephasing of the spins (designated T_m). This dephasing is caused by differences in the effective magnetic field felt by different groups of spins, changing their Larmor frequency with respect to the average frequency of rotation about the external magnetic field. Within this thesis, the spin-spin relaxation is the major limiting factor on the experimental time period (El Mkami et al., 2014).

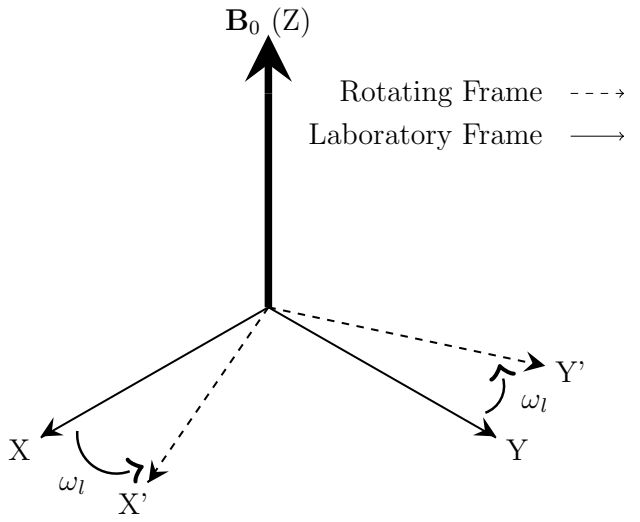

Figure 1.2: An example of the coordinate systems for the laboratory frame (X and Y), with the rotating frame (X' and Y') shown to precess around the external magnetic field at the Larmor frequency (ω_l).

1.5 EPR Methods

Here an overview is given of EPR techniques used within this thesis; these can be split into continuous wave (CW-EPR) and pulsed methods. Continuous wave methods measure the absorption of microwave radiation that occur when the resonance condition is met; sweeping either the frequency of microwave radiation or the external magnetic field, producing spectra related to different resonance conditions within the sample being studied. Pulsed methods excite a range of resonant conditions using a pulse of microwave radiation; followed by measurement of the emitted electromagnetic radiation from the system returning to equilibrium.

1.5.1 CW-EPR

CW-EPR experiments measure the change in amplitude of microwave radiation by either sweeping the microwave frequency or the external magnetic field strength; A model of this power absorption can be produced using Bloch equations solved for the steady state:

$$M_{x'} = -M_z^0 \frac{\gamma_e B_1 (\omega_l - \omega) {T_2}^2}{1 + (\omega_l - \omega)^2 {T_2}^2 + {\gamma_e}^2 {B_1}^2 T_1 T_2} \tag{1.29}$$

$$M_{y'} = +M_z^0 \frac{\gamma_e B_1 T_2}{1 + (\omega_l - \omega)^2 {T_2}^2 + {\gamma_e}^2 {B_1}^2 T_1 T_2} \tag{1.30}$$

$$M_z = +M_z^0 \frac{1 + (\omega_l - \omega)^2 {T_2}^2}{1 + (\omega_l - \omega)^2 {T_2}^2 + {\gamma_e}^2 {B_1}^2 T_1 T_2} \tag{1.31}$$

where M_z, $M_{x'}$, and $M_{y'}$ are the magnetizations in the rotating frame (figure 1.2); M_z^0 is the magnetization of the system at equilibrium; ω_l is the Larmor frequency of the system; ω is the frequency of the applied magnetic radiation; T_1 and T_2 are the longitudinal and transverse relaxation times respectively; B_1 is the applied magnetic field; and γ_e is the electrons gyromagnetic ratio.

The magnetic susceptibility (χ), a dimensionless proportionality constant defined by the degree of the samples polarization per magnetic field strength, can be used to translate these magnetizations into a change in power of the system (Weil and Bolton, 2007). Magnetization of a system with the external magnetic field along the z-axis can be described using the static magnetic susceptibility (χ^0) by:

$$M_z = \frac{\chi^0 B_z}{\kappa \mu_0} \tag{1.32}$$

where μ_0 is the magnetic permeability of a vacuum and κ is a correction factor to the magnetic permeability for the media under investigation. During a CW-EPR experiment, electromagnetic radiation is introduced such that the magnetic field ($\boldsymbol{B}_1$) oscillates along a single axis; its magnitude described by the scalar B_1, representing half the amplitude of the applied electromagnetic radiation. Magnetic susceptibilities associated with the B_1 field are χ' and χ'' where:

$$\chi' = \frac{+\kappa \mu_0 M_{x'}}{B_1} \tag{1.33}$$

$$\chi'' = \frac{-\kappa \mu_0 M_{y'}}{B_1} \tag{1.34}$$

Substituting in steady state Bloch equations for M_x, and M_y, transform the description of the systems magnetic susceptibilities to:

$$\chi' = \chi^0 \frac{\omega_l(\omega_l - \omega){T_2}^2}{1 + (\omega_l - \omega)^2{T_2}^2 + {\gamma_e}^2{B_1}^2 T_1 T_2} \tag{1.35}$$

$$\chi'' = \chi^0 \frac{\omega_l T_2}{1 + (\omega_l - \omega)^2{T_2}^2 + {\gamma_e}^2{B_1}^2 T_1 T_2} \tag{1.36}$$

The power absorbed within a CW-EPR experiment can then be expressed by:

$$P(\omega) = 1 \frac{\omega\chi''{B_1}^2}{\mu_0 V} \tag{1.37}$$

Where V is the sample volume. Expansion of this equation gives:

$$P(\omega) = \frac{\pi{B_1}^2 \omega\omega_l \chi^0 Y}{\mu_0 (1 + {\gamma_e}^2{B_1}^2 T_1 T_2)^{1/2}} \tag{1.38}$$

Where the line shape of the spectra is described by Y: a Lorentzian function of $\omega - \omega_l$:

$$Y(\omega - \omega_l) = Y_{max} \frac{\Gamma^2}{\Gamma^2 + (\omega - \omega_l)^2}. \tag{1.39}$$

Where Y_{max} is the maximum absorption of the spectra, and Γ is half the line width at half height within the absorption spectra:

$$\Gamma = \frac{(1 + \gamma_e{}^2 B_1{}^2 T_1 T_2)^{1/2}}{T_2} \tag{1.40}$$

The line width is a result of line broadening, which can be separated into inhomogeneous and homogeneous line broadening. Inhomogeneous broadening is caused by differences in the magnetic field felt by different electrons within the sample, giving the spectra a Gaussian line shape; and homogeneous broadening is broadening of spectra where all electrons are exposed to the same magnetic field, producing the Lorentzian function mentioned above.

1.5.2 Pulsed EPR

Pulsed EPR spectroscopy functions by using pulses of electromagnetic radiation to excite spin packets within an external magnetic field. It then monitors the emission of microwave radiation as the magnetization of the system relaxes back to equilibrium. EPR experiments were performed for this thesis using square pulses of microwave radiation, where microwave radiation of a constant frequency and amplitude are applied over a finite time (t_p) producing an applied magnetic field ($\boldsymbol{B}_1$). Transverse components of the Larmor precession at equilibrium around the external magnetic field ($\boldsymbol{B}_0$) cancel out, leaving a net magnetization along the z-axis ($\boldsymbol{M}_0$) (figure 1.3, A). Upon the introduction of $\boldsymbol{B}_1$, magnetization matching the resonance condition is rotated by a flip angle (α) around the axis $\boldsymbol{B}_1$ is applied along, (figure 1.3, B) where:

$$\alpha = \gamma_e |\boldsymbol{B}_1| t_p \tag{1.41}$$

And off resonance magnetization precesses around an effective magnetic field $\boldsymbol{B}_{eff}$ (figure 1.3, C) with:

$$\boldsymbol{B}_{eff} = \boldsymbol{B}_0 + \boldsymbol{B}_1 \tag{1.42}$$

Longer pulses of microwave radiation average out a greater proportion of the off-resonance magnetization, reducing numbers of different transitions excited by the microwave pulse. Consequently, shorter pulses excite a greater proportion of the EPR spectra than long pulses. Once the microwave pulse is switched off, the sample's net magnetization precesses about the external magnetic field inducing a detectable, alternating current in detector coils. Over the time of the experiment, dephasing of transverse electron spin magnetizations reduce the net magnetization in the transverse plane, observed as a decay in oscillations, referred to as the free induction decay (FID).

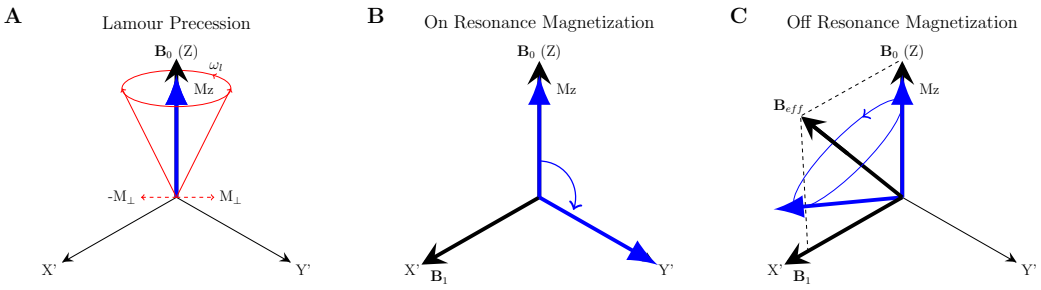

Figure 1.3: (A) The Larmor precession for electron spins within an external magnetic field (B_0). Across a sample the transverse magnetization ($M_\perp$) averages out leaving only the magnetization along z (M_z). (B) Rotation of on resonant electron magnetization by applying a B_1 field along X'. (C) Rotation of off resonance electron magnetization by applying a B_1 field along X'.

Within pulsed EPR, microwave radiation from the pulses resonates for a time after the end of the pulse, referred to as the dead time, where the signal from the sample is too weak to be read above background noise. To overcome the dead time, pulsed EPR experiments set up a spin echo, with the simplest spin echo being created by a pulse with a 90° flip angle ($\frac{\pi}{2}$ pulse), which rotates the magnetization into the transverse plane. The dephasing magnetization is subjected to a π pulse at a time of τ, inverting their position around the z axis. This enables faster precessing magnetizations to rephrase with slower precessing magnetizations at a time τ after the π pulse, creating a spin echo (figure 1.4).

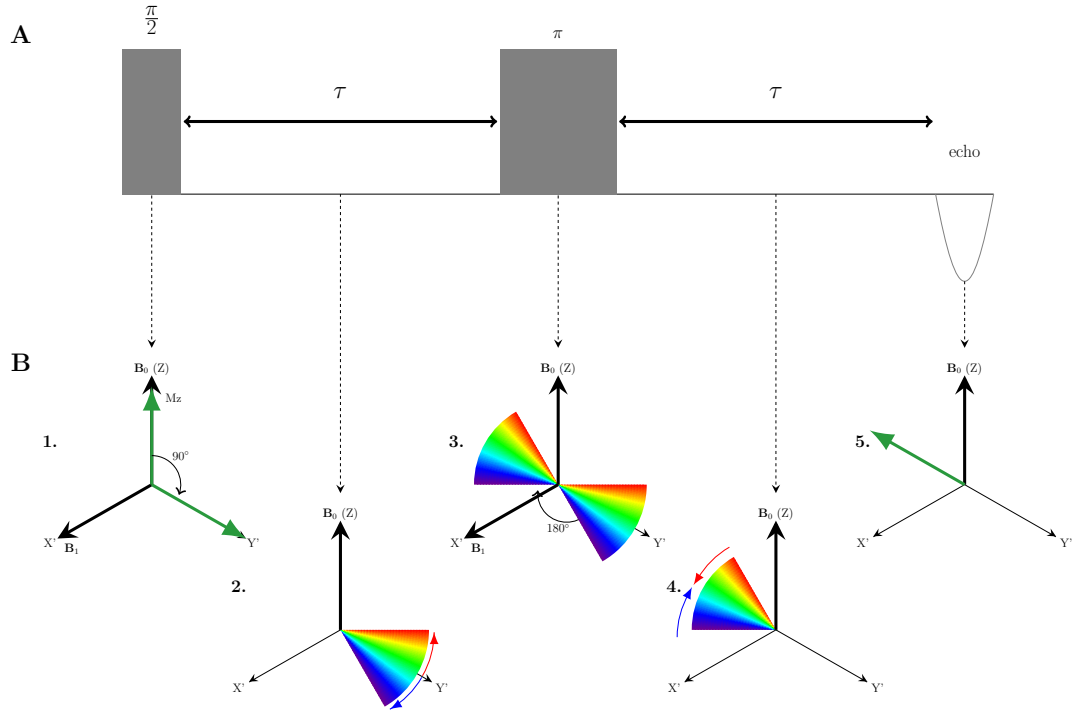

Figure 1.4: (A) The pulse sequence used to produce a Hahn echo. (B) The evolution of the magnetization during the pulse sequence; green arrows represent the focused net magnetization, and the multi-coloured cone represents dephasing magnetization, with red indicating magnetization that precesses slower than the net magnetization of the sample, and the blue region representing magnetization that precesses faster than the magnetization of the sample.

1.5.2.1 Tm Measurements

Not all magnetization is rephrased to form the spin echo. This non-recoverable dephasing is a result of fluctuations in localised magnetic fields. The most common cause of local magnetic field fluctuations are interactions between the excited spin and nearby nuclear spins, diffusing the spin temperature from equation 1.24. The rate of spin temperature diffusion is described by a stretched exponential decay (Lindgren et al., 1997):

$$M(t) = M(0)e^{(\frac{-t}{T_m})^x} \tag{1.43}$$

where M(t) is the transverse magnetization after a time (t), M(0) is the initial magnetization, x is the parameter that forms a stretched exponential, and T_m is the time it takes for non-recoverable magnetization to reach 37 % of its original value.

T_m describes the spin–spin component of a system's transverse relaxation, in cases where the T_2 of a system is an order of magnitude less than the T_1, the T_m can be measured using a $\frac{\pi}{2}$ -- τ-- π -- τ—spin echo pulse sequence (figure 1.4, A). Lengthening the time τ within the pulse sequence gives an exponential decay in the magnitude of the spin echo. The T_m of the system can be measured by fitting the spin echo decay to equation 1.43.

1.5.2.2 Pulsed Electron Double Resonance (PELDOR)

The most commonly used pulsed technique within biological structures is PELDOR. PELDOR splits electrons in the sample into spin packets excited by pulses of microwave radiation at different frequencies, labelled the pump pulse and the

observer pulse. The pulse sequence used for acquiring data presented within this thesis is 4-pulse PELDOR. In 4-pulse PELDOR the observer pulse sequence refocuses the initial spin echo (figure 1.5), enabling the echo to be detected outside the experiment's dead time (Martin et al., 1998; Pannier et al., 2011). During PELDOR the spin packet of the pump pulse is excited by a π pulse at a time τ_p after the second π pulse in the observer pulse sequence. The refocused echo intensity from the observer pulse is modulated depending on the value of τ_p (figure 1.5). Modulation of echo intensity at different values of τ_p gives an oscillation related to dipolar coupling between spin packets excited by the pump pulse and the observer pulse.

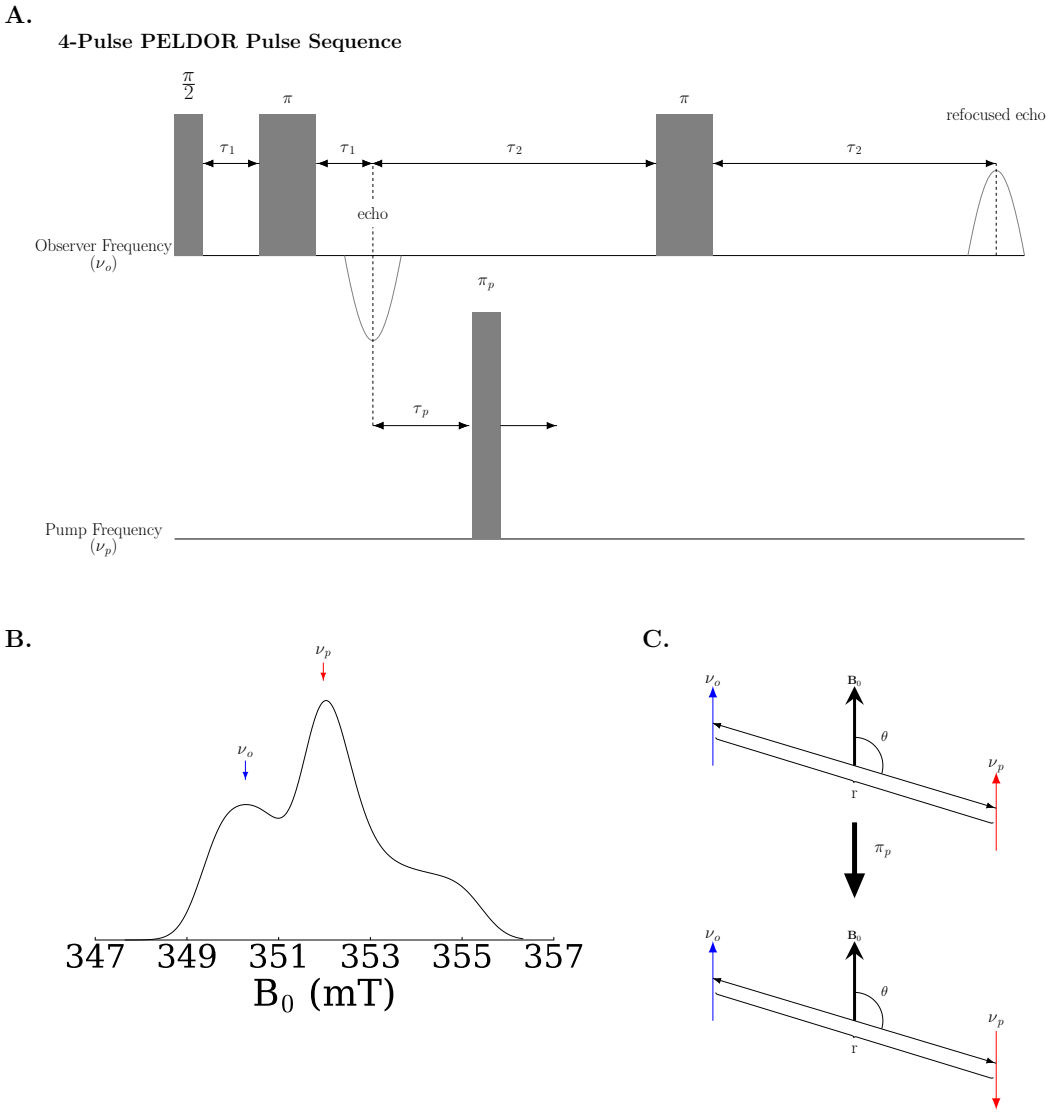

Figure 1.5: (A) The pulse sequence for 4-pulse dead time free PELDOR. (B) Locations of the microwave pulse frequencies for the pump (ν_p) and observer (ν_o) pulses. (C) An illustration of the distance (r) and angle between electrons under the pump and observer pulses, showing differences between the inversions of magnetization by the pump pulse.

Theoretically, the dipolar coupling between the spin packets introduces an additional Hamiltonian operator into the total energy of the system:

$$\mathcal{H}_{dd} = \frac{\mu_0}{4\pi} g_1 g_2 {\beta_e}^2 \boldsymbol{S}_1^{\ T} \cdot \boldsymbol{T} \cdot \boldsymbol{S}_2 \qquad (1.44)$$

where $\boldsymbol{S}_1$ and $\boldsymbol{S}_2$ are the spin operators of electrons under the pump and observer pulses, $\boldsymbol{T}$ is a matrix describing the spatial aspects of the dipolar coupling (equation 1.16); g_1 and g_2 are the g values for $\boldsymbol{S}_1$ and $\boldsymbol{S}_2$ respectively; μ_0 is the magnetic permeability of a vacuum, and β_e is the bohr magneton. The dipolar interaction creates a shift in the Larmor frequency of interacting spins, dephasing the signal described by:

$$\omega_{dd} = \frac{\mu_0 g_1 g_2 {\beta_e}^2}{4\pi\hbar} \frac{(1 - 3\cos^2\theta)}{r^3} \qquad (1.45)$$

where r is the distance between the excited spin packets and θ is the angle between r and the external magnetic field.

When performed on frozen biological samples the PELDOR signal (V(t)) is made up of two components:

$$\mathrm{V(t)} = \mathrm{V}_{intra}(\mathrm{t}) \cdot \mathrm{V}_{inter}(\mathrm{t}) \qquad (1.46)$$

where $\mathrm{V}_{intra}(\mathrm{t})$ describes the intra-molecular interactions and $\mathrm{V}_{inter}(\mathrm{t})$ describes the intermolecular interactions. An approximation of dipolar interactions over long distances within a homogenous distribution of molecules in 3D space, which

contribute to $V_{inter}(t)$ in most cases, can be modelled using an exponential decay. Alternately, $V_{intra}(t)$ can be determined by integrating over different distance vectors present in the sample, alongside angles between these vectors and the external magnetic field (Goldfarb, 2012; Milov et al., 1998):

$$V_{intra}(t) = V(0)\left(1 - \int_0^{\infty} D(r) \int_0^{\pi/2} \lambda(\theta)[1 - \cos(\omega_{dd}(r,\theta)t)] \cdot \sin\theta \, \delta\theta\delta r\right) \quad (1.47)$$

Where $V(0)$ is the initial echo intensity, $D(r)$ is the distance distribution function made up of all the distances present in the sample, and $\lambda(\theta)$ is the systems modulation depth parameter: the probability of spins being flipped by the pump pulse. The modulation depth (Δ) is the drop from the maximum intensity of the PELDOR experiment to the line the PELDOR data oscillates around, defined by (Giannoulis et al., 2013):

$$\Delta = 1 - (1 - \lambda(\theta))^{n-1} \quad (1.48)$$

where n is the number of interacting spins. For a two spins system this gives:

$$\Delta = \frac{\left(1 - \lambda(\theta)\right) - 1}{(1 - \lambda(\theta))} \quad (1.49)$$

Thus, allowing the modulation depth to be used for determining the number of interacting spins within the sample.

1.5.2.3 Measuring Orientations from PELDOR

When the g factor of the unpaired electron is anisotropic, such as the g factor of the nitroxide radical that is commonly used in biological EPR; raising the external magnetic field strength broadens the absorption spectra of the sample under investigation (figure 1.6) (White et al., 2007). The breadth of the spectra allows selection of spin packets based upon their orientation within the external magnetic field (Abdullin et al., 2015; Kaminker et al., 2013). Measuring interactions by selecting spin packets at different orientations to the external magnetic field, produces a series of PELDOR spectra that vary in their modulation depth. This variation is caused by the different inversion efficiencies ($\lambda(\theta)$) of different spin packets. In addition, PELDOR also has an orientation component based upon the angle between the external magnetic field and the spin-spin vector (Abdullin et al., 2015). Consequently, the frequency of oscillations from the PELDOR data change depending on which orientations are selected by the pump pulse, and which orientations are selected by the observer pulse. Analysis of spectra produced in this manner allows orientations between two packets of spins to be determined, provided the individual species containing unpaired electrons are in well-defined orientations (Schiemann et al., 2009).

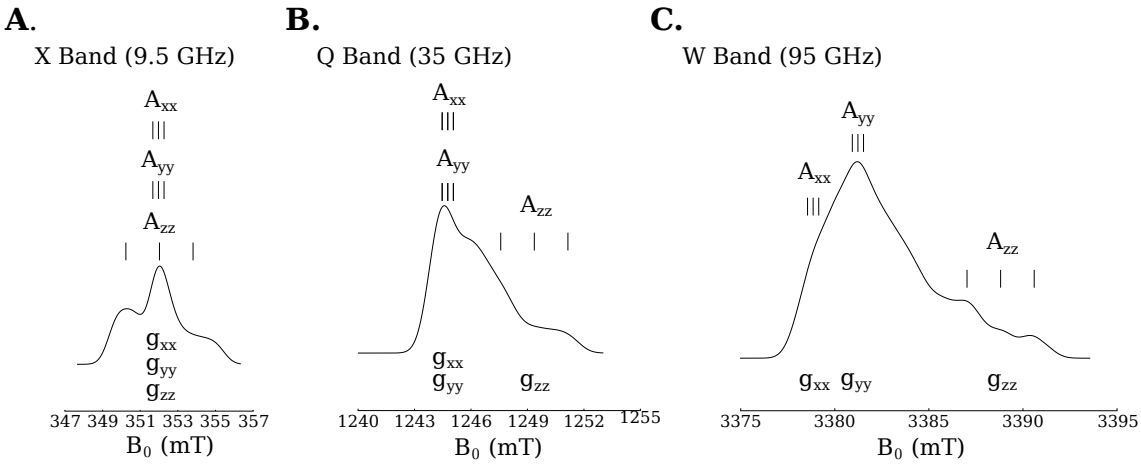

Figure 1.6: The absorption spectra of nitroxides at X (A.), Q (B.), and W (C.) band. Increasing the microwave frequency resolves the g anisotropy of the sample, broadening the spectra from X to W band. The A and g anisotropy of a nitroxide are aligned, so as the g anisotropy of the spectra is resolved, the different A tensors occupy different areas of the spectra.

1.6 PELDOR Analysis

The software package used within this thesis for analysing PELDOR data was DeerAnalysis; a matlab package developed by Gunnar Jeschke (Jeschke et al., 2006). As mentioned before, the raw PELDOR data $V(t)$ can be split into $V_{inter}(t)$: representing a background decay ($B(t)$) from long range distances within the sample (r > 400 nm), and the intramolecular interactions producing $V_{intra}(t)$: a form factor ($F(t)$) of the short-range interactions:

$$V(t) = B(t)F(t) \tag{1.50}$$

$B(t)$ can be fit to the exponential decay:

$$B(t) = e^{-kt^{D/3}} \tag{1.51}$$

where D is the dimensionality of the background correction and k is a constant for the background decay. The background function is determined by fitting the exponential decay to an area of raw data where the oscillations from $F(t)$ have fully decayed. $F(t)$ can be defined as a product of a kernel function ($K(t,r)$) multiplied by the intramolecular distance distribution ($P(r)$):

$$F(t) = K(t,r)P(r) \tag{1.52}$$

The solution to the reverse transformation of this is ill posed. Consequently, performing a root mean squared minimization results in a series of sharp peaks. Within DeerAnalysis, $P(r)$ is determined by fitting $F(t)$ using Tikhonov regularization:

$$G(P) = \|KP - F\|^2 + \alpha \left\| \frac{\delta^2}{\delta r^2} P \right\|^2 \tag{1.53}$$

where $\|KP - F\|^2$ is the root mean squared deviation (RMSD) from the experimental data of the fit (ρ), $\left\| \frac{\delta^2}{\delta r^2} P \right\|^2$ is a smoothing factor for the data (η), and α is the weighting factor for η.

The smoothness of the fit is dependent upon α; with lower values giving a series of sharp peaks within the distance distribution, and higher values producing single

broad distance distributions. α is determined by plotting an L-curve of $\ln \eta$ against $\ln \rho$ for different values of α. The optimum value of α gives the best RMSD fit (lowest $\ln \rho$) with a minimum amount of smoothing (lowest $\ln \eta$). Within the L-curve this point is closest to the bottom left hand corner of the graph, on the bend of the L curve.

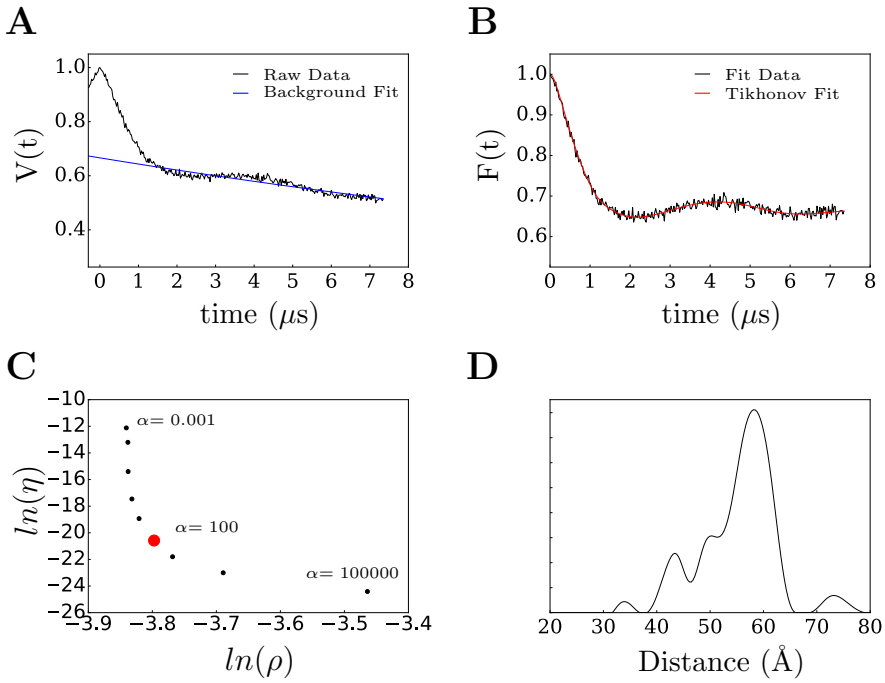

Figure 1.7: An example of fitting PELDOR data using DeerAnalysis. (A) Raw PELDOR data with the background fit (B(t)) shown in blue. (B) Background corrected PELDOR data with the Tikhonov fit in red. (C) The L-Curve for the Tikhonov fit, with the value of α used to derive the distance distribution highlighted in red. (D) Distance distribution from the Tikhonov fit.

Artefacts in PELDOR distance distributions occur due to errors in both the background correction, with the choice in background correction introducing false distances into the samples data; and the presence of orientations within the

sample, where a lack of averaging contributes to $F(t)$. However, changing the background correction of the data and observing which distance distribution peaks are shifted allows background correction artefacts to be identified. Furthermore, observing shifts in the distance distribution caused by changing the spectral positions of either the pump pulse or the observer pulse, identifies orientation artefacts.

Chapter 2: An Introduction to EPR in Structural Biology

2.0 Summary

In this chapter, the area within structural biology that EPR occupies is expanded. An overview of the resources available for using EPR within a biological system; namely databases of biological structures and computational packages, is given. This is followed by an introduction to the use of site directed spin labelling (SDSL) for introducing radicals into large biological structures, and the methods available for analysing EPR data for protein structure refinement.

2.1 Structural Biology of Proteins

One of the most useful resources for structural biology is the protein data bank (PDB): a repository for NMR, X-ray crystallography, and electron microscopy structural data (Berman et al., 2007, 2014). This vast database of structures provided by the PDB has allowed classification of proteins based upon their 3D structures (Holm and Sander, 1996), with the most commonly used classification systems being SCOP (Murzin et al., 1995), CATH (Orengo et al., 1997), and FSSP (Holm and Sander, 1994). In all these systems, protein structures are grouped into similar folds (Hadley and Jones, 1999), defined by protein interactions and the placement of the secondary structural features. Current statistics of the PDB show that there have been no new folds by the SCOP classification and only 16 by the CATH classification deposited since 2008. Advancements in acquisition technology for X-ray crystallography (Miao et al., 2015; Zhou et al., 2016), NMR sensitivity (Gelis et al., 2013; Palmer et al., 2015; Parthasarathy et al., 2013), and cryo EM resolution (Bai et al., 2015; Fernandez-Leiro and Scheres, 2016) has raised the number of protein structures deposited per year from 6900 to 9500 over the same time. The limited number of folds compared to the number of protein structures,

enables an increasingly effective use of statistical approaches to homology modelling where there is a lack of experimental data (Gonzalez et al., 2012; Politis et al., 2014; Samish et al., 2015; Schwede, 2013).

FRET (Greife et al., 2016; Vámosi et al., 2008), PELDOR (Ward et al., 2009a) and mass spectrometry (Back et al., 2003; Kalisman et al., 2012) provide empirical evidence for homology models and enable the positioning of individual subunits in space (Lasker et al., 2012; Schwede, 2013; Zhang et al., 2015). Each technique has its own set of advantages for answering specific questions; mass spectrometry is useful for determining protein binding interfaces (Gorasia et al., 2016; Kalisman et al., 2012; Udeshi et al., 2013); FRET has the ability to measure distances on a single molecular level (Bystranowska et al., 2012); and PELDOR measures distances in the range of approximately 15 Å (Jeschke, 2002) to the order of 150 Å within a protein structure (see chapter 6). Determining the most appropriate technique to use for the task often depends on the question being asked and the properties of the protein under investigation. For instance, mass spectrometry is useful in samples with unknown binding interfaces where large individual margins of error are acceptable (Chu et al., 2004).

Distances can be investigated using FRET or PELDOR. FRET measures the transfer efficiency between a donor and acceptor molecule, requiring the introduction of two different molecular groups to attain a measurement, with the transfer efficiency giving a drop-off in accuracy over longer distances. PELDOR allows distance measurement between the same label groups, with no reduction in accuracy as the distance is increased (Pornsuwan et al., 2013). This makes PELDOR particularly useful for symmetrical multimeric proteins, where it is

important for multiple sites to be labelled using a single labelling chemistry, see (Ghimire et al., 2009; Kerry et al., 2014; Ward et al., 2009b). The disadvantage of using PELDOR is its low sensitivity and the requirement for low temperatures during most measurements. Conversely, FRET is a single molecule technique that can be performed at room temperature, allowing its use under physiological conditions.

2.2 Site Directed Spin Labelling

It is hard to argue that there has been a more significant development for biological EPR than site directed spin labelling (SDSL) (Klug and Feix, 2008). A spin label is a paramagnetic molecule, possessing a chemistry designed to attach at a specific site on a large biomolecular structure. The spin label attachment site on a protein is often an amino acid residue or motif that can be introduced using site directed mutagenesis. Sulphhydryl (or sulfhydryl) reactive chemistry is the most popular binding method for spin labels as it allows the label to bind the uncommon amino acid cysteine. The rarity of cysteine simplifies the removal of unwanted, naturally occurring residues and consequently the introduction of site-specific residues into a protein's primary structure (Hubbell et al., 1996). To enable the use of EPR in cases where cysteine is functionally important, alternative attachment procedures and chemistries have been developed, such as using unnatural amino acids with a unique exploitable chemistry (Becker et al., 2005; Fleissner et al., 2009).

The paramagnetic species chosen for the label is dependent upon the experiment that needs to be performed. In CW-EPR, the spectra of the paramagnetic species has to be affected by the parameter under investigation, for example, the label's

motion or the polarity of the environment (Marsh, 2010). In pulsed EPR, the microwave pulse has to excite enough of the spectra to produce a measurable FID, and PELDOR requires the breadth of the spectra to encompass pulses of microwave radiation at two different frequencies (Pannier et al., 2011). Additionally, the size of the paramagnetic species should be taken into consideration; larger labels are more likely to distort the protein structure and can increase the difficulty of translating experimental data into structural information. Paramagnetic species used for spin labels have included: metal centres such as gadolinium (Doll et al., 2015) and copper (Cunningham et al., 2015; Voss et al., 1995); and radical species, such as the trityl radical (Reddy et al., 2002; Reginsson et al., 2012a) and the nitroxide radical (Fielding et al., 2014) (figure 2.1). Metal centres produce broad absorption spectra with a low intensity (Lueders et al., 2011; Narr et al., 2002); trityl radicals produce a sharp spectrum with a high intensity (Reginsson et al., 2012a); and the nitroxide spectrum is intermediate for both spectral width and intensity.

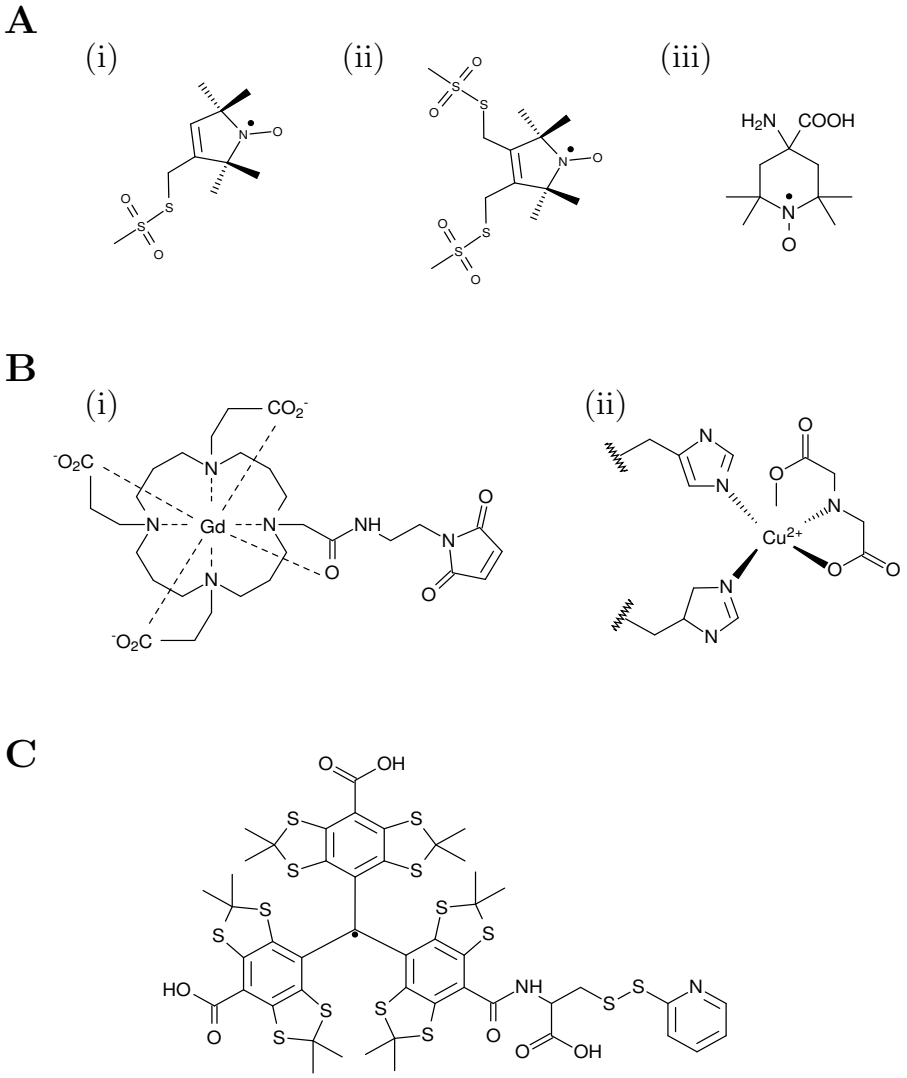

Figure 2.1: Structures of nitroxide, metal centres and trityl spin labels. (A) Nitroxide radical structures for: (i) MTSL, (ii) 3,4 Bis-MTSL, (iii) TOAC. (B) Metal centre labels (i) Gd (ii) Cu^{2+}, His-IDA. (C) Trityl spin label (tetrathiatriarylmethyl (TAM) CT02-TP). Label structures were taken from (Fielding et al., 2014) and (Cunningham et al., 2015).

This intermediary nature gives Nitroxide radicals a favourable spectrum for performing pulsed EPR by providing the breadth required to encompass microwave pulses at two different frequencies while maintaining signal intensity. For CW-EPR, changes in the nitroxide spectrum are able to monitor both the label's motion on a nanosecond timescale (Benial et al., 2011; DeSensi et al., 2008) and

the polarity of its environment (Haugland et al., 2016; Marsh, 2010). The nitroxide radical can be incorporated into a wide range of spin labels due to its small size (Fielding et al., 2014); the radical is shielded from reduction using groups bound to carbons atoms neighbouring the nitroxide (Paletta et al., 2012). Methyl groups are often chosen for this purpose, allowing the spin label to maintain its low volume. However, rotation of the methyl groups produces fast relaxation times at temperatures above 70 K (Zecevic et al., 1998). Shielding residues can be modified to remove the relaxation effects of methyl rotation by replacing the buttressing methyl groups with hexane rings; allowing higher temperature measurements (Krumkacheva and Bagryanskaya, 2017). Additionally, the nitroxide can be modified to be protected against a reducing environment by buttressing the nitroxide with ethyl residues (Jagtap et al., 2015). For regular applications the most commonly used spin label is S-(1-oxyl-2,2,5,5-tetramethyl-2,5-dihydro-1H-pyrrol-3-yl) methyl methanesulfonothioate (MTSL) which contains a nitroxide group shielded by 4 methyl groups, and a methyl thiosulphonate chemistry. This chemistry allows MTSL to react with cysteine residues, to form the side chain R1 (Altenbach et al., 1989)(figure 2.2).

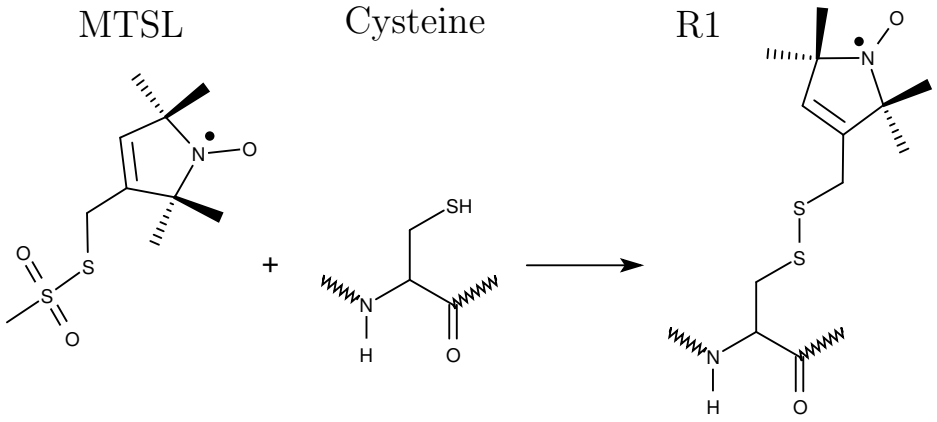

Figure 2.2: Reaction mechanism for MTSL and cysteine to form R1.

2.3 Modelling the distribution of Spin Labels onto a Protein Structure

The use of spin labels introduces a double uncertainty into distance measurements: that of the distribution of the label with respect to the underlying protein structure, and that of any effect the label's binding might have on the underlying protein backbone. In the past this has resulted in accepting errors of ~14 Å in PELDOR measurements (Kim et al., 2011) or producing cones to represent rough distributions of the label (Alexander et al., 2008; Hirst et al., 2011). It is now common practice to model a distribution of the label onto the protein structure using either molecular dynamics (Hammond et al., 2014), or a rotamer library of dihedral angles within the label's attachment 'leg' (Figure 2.3)(Polyhach et al., 2011a).

Molecular dynamics can cover a wide range of different labels, provided energy parameters can be produced for the label's attachment leg. Calculating a full energy landscape at each labelled position is too computationally demanding for molecular dynamics to be practical. In order to reduce the time taken, simulations are run using a subsection of the forces, with the van der Waals radii often the only intermolecular force implemented during molecular dynamics (Steinhoff et al., 2000). Accurate replication of the molecular environment is produced using less calculation intensive force fields to maintain fidelity of the known structure of the protein backbone, and implement other forces of interest. For example, harmonic restraints can maintain the coordinates of specific atoms throughout the dynamics run, and symmetry restraints can ensure homodimers maintain their structural integrity during the dynamics run (Hammond et al., 2014). The limited forces used

in molecular dynamic runs often create broader modelled distance distributions than experimental distance distributions.

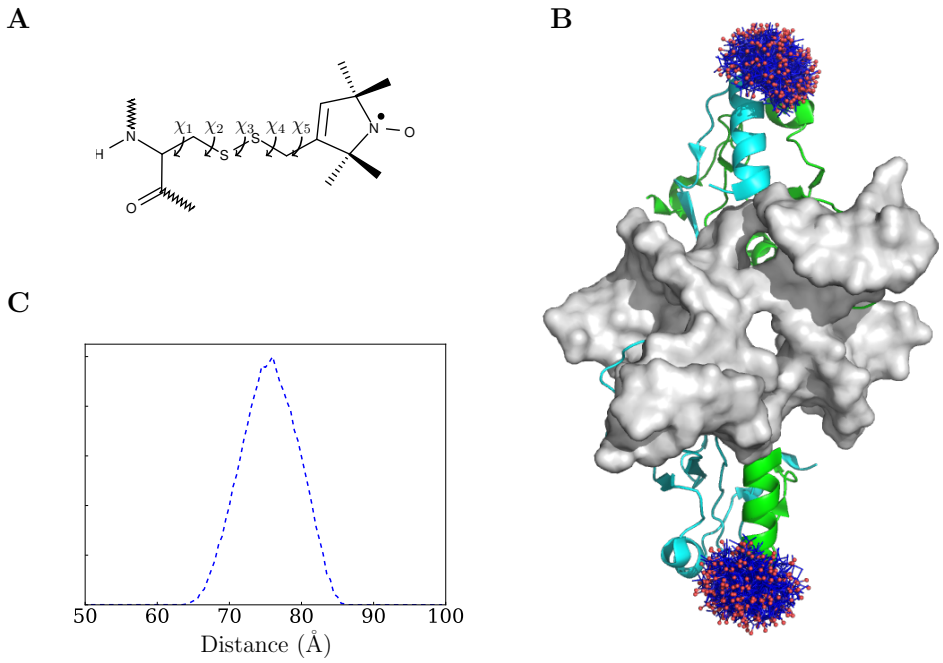

Figure 2.3: (A) The dihedral angles of the leg of R1 used for the MTSL Wizard rotamer library. (B) R1 modelled onto S29 of endonuclease I (Endo I; PDB ID: 2PFJ). (C) A distance distribution derived from using MTSL Wizard shown in B.

Methods using a rotamer library allow spin label distributions to be determined in a more computationally efficient manner than molecular dynamics. However, to form a rotamer library, dihedral angles within the leg of the spin label must be well understood. The two main programs that use a rotamer library are MMM (Polyhach et al., 2011b) and MTSL Wizard (Hagelueken et al., 2012); each have a selection of different labels that can be modelled onto a known protein backbone in a time efficient manner. The most commonly used spin label: MTSL, has its binding leg split into 5 angles labelled χ_{1-5}, each angle has different energy functions assigned to it based upon various orientations seen within crystal

structures (Guo et al., 2008; Islam et al., 2013; Langen et al., 2000). MTSL Wizard uses these angles in conjunction with clashes between the modelled label and surrounding structural features in order to model a label's distribution (Hagelueken et al., 2012).

2.4 The Nitroxide Radical

The unpaired electron within the nitroxide radical is located in the π* antibonding orbital, hence in polar environments the electron density is shifted towards the ^{14}N nucleus (Huber, 2009). This feature allows the nitroxide radical to be used as a probe for solvent exposure at specific sites based upon changes in the absorption spectra (Owenius et al., 2001). The π* orbital has a rhombic symmetry that allows matrices from the hyperfine and Zeeman splitting to be diagonalized, as a result the hyperfine and Zeeman splitting is described in terms of A_{xx}, A_{yy}, and A_{zz}; and g_{xx}, g_{yy} and g_{zz} respectively (Plato et al., 2002). The x, y, and z axes of the hyperfine coupling and Zeeman splitting align, where the x-axis runs along the N-O bond; the z-axis is perpendicular to the x-axis and runs through the π* orbital; and the y axis is perpendicular to the x-z plane so that it forms a right handed coordinate system (Owenius et al., 2001) (figure 2.3, A).

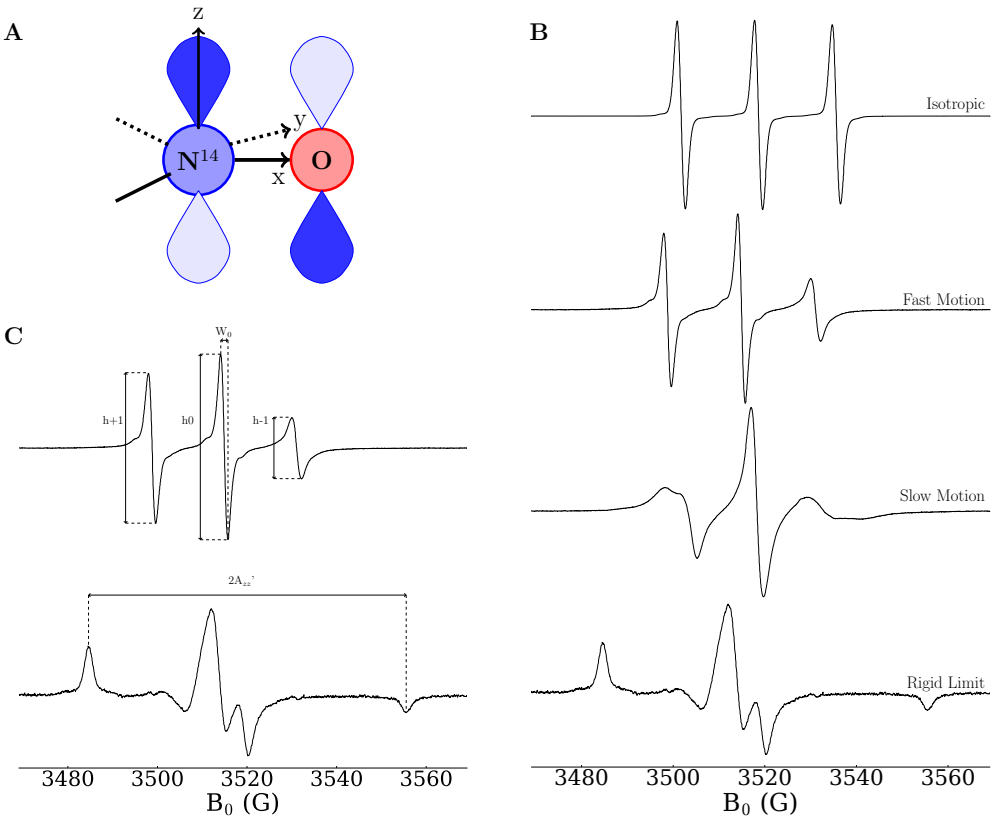

Figure 2.4: Nitroxide CW-EPR Spectra. (A) A cartoon of the nitroxide π orbital with the coordinate set that describes the A and g coupling. (B) X-Band nitroxide spectra of fast, slow, and rigid motional regimes. (C) CW-EPR spectra showing the h+1, h0, h-1, W_0, and $2A_{zz}$' parameters.*

2.5 CW-EPR of the Nitroxide Radical

Broadening of the nitroxide spectrum at X-band (9.4 GHz) is due to the hyperfine coupling. Zeeman coupling becomes more prominent as field strengths and microwave frequencies are raised, further broadening the spectrum (Kirilina et al., 2005). CW-EPR records spectra as the first derivative of the sample's absorption spectrum. If the nitroxide is tumbling fast enough, the A anisotropy averages out into the isotropic hyperfine coupling (A_{iso}): introducing three resonant conditions observed as three sharp lines in the nitroxide spectrum (Nielsen et al., 2004).

Slower nitroxide rotations allow contributions from the anisotropic hyperfine coupling; this creates a series of different motional regimes with spectral line shapes determined by the different contributions of the anisotropic A tensor (DeSensi et al., 2008) (figure 2.3, B).

Data from CW-EPR is often extracted by fitting the spectra to model parameters, with a series of specifically developed packages, including the matlab package EasySpin (Stoll and Schweiger, 2006). As with any fitting process, issues can occur where there are too many variables within the sample, for example, in cases where the spin label can adopt a variety of motional regimes, or where the spin label is exposed to a variety of different environments. Accurate determination of the g and A values can only be achieved by measuring the CW-EPR spectra under a series of different magnetic field strengths (Bagryanskaya et al., 2009). Simpler methods can be used to establish trends in the label's motion by measuring different features of the CW-EPR spectrum. These parameters include the spectral distance between the low field peak and the high field trough ($2A_{zz}$'); the relative heights of the high, central and low field peaks (h_{+1}, h_0, and h_{-1} respectively); and the central line width (W_0) in gauss (figure 2.3, C).

Slower label motions cause spectra to broaden, increasing the $2A_{zz}$' value until it reaches the rigid limit ($2A_{zz}$' = $2A_{zz}$); allowing increases in the $2A_{zz}$' value to give an estimation of the correlation time for the nitroxide under investigation (Mason and Freed, 1974). Within the fast motion regime, both the different heights of the three lines and the line width can give the correlation time τ_c (Bruni and Leopold, 1991; Roozen and Hemminga, 1990):

$$\tau_c = 6.5\times10^{-10} W_0 \left[\left(\frac{h_{+1}}{h_{-1}}\right)^{\frac{1}{2}} - 1\right] \quad (2.1)$$

Where 6.5×10^{-10} is an averaged parameter taking into account both A and g anisotropy's in the particular solvent.

Spectra within the slow motion regime have too low h_{-1} line heights to be measured from the experimental data, however the ratio between h_{+1} and h_0 can give an indication of the different mobility for different labelling sites (Belle et al., 2008; Grijalba et al., 1999).

2.6 Pulsed EPR of the Nitroxide Radical

Pulsed EPR is performed in the solid phase where the nitroxide spectrum is in the rigid limit; here the spectrum is broad enough to accommodate the two pulses required for PELDOR. At magnetic field strengths around X-band, broadening of the spectra is due to the anisotropic hyperfine coupling (Schiemann et al., 2009). At higher field strengths, further broadening of the nitroxide spectra is observed due to the anisotropy in Zeeman splitting, allowing nitroxide labels to be selected by different frequencies of microwave radiation based upon their orientation in the external magnetic field (Reginsson et al., 2012b). The orientation dependence in these two splitting's has an 8 fold symmetry, meaning orientation measurements within nitroxide systems can only be defined within a 90° quadrant (Schiemann et al., 2009; Stevens et al., 2016). Despite this limitation, the nitroxide is still the most promising stable radical for orientation selective PELDOR on protein structures due to the advantages mentioned above (Tkach et al., 2013).

2.7 Aim

SDSL has expanded the use of EPR to a wide range of protein structures, allowing it to determine structural features inaccessible to other techniques, particularly within ill-defined protein structures. In addition, SDSL has increased the ability of EPR to be used to answer questions on protein conformation by allowing a range of different sites to be introduced for measuring distances and mobility within proteins structures. PELDOR aids in the determination of protein structures by measuring distances of 15 Å to 80 Å within a protonated protein structure, the maximum distance limit increasing to around 150 Å when the underlying protein structure is deuterated. However, at present it is not known if this is the actual limit of performing PELDOR on a deuterated protein. The first aim of this thesis is to provide instances where EPR has been used to identify structures within intrinsically disordered protein structures, and the orientation of homodimeric binding conformations (chapters 4 and 5). This is followed by an investigation into the extent of the increase in time period PELDOR can be run over using protein deuteration; and testing different binding conformations of the bi-functional spin label Rx, for those most suited for orientation selective PELDOR (Chapters 6 and 7). These investigations are geared towards: demonstrating where EPR is currently useful in structural biology; and sample preparation methods that allow a greater amount of information to be gathered using PELDOR.

Chapter 3: Methods

3.0 Summary

In this chapter descriptions are given of the methods used throughout this thesis; sections 3.1 to 3.2 describe EPR experiments, 3.3 describes the use and analysis of molecular dynamics, and 3.4 to 3.7 the purification procedures for the different protein constructs.

3.1 CW-EPR

CW-EPR spectra were measured on a Bruker EMX spectrometer working at X-band using a super high sensitivity probe head (ER4122SHQE). The resonator was critically coupled with a typical quality (Q) factor (defined by $\frac{\nu}{\nu_{FWHM}}$, where ν is the resonant frequency and ν_{FWHM} is the full width at half maximum of the absorbed microwave frequencies from the resonator, Figure 3.1) of 7000. The magnetic field was swept over a range of 100 G centred at 3519 G, with the microwave radiation constantly resonating at a constant frequency of 9.876 GHz with a constant power of 10 mW. Background noise was averaged over 10 sweeps, with each sweep collected over 2048 points. Spin label concentrations were calculated by comparing the CW-EPR absorption against a calibration curve made using a series of known 4'-amino TEMPO; absorptions were determined by taking the double integral of the CW-EPR spectra (Figure 3.2).

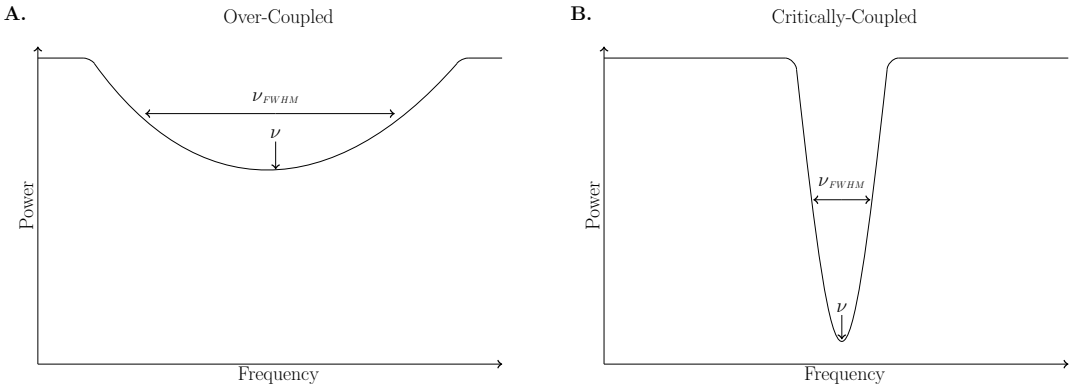

Figure 3.1: Illustrations of the power absorption against microwave frequency for an over-coupled (A) and critically coupled (B) resonator, with the resonant frequency (ν) and full width at half maximum (ν_{FWHM}) labelled.

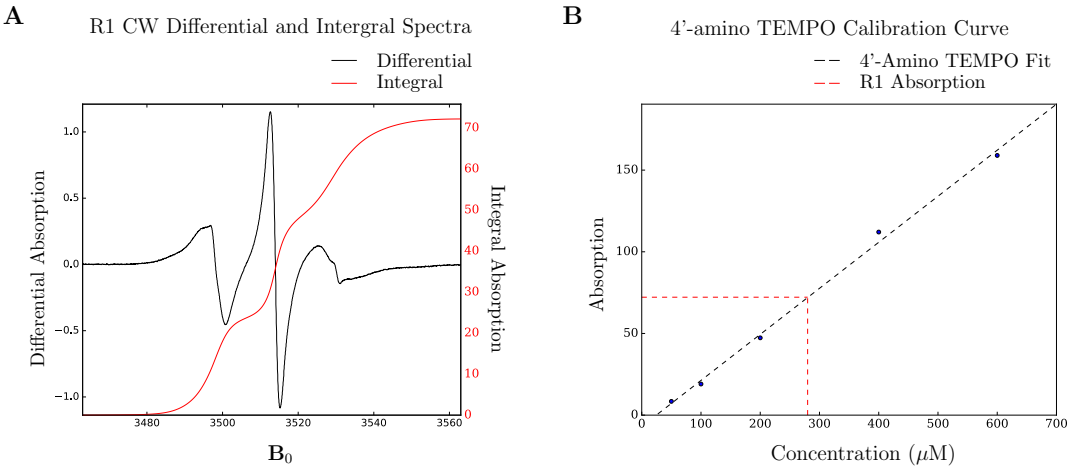

Figure 3.2: Calibration curve alongside an example of CW-EPR spectra. (A) (black) The measured CW-EPR spectra (first differential of the absorption spectra) along with the integral of the absorption spectra (red). (B) Absorptions from 4'-amino TEMPO along with the absorption of the spectra from A shown in red.

3.2 Pulsed EPR

3.2.1 X-Band Spectrometer Set up

X-band (9.8 GHz) PELDOR was performed in 4.0 mm OD, 3.0 mm ID Quartz tubes (Norell S-4-EPR-250S) with a typical sample volume of 100 µl to 150 µl.

Experiments were performed using a Bruker ELEXSYS E580 spectrometer operating at X-band with a second Bruker 400 U microwave source unit, with a MD 4 dielectric ring resonator, over coupled to give a Q factor of <100.

3.2.2 Q-Band Spectrometer Set up

Q-band (34 GHz) PELDOR and Tm measurements were carried out in 3.0 mm OD and 2.0 mm ID Quartz tubes with a typical sample volume of 75 µl to 100 µl. Experiments were performed using a Bruker Elexsys E530 spectrometer with a cylindrical ER 5106 QT-2w resonator, over coupled to give a Q factor of approximately 250-300. The spectrometer was equipped with a cryogen free variable temperature cryostat (cryogenic limited), operating in the 1.5-300 K temperature range. Pulses were amplified using a pulsed travelling wave tube (TWT) amplifier with a nominal power output of 150 W.

3.2.3 PELDOR

PELDOR was performed using a dead time free four-pulse sequence at 50 K. Samples were made up to 50 % D_8 glycerol and flash frozen in liquid nitrogen to produce a frozen glass. The typical $\pi/2$ pulse length was 16 ns and the typical pump π pulse length was 14-18 ns. The pump pulse was set to the highest sensitivity point within the absorption spectra with the observer pulse set at an 80 MHz offset. Receiver offsets were eliminated using two step phase cycling. Each experiment was run with a repetition time of 4 ms with 50 shots per point. The number of data and time points varied between samples, and each sample was run for the number of scans required to give a suitable signal to noise ratio.

3.2.4 Tm Measurements

Tm measurements were performed under the same sample conditions as PELDOR using a π -- τ -- $\frac{\pi}{2}$ -- τ -- echo pulse sequence, with a typical $\pi/2$ pulse length of 16 ns set to the highest sensitivity point within the absorption spectra. Receiver offsets were eliminated using two step phase cycling and each experiment had a repetition time of 4 ms with 50 shots per point. The number of data and time points varied between samples, and each sample was run for the number of scans required to give a suitable signal to noise ratio.

3.3 Modelling

3.3.1 R1 Modelling using MTSSL-Wizard

R1 was built onto structures from the PDB using the MTSSL-Wizard plug-in for pymol (Hagelueken et al., 2012), which uses a rotamer library of dihedral angles in the leg of R1 to produce a distribution of label rotamers. A thorough search was used to produce approximately 200 different rotamers for R1, with van der Waals restraints set to loose within MTSSL-Wizard (2.5 Å van der Waals radius cut-off, and 5 clashes with the surrounding protein structure allowed). Distance distributions were produced by measuring distances between each nitroxide from one site to all rotamers at the opposing site.

3.3.2 Homology Modelling of Muscle Regulation Factor 1 (MuRF 1) using Modeller

The Needle server was used to align the amino acid sequences of coiled coil domain of MuRF 1 to coiled coil domains of each tripartite motif (Trim) family member protein within the PDB: PDB ID's 4LTB (Trim 25), 4CFG (Trim 25), 4CG4 (Trim 20), 4TN3 (Trim 5α), and 4NQJ (Trim 69). Needle uses the Needleman-

Wunsch algorithm and was performed using a gap penalty 10, a gap extension penalty of 5.0, an end gap penalty of 10, and an end gap extension penalty of 1. The higher gap extension penalty when compared to the default value of 0.5 was used to maintain the alignment of the coiled coil domain heptad repeats. The automodel feature of Modeller (Webb and Sali, 2002) was used to thread the MuRF 1 coiled coil sequence onto the protein structural templates from the PDB from the aligned coiled coil domain. Homology models were interrogated using MTSSL-Wizard as described in section 3.3.1 to produce modelled distance distributions that could be compared against the PELDOR distance distribution.

3.3.3 Rx construction using Xplor-NIH

Rx was built onto the PDB structure of Vps 75 (PDB ID: 2ZD7) and molecular dynamics were carried out using Xplor-NIH (Schwieters et al., 2003). During the molecular dynamics run van der Waals radii were the only intermolecular forces used in the simulations. The protein backbone structure was maintained using harmonic restraints, which introduce an energy function to keep the backbone within its initial coordinates.

Dynamics were performed using the Verlet algorithm within Xplor (Verlet, 1967), with the initial residue positions determined by undergoing a 200 step minimisation, followed by a 2 ns dynamic run at 600 K, and a 2 ns dynamics run at 500 K. Distributions of Rx were determined by performing molecular dynamics at 400 K with coordinate files written out at 2 ns time steps , with a total simulation time of 4 μs. Distance distributions were determined by measuring the distance between the Rx nitroxide nitrogen from one site to all nitroxide nitrogens in the distribution of Rx at the opposing site.

3.3.4 Rx orientations to the protein backbone

To define the rotational distribution of the nitroxide at each Rx labelling site, a series of rotational transformations that placed the nitroxide ring of Rx into a specific orientation in relation to its binding site were carried out. This orientation had the N-O vector perpendicular to the plane of the β-sheet or the helical axis of the α-helix, with the plane of the nitroxide ring parallel to the Cα to Cα vector of the Rx binding site (Cα-Cα).

The three rotational transformations required to position the nitroxide ring were referred to as the Tilt, Twist, and Roll, and were designated to describe different motions of Rx. The Tilt represented a rocking motion around Cα-Cα, Twist represented a waving motion around an axis perpendicular to the nitroxide ring plane, and Roll represented a turning motion around the N-O vector (figure 3.3, D).

3.3.4.1 Assigning axes

For defining angle distributions a Cartesian coordinate set was assigned to both the nitroxide ring and secondary structure feature (figure 3.3, A, B and C). The nitroxide coordinate set had the x-axis assigned along the N-O vector. The y-axis was perpendicular to the N-O vector in the plane of the nitroxide ring, with its vector in the direction of the nitroxide nitrogen to the side of the ring closest to the highest numbered binding site. The z-axis vector was perpendicular to the plane of the ring, positioned such that it forms a Cartesian coordinate set (figure 3.3, A). The secondary structural coordinate set was assigned where the x-axis was perpendicular to the plane of the β-sheet or the helical axis of the α-helix; the y-axis is the Cα-Cα vector running from the lowest to the highest numbered residue

of the Rx binding site. Finally the z-axis vector was introduced to make up the Cartesian coordinate set.

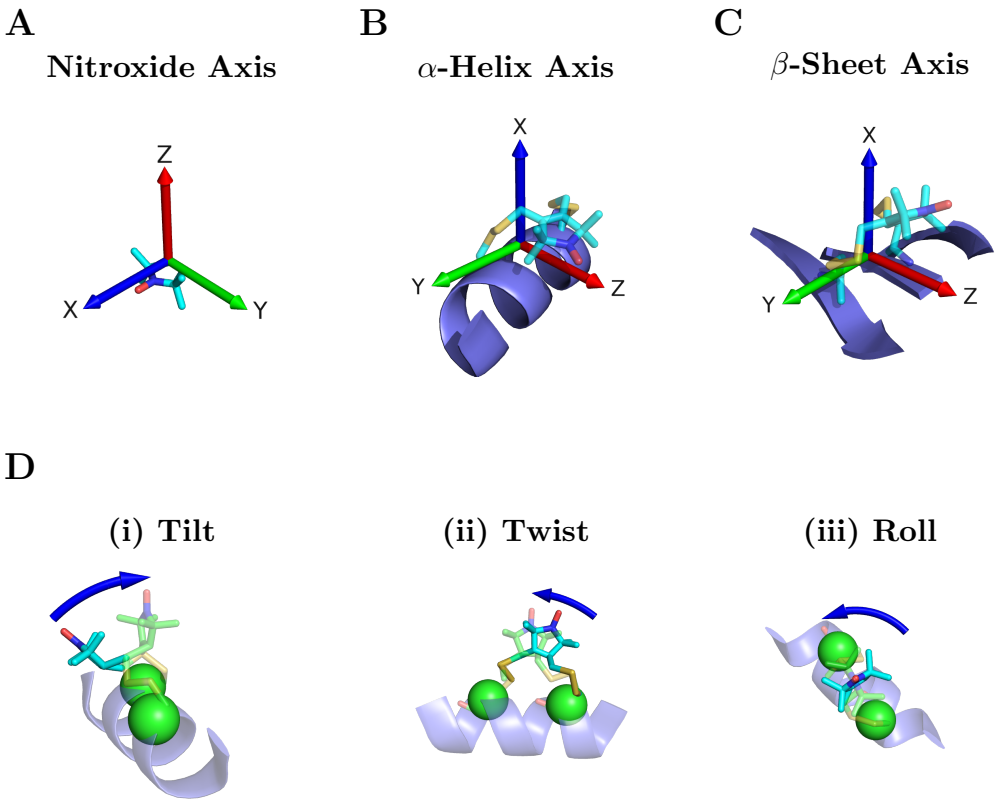

Figure 3.3: (top) Images of axes assigned to the nitroxide (A), α-helix (B), and β-sheet (C), (bottom) diagrams demonstrating the motions that the Tilt (D.(i)), Twist (D.(ii)) and Roll (D.(iii)) represent.

3.3.4.2 Measuring angles

Angle distributions were determined by aligning the origins of the nitroxide and secondary structure axis sets. The Tilt, Twist and Roll angles represent three rotational transformations that align the nitroxide axes with the secondary structure axes.

The rotational transformations were carried out by first rotating the nitroxide axes anti-clockwise around the y-axis to place the nitroxide x-axis in the y-z plane of the secondary structural axes set, with the angle of the rotation recorded as the Tilt. Secondly, the nitroxide axes were rotated anti-clockwise around the z-axis of the secondary structural to align the x axes from the nitroxide and secondary structural axes sets, with the angle of this rotation recorded as the Twist. Finally, the nitroxide axis was rotated anti-clockwise around the x-axis of the secondary structural axis to align the y-axes of the nitroxide and secondary structural axis. Angles were measured for all the different modelled conformations of Rx with angle distributions produced by making histograms with 4° bins.

3.4 Endo I Sample Preparation

3.4.1 Endo I Mutants

Endonuclease I (Endo I) N-terminal mutants were made using QuickChange site directed mutagenesis (Stratagene, see figure 3.4 for the typical reaction conditions) onto an Endo I coding sequence inserted in a pET19 vector (pET19-endoI). Mutants success was determined using DNA sequencing (Dundee, MRC PPU sequencing services).

A Typical PCR Cycle

Temperature (°C)	time (minutes:seconds)
95	0:30
16 cycles	
95	0:30
55	0:30
55	1:00
68	10:00

B Typical PCR Reaction

Reagent	Volume/ Amount
10 x Reaction Buffer	2.5 μl
DNA template	10 ng
Forward Primer	62.5 ng
Reverse Primer	62.5 ng
10 mM dNTP Mix	0.5 μl
ddH_2O	up to 25 μl

C 10 x PCR Reaction Mix

Reagent	Concentration (mM)
Tris-HCl (pH 8.8)	200
$MgSO_4$	20
KCl	100
$(NH_4)_2SO_4$	100
Triton X-100	1%
BSA (nuclease-free)	1 mg ml^{-1}

Figure 3.4: PCR temperature cycle (A), reaction mix (B), and buffer mix (C).

3.4.2 Endo I Protein Expression

pET19-endoI was expressed in BL21(DE3)pLysS cells, with cell transformations performed by standard protocols. Cell cultures were grown up in Lysogeny Broth (LB) media containing 50 μg ml^{-1} ampicillin for selection. The culture was grown to an OD_{600} of 0.6 at 37 °C, where expression was induced by the addition of 100 μl of 1 M isopropyl β-D-1-thiogalactopyranoside (IPTG). Induced cultures were left to express for 4 hours at 30 °C.

Cells were harvested by centrifugation (4550 x g rcf, for 40 minutes), the media was removed from the cell pellets and the cell pellets were suspended in PS buffer (50 mM sodium phosphate (pH 8.), and 1 M NaCl) supplemented with a complete protease inhibitor set (Roche).

Cells were lysed by sonication and the cell debris was pelleted by centrifugation (45000 x g rcf for 30 minutes at 4 °C). The solvent layer was removed and Endo I was purified by affinity chromatography using a Nickel-loaded HisTrap HP column (GE Healthcare). The N-terminal histidine tagged Endo I was eluted from the column using a gradient between 10 mM and 500 mM imidazole in PS buffer.

3.4.3 Endo I His Tag Removal and Labelling

The His tag was removed by digestion with shTEV Protease (a kind gift from Helena Berglund (van den Berg et al., 2006)), with the sample extensively dialysed against dialysis buffer (50 mM Tris-HCl (pH 8), 100 mM NaCl, and 1 mM dithiothreitol (DTT)).

Protein concentrations were determined using the A_{280} with the absorption coefficient, ε = 49500 M^{-1} cm^{-1} for the Endo I dimer determined using the ProtParam tool in ExPaSy (Gasteiger et al., 2005). Cysteine residues were reduced for labelling by incubating in 20 mM DTT (added from a 1M stock solution) at room temperature for 1 hour. The reducing agent was removed by anion exchange chromatography using a sephadex SP column (GE Healthcare). Endo I was reacted with a ten-fold excess of MTSL at protein concentrations of 20 μM to 100 μM of dimer for 1 hour at 4 °C. Unreacted MTSL was removed by dialysis against ddH_2O and the protein sample was lyophilized for storage.

3.4.4 DNA Synthesis

DNA was synthesised using phosphoramidite chemistry on a 394 DNA/RNA synthesizer (Applied Biosystems). Deprotected DNA was purified using gel electrophoresis on 10 % to 20 % w/v polyacrylamide in Tris-borate (pH 8.5) and 2 mM EDTA (TBE buffer) with 8 M urea. DNA was recovered using electro-elution and ethanol precipitation; separate DNA stands were assembled into four-way junctions by mixing stoichiometric quantities of each strand. DNA strands were annealed by incubation in annealing buffer (20 mM Tris-HCl (pH 8), and 50 mM NaCl) for 5 minutes at 85 °C, followed by slow cooling. DNA junctions were purified by gel electrophoresis in polyacrylamide under non-denaturing conditions, and eluted from the excised gel fragment by diffusion into buffer. DNA was ethanol precipitated with the resulting pellet suspended in D_2O.

3.4.5 Endo I EPR Sample Preparation

PELDOR samples were prepared by suspending lyophilised spin labelled Endo I samples in 50 µl of D_2O containing 20 mM HEPES (pH 7.5), 100 mM NaCl, and 20 mM $CaCl_2$ (Ca^{2+} ions were used instead of Mg^{2+} to prevent Endo I cleaving DNA upon binding).

Samples were diluted in equivalent volumes of D_8 glycerol (50 µl) producing a final volume of 100 µl. For samples with DNA the DNA junction was added in a concentrated solution in D_2O directly to the protein before addition of glycerol. Samples for CW-EPR spectroscopy were prepared in the same buffer and at the same concentrations as PELDOR. In this case H_2O was used in place of D_2O, no glycerol was added, and samples were made up to 25 % Ficoll PM 70 to increase viscosity.

3.5 MuRF 1 Sample Preparation:

3.5.1 MuRF 1 Protein Expression

pET28a plasmids containing the MuRF 1 coiled coil domain and COS-Box coding sequence (pET28a-MuRF 1, a kind gift from Owen Pornillos) plasmids were transformed into BL21 (DE3) EColi. Cell cultures were grown in LB media containing 50 mg ml^{-1} kanamycin for selection. Cultures were incubated at 37 °C to an OD_{600} of 0.8, and expression was induced using 0.2 mM IPTG. MuRF 1 Expression was carried out for 3 hours and 30 minutes at 37 °C and cells were harvested by centrifugation (5020 x g rcf for 45 minutes at 4 °C).

Media was removed and the cell pellet was suspended in 30 ml of lysis buffer (50 mM Tris-Base pH 8.0, 500 mM NaCl, 5 % glycerol, and 5 mM β-mercaptoethanol), Cells were burst by freeze thawing followed by sonication on ice using six 10 second pulses with 40 second pauses between each pulse.

3.5.2 MuRF 1 Affinity chromatography

Cell debris was removed by centrifugation (38'000 x g rcf for 45 minutes at 4 °C), followed by filtering the solute through a 0.45 µm pore sized membrane filter to remove any remaining debris. MuRF 1 was purified by affinity chromatography using a 1 ml HisTrap ff nickel column (GE healthcare); the solute was flowed through the column at 1 ml min^{-1} for 1 hour at 4 °C to bind MuRF 1. The column was washed with 250 ml of wash buffer (50 mM Tris pH 8.0, 500 mM NaCl, 5 % glycerol, 30 mM imidazole and 5 mM β-mercaptoethanol), and MuRF 1 was eluted using 20 ml of elution buffer (50 mM Tris (pH 8.0), 100 mM NaCl, and 1 M imidazole).

3.5.3 MuRF 1 SUMO Tag Cleavage

The SUMO tag was cleaved from the elute by the addition of 1:100 mass ratio of ULP 1 protease: MuRF 1. The cleavage reaction was dialysed in a 3.5 kDa cut off membrane tube against 1 L of dialysis buffer (30 mM Tris pH 8.0, 100 mM NaCl, 5 % glycerol, and 5 mM β-mercaptoethanol) at 5-7 °C overnight. A 1 ml nickel column was used to remove the SUMO tag, leaving cleaved MuRF 1cc in the flow through. The success of cleavage and purification was assessed using 12 % SDS-PAGE.

3.5.4 Labelling MuRF 1

Samples were incubated at room temperature for 2 hours with 5mM DTT to reduce cysteine residues. DTT was removed using superose S12 size exclusion chromatography (Pharmacia) in labelling buffer (20 mM HEPES pH 6.8, and 100 mM NaCl). MuRF 1 constructs were labelled by incubating the sample at room temperature for 2 hours with 10 molar equivalents of MTSL to labelling sites. Samples were dialysed against 1 L of PELDOR buffer (20 mM HEPES pH 8.0, and 100 NaCl) overnight in 3.5 kDa cut-off membrane tubing at 5 to 7 °C with 2 buffer changes at 3-hour intervals the following day.

Dialysed samples were concentrated down to 100 µl using 5 kDa cut off concentration columns. Buffer exchange was performed by diluting the sample in a 1:4 v/v ratio with 2 x PELDOR buffer in D_2O, concentrating the sample down to 100 µl using a 5 kDa cut-off concentration column, then repeating the dilution and concentration a further 4 times.

Concentrations were performed using 30-minute centrifugation pulses at 7500 x g rcf at 4 °C, with the final concentration step repeated until the samples volume was reduced to 50 µl. PELDOR samples were mixed in a 1:1 v/v ratio with D_8 glycerol, transferred to quarts tubes, and flash frozen in liquid nitrogen.

3.6 Trim 25 Sample Preparation

3.6.1 Trim 25cc Mutants:

The coding sequence for the coiled coil and linker domains of Trim 25 was inserted into a pET28a vector containing a His_6 tagged-SUMO leader sequence (pET28a-

Trim 25cc, a kind gift from Owen Pornillos*). Natural cysteine residues were removed and a series of constructs with different cysteine mutations were made using QuickChange site directed mutagenesis (Qiagen, see figure 3.4 for typical PCR conditions). The success of each cysteine mutation was determined by sequencing the plasmid DNA (Dundee, MRC PPU sequencing services).

3.6.2 Deuterated Trim 25cc Expression:

pET28a-Trim 25cc plasmids were transformed into Rosetta 2 cells (home grown from a Novagen stock, made competent using the Inoue Method (Inoue et al., 1990)) Cells were used to inoculate 0.5 ml of spectra 9 media containing 30 μg ml^{-1} kanamycin and 30 μg ml^{-1} chloramphenicol for selection. 0.5 ml cultures were incubated at 37 °C until they reached an OD_{600} greater than 1. 100 ml cultures of spectra 9 media containing the same concentrations of kanamycin and chloramphenicol were inoculated with the small cultures and grown to an OD_{600} of 0.8 at 37 °C. Expression was induced by adding 1 ml of 1 M IPTG and the protein was left to express at 37 °C for 9 hours. Cells were harvested by centrifugation (4845 x g rcf for 40 minutes at 4 °C). Media was removed and the cell pellet was suspended in 10 ml of lysis buffer (300 mM NaCl, 50 mM Tris, and 5 mM β-mercaptoethanol; pH 9.0), cells were lysed by freeze thaw followed by sonication on ice using six 10 second long pulses, each followed by a 40 second rest. Cell debris and the solvent layers were separated by centrifugation at 45000 x g rcf and 4 °C for 45 minutes and the solute was filtered through a 0.45 μm pore syringe filter to remove any remaining cell debris (Sartorius Minisart syringe filters, hydrophobic).

3.6.3 Trim 25cc Purification and Labelling

Affinity chromatography was carried out using a 1 ml nickel column by circulating the fraction through the column for 1 hour at 1 ml min^{-1} at room temperature. The column was washed with 500 ml of wash buffer (25 mM Tris, 100 mM NaCl, 20 mM imidazole and 5 mM DTT), followed by 40 ml of degassed wash buffer without reducing agents to remove DTT (25 mM Tris, 100 mM NaCl, and 20 mM imidazole). Labelling was performed on the column using labelling buffer (100 nmoles of MTSL in 2 ml of wash buffer without DTT). The nickel columns were incubated in labelling buffer for 1 hour with the buffer mixed by pushing the buffer back and forth through the column 10 times every 15 minutes. Excess MTSL was removed by washing the column with 40 ml of wash buffer. The sample was eluted using 10 ml of elution buffer (25 mM Tris pH 8.0, 100 mM NaCl, and 400 mM imidazole), with the flowthrough collected in 0.5 ml fractions.

3.6.4 Trim 25cc PELDOR Sample Preparation

SDS-PAGE was used to determine which fractions of the elute contained Trim 25cc. The elute was pooled and concentrated down to 1 ml using a 20 ml 10 kDa cut off concentration column (Millipore) by centrifugation (20-minute pulses at 2500 x g rcf with samples mixed between pulses). Further concentration to 100 µl was performed using a 0.5 ml concentration column (7500 x g rcf for 30 minutes).

Buffer exchange into PELDOR buffer (20 mM Tris, and 100 mM NaCl, pH 8.0 in D_2O) was carried out in the 0.5 ml concentration column by making up a 4:1 dilution of PELDOR buffer to sample, concentrating the sample down to 100 µl

using the same conditions as before, and repeating the dilution and concentration 4 times.

PELDOR samples were made using a 1:1 ratio of protein sample to D_8 glycerol transferring 100 µl of the mixture to a Q-band EPR tube (Sigma Z567345-1EA), and flash freezing in liquid nitrogen. Samples were stored in a 70 K gas phase nitrogen fridge until PELDOR experiment could be run.

Further Information:

*The plasmid vector was subcloned from pFlagCMV2-EFP, gifted to Owen Pornillos by Dong-Er Zhang (Addgene Plasmid 12449) (Fleissner et al., 2011).

3.7 Vps 75 Sample Preparation

3.7.1 Vps 75 Plasmid Preparation

The coding sequence for Vps 75 was inserted into a pET30a plasmid vector (pET30a-Vps 75, a kind gift from Tom Owen-Hughes) with a TEV-protease cleavable His tag. Natural cysteine residues within Vps 75 were mutated to either alanine or serine, and double cysteine mutations were introduced at the desired sites using QuickChange site directed mutagenesis, with both cysteines introduced in the same primer where possible. The success of mutations was tested using DNA sequencing (MRCPPU, Collage of life sciences, University of Dundee, Scotland) on a Biosystems model 3730 automated capillary DNA sequencer using Applied Biosystems Big-Dye Version 3.1 chemistry.

3.7.2 Vps 75 Expression

pET30a-Vps 75 plasmids were transformed into Rosetta 2 cells and cultures were grown in LB media containing 50 μg ml^{-1} of kanamycin and chloramphenicol. The culture was incubated at 37 °C until it reached an OD_{600} of 0.8. Vps 75 expression was induced with 1 mM IPTG and cultures were left to express at 24 °C overnight.

3.7.3 Vps 75 Harvesting

Cells were harvested by centrifugation (4845 x g rcf for 20 minutes at 4 °C), the cell pellet was suspended in 30 ml of binding buffer (20 mM Tris-HCl (pH 7.5) and 500 mM NaCl) with the protease inhibitors E64, pepsin, AEBSF and aprotinin. Cells were lysed by flash freeze thawing and sonication using six 10-second pulses with 40-second pauses, with the suspension kept on ice. Cell debris was removed by centrifugation (35562 x g rcf for 30 minutes), followed by filtering the solute through a 0.45 μm pore sized filter.

3.7.4 Vps 75 Purification

The filtered solute was loaded incubated with 2 ml of his-pur cobalt resin (Thermo Scientific) at 5 to 7 °C for 1 hour. Beads were washed with 40 ml of binding buffer, followed by 40 ml of wash buffer (binding buffer with 25 mM Imidazole), and Vps 75 was eluted from the column using 8 ml of elution buffer (binding buffer with 500 mM Imidazole). Fractions from the column flow through were tested for Vps 75 using SDS-PAGE with a 12 % resolving gel and protein bands were observed with a coomassie stain. Elute fractions containing Vps 75 were concentrated to a volume of 1 ml using 10 kDa cut off membrane concentration columns (20 ml, Millipore).

3.7.5 Labelling Vps 75 with Rx

Concentrated samples were made up to 50 mM DTT and incubated at room temperature for 1 hour. DTT was removed using size exclusion chromatography on a Sephadex S75 column in binding buffer. Fractions containing Vps 75 were pooled and protein concentrations were determined using the A_{280} (ε = 49850 M^{-1} cm^{-1}, determined using ExPaSy). A 20 mM stock of 3,4-Bis-(methanethiosulphonylmethyl)-2,2,5,5-tetramethyl-2,5-dihydro-1H-pyrrol-1-yloxy (3,4 bis MTSL) in dimethylformamide (DMF) was added to the sample in 0.5 mole equivalents to Rx binding sites at 5 minute intervals until the amount of label reached a final equivalency of 2:1, 3,4 bis MTSL to Rx binding site. The labelling reaction was left incubating at room temperature for 1 hour after the final 3,4 bis MTSL addition.

3.7.6 Vps 75 PELDOR Sample Preparation

Excess spin label was removed by dialysis against 1 L of binding buffer at 5-8 °C overnight. Buffer was then exchanged, left for three-hours, exchanged once more and the sample removed after a further 3 hours. PELDOR samples were prepared by concentrating the dialysed samples down to approximately 100 µl using a 10 kDa cut off concentration column (0.5 ml, Millipore) by centrifugation at 7500 x g rcf, 10 °C, for 20 minutes. The buffer was exchanged by adding 400 µl of double concentrated binding buffer in D_2O, concentrating the sample down to 100 µl in the same manner as before. Buffer exchange was carried out a total of 5 times, with the sample volume reduced to 50 µl in the final concentration step. The exchanged 50 µl samples were made up in a 1:1 ratio with D_8 glycerol, transferred to a 4.0 mm

OD, 3.0 mm ID Quarts tubes (Norell S-4-EPR-250S) and flash frozen in liquid nitrogen.

3.7.7 Vps 75 CW-EPR Sample Preparation

Samples for CW-EPR were further dialysed against 500 ml of binding buffer using a 10 kDa cut off membrane at room temperature, with the buffer exchanged twice daily for two weeks to remove free spin label from the sample. To prevent cell growth in dialysis samples and the dialysis buffer were made up to 0.05 % w/v and 0.005 % w/v sodium azide respectively. Samples were concentrated using a 10 kDa cut off concentration column to a typical concentration of 150 μM in 30 % w/w sucrose. 10 μl of samples were transferred to 0.64 mm ID, 0.8 mm OD borosilicate capillary tubes, sealed with silicone gel for CW-EPR measurements.

Chapter 4: Determining the Structure of the 16 N-terminal Residues of Endonuclease I.

4.0 Summary

The 16 residues of the Endonuclease I (Endo I) N-terminal tail, a Holliday junction-resolving enzyme, are important for its resolvase activity. These residues are not resolved in current crystal structures of Endo I bound to DNA, implying the Endo I N-terminus is flexible. A combination of CW-EPR and PELDOR data presented in this chapter, have allowed hypothesise to be made on the binding location and conformation of the Endo I N-terminal tail when bound to DNA.

These are:

- Residues between 15 and 10 bind the cleaved DNA helix, stabilizing the interaction between Endo I and the Holliday junction.
- Residues 1 to 10 of the Endo I N-terminus aid in either destabilizing the centre of the Holliday junction or stabilizing the cleavage reaction intermediate.
- A helical intrinsically disordered structure is formed within the first 10 N-terminal residues of Endo I, this structure is stabilized upon binding of Endo I to the Holliday junction (Freeman et al., 2016).

4.1 Introduction

4.1.1 The Function of Endo I

The four-way, or Holliday, DNA junction is an important structural intermediate in homologous recombination (Potter and Dressler, 1976). This process is important in double strand DNA break repair, as well as meiosis in eukaryotes (Meselson and Radding, 1975; Schwacha and Kleckner, 1995). The structural recognition and cleavage of the DNA four-way junction in a conserved manner is required for its resolution. The phage T7 endonuclease I (Endo I) has been observed to bind DNA

four-way junctions in a structurally selective manner, with a disassociation constant of ~1nM (Déclais et al., 2006). In solution, Endo I is a strongly associated homodimer that cleaves the DNA four way junction in a sequential manner at two symmetrical sites (Parkinson and Lilley, 1997).

4.1.2 Endo I Crystal Structures

A series of crystal structures for the Endo I homodimer in isolation or bound to DNA have been resolved. These demonstrated a limited structural flexibility for Endo I, with the structure undergoing a small conformational change upon binding DNA (Freeman et al., 2011; Hadden et al., 2007). The Endo I active site consisted of two metal ion centres, and was made up from residues of both monomers forming the homodimer (Asp55, Glu65, and Lys67 from one monomer; and Glu20' from the opposing monomer) (Freeman et al., 2003). The DNA four-way junction is bound to Endo I by the two metal centres and a series of basic residues within the Endo I homodimer's DNA binding grooves. The Endo I DNA binding grooves are formed of two 30 Å long channels aligned perpendicular to one another; causing the channels to favourably bind the four-way DNA junction in a coaxial conformation (Déclais et al., 2003).

4.1.3 The N-Terminal Residues

Biochemical studies have found deletion of the first 16 N-terminal residues of Endo I (Endo I Δ16) increased its affinity for the DNA four-way junction (Freeman et al., 2013). However, spectroscopic studies showed a decrease in the bilateral cleavage of the DNA four-way junction for Endo I Δ16. This indicated the first 16 N-terminal residues had an important role in the catalytic activity of Endo I (Déclais et al., 2003; Hadden et al., 2001).

4.1.4 SDSL of Endo I

To investigate the flexible N-terminal region of Endo I, site directed spin labelling (SDSL) was used to introduce the nitroxide label MTSL at a series of sites within residues 1 to 16 of Endo I. This formed the side chain R1, that allowed the investigation of differences between unbound Endo I and Endo I bound to the DNA four-way junction at labelled positions on the N-terminal tail. Changes in mobility were interrogated using CW-EPR, and changes in distances across the homodimer were interrogated using PELDOR. The spectral line shape of CW-EPR was used to determine the mobility of R1 (Belle et al., 2008). Within a protein structure this mobility is affected by both the flexibility of the protein backbone, and restrictions imposed on the spin label by the surrounding protein tertiary structure.

Endo I was labelled with MTSL at residues 2, 6-10, 12, 14, and 16 on the N-terminal tail. In addition, residue 29 was labelled to provide data on a site observed in the crystal structure, this allowed the distribution of R1 to be modelled at this site. Remaining sites were chosen to provide a good coverage of residues 2 to 16, where possible excluding large hydrophobic residues such as F15 (figure 4.1).

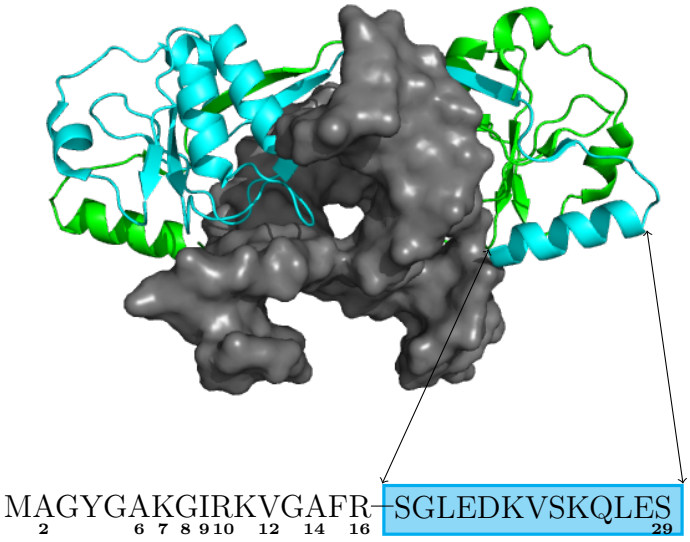

Figure 4.1: The crystal structure of Endo I (PDB ID: 2PFJ) along with sequences of the flexible N-Terminal tail, shown with labelling sites marked, and the N-terminal helix highlighted in cyan.

4.2 CW-EPR

Figure 4.2 shows CW-EPR spectra from R1 positioned within the first 16 N-terminal residues and residue 29 of Endo I free in solution (red) or bound to DNA (black). Initial examination of CW-EPR spectra showed significant differences between Endo I free in solution and the DNA bound counterpart for the majority of the 16 N-terminal R1 binding positions. Differences in the spectra from Endo I bound to DNA, compared to Endo I free in solution included: the appearance of a low field peak at 3489 G and a high field trough at 3559 G, indicated by dashed lines in figure 4.2; and broadening of the central line width.

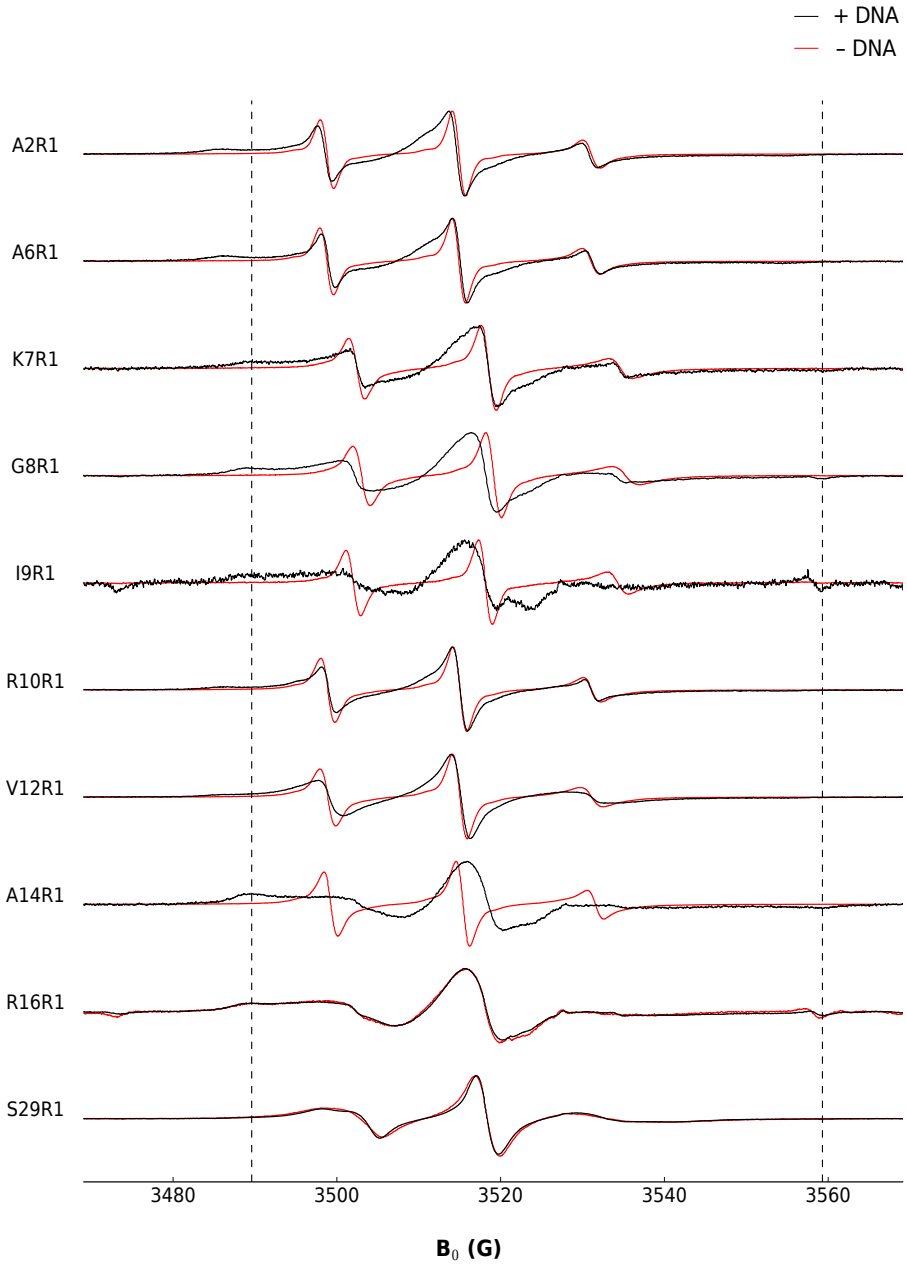

Figure 4.2: CW-EPR spectra for R1 bound within the first 16 N-terminal residues of Endo I, both free in solution (red) and bound to DNA (black). The dashed lines indicate the average position of the low field peak and high field trough for labelling sites with Endo I bound to DNA. In all cases the CW-EPR spectra were normalised so that the central peaks were all the same height, with different Endo I constructs shown on the left-hand side of the spectra.

4.2.1 Line Broadening

Line broadening within CW-EPR may be caused by either: dipolar interactions between spin labels within 20 Å of one another; or reduction in the nitroxide's motion. PELDOR data (figure 4.4) showed Endo I labelled at sites A2R1, K7R1 or G8R1 had electron spin-spin distances of 20 Å or less across the homodimer, allowing dipolar interactions to broaden CW-EPR line shapes. Additionally, spectral line broadening at other positions are features of faster correlation times (τ_c) for R1 bond to Endo I free in solution when compared to R1 bound to the Endo I / DNA four-way junction complex.

The presence of the 3489 G peak and 3559 G trough in CW-EPR spectra indicated the correlation time of R1 was close to the rigid limit of CW-EPR (τ_c > 50 ns). These features were observed for spectra from R1 positions within the first 16 N-terminal residues of Endo I bound to DNA, and where absent in spectra from the same labelling sites on Endo I free in solution. A 3489 G peak along with a 3559 G trough in spectra with narrow central line widths (for example A2R1 and A6R1), indicate the presence of R1 conformations with different correlation times at these sites. CW-EPR spectra from samples with multiple different correlation times are none trivial to fit using programs such as EasySpin (Stoll and Schweiger, 2006), this is a result of the number of unknown parameter required for the fit.

4.2.2 Label Mobility

Lower correlation times in CW-EPR spectra from R1 labelling sites on Endo I bound to DNA, when compared to the equivalent sites on Endo I free in solution, resulted partly from a reduction in protein backbone flexibility. This is exemplified

by the CW-EPR spectra of Endo I S29R1, where the protein backbone has been made rigid by forming an α-helix observed in Endo I crystal structures (PDB IDs: 2PFJ (Hadden et al., 2007), 1FZR (Hadden et al., 2001), and 1M0[D/I] (Hadden et al., 2002)). CW-EPR spectra showed greater spectral line widths, as well as the appearance of a 3489 G peak and 3559 G trough, from labelling sites within residues 2 to 16 from Endo I bound to DNA when compared to Endo I S29R1. These features indicated a lower correlation time for R1 bound to sites within residues 2 to 16 of Endo I bound to DNA than Endo I S29R1. The reduction in correlation time results from a reduction in the motion of R1, a result of the surrounding biomolecules structures restricting the mobility of R1. The first 16 N-terminal residues are unresolved in the Endo I crystal structure bound to DNA (PDB ID: 2PFJ), indicating a flexible protein backbone. Combined with the presence of mobile and immobile features in the multi-component CW-EPR spectra at these sites, this suggests the protein backbone adopts an intrinsically disordered structure.

4.2.3 CW-EPR Observations

Although multiple components within the CW-EPR spectra complicate any analysis, semi-quantitative information can be obtained by measuring specific spectral features. Differences in the proportion of the rigid component within spectra from Endo I bound to DNA can be analysed by measuring the 3489 G peak height. A plot of the 3498 G peak height against R1 binding positions, showed the proportion of spectra in a rigid conformation adopted an oscillating feature between residues 6 and 12 of Endo I bound to DNA (figure 4.3, C). This suggested the protein backbone adopted a helical structure between these positions.

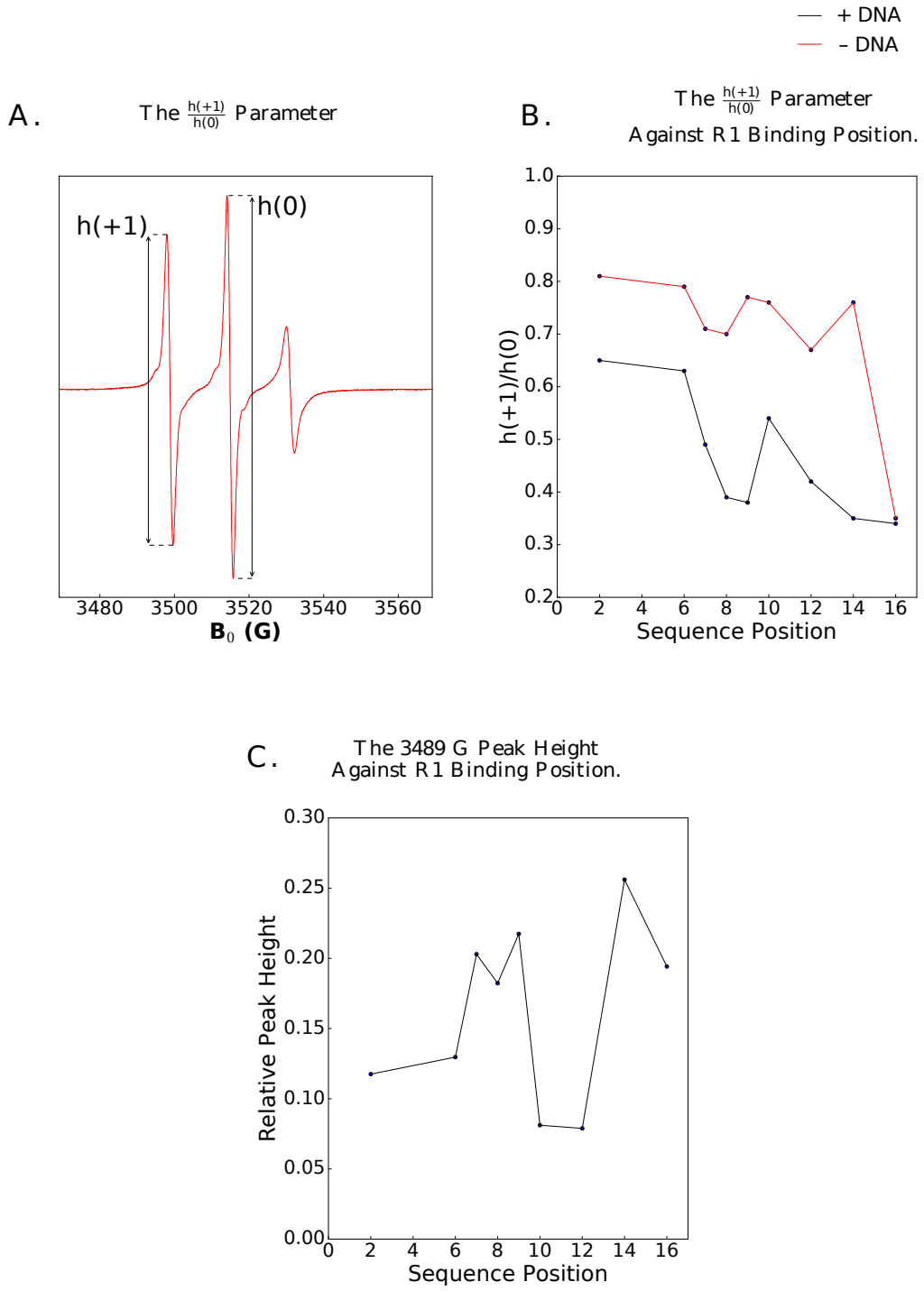

Figure 4.3: Graphs of different CW-EPR spectral components against the binding position. (A) The identity of the h(+1) and h(0) values of a CW-EPR spectra with the free in solution A2R1 spectra used as an example. (B) The changes to the h(+1)/h(0) parameter in relation to the different binding positions on the N-terminal tail of Endo I. The graph for free Endo I is shown in red and Endo I bound to DNA is shown in black. (C) A graph of the relative peak intensity of the 3489 G immobile peak taken for normalised CW-EPR spectra against their binding position on the N-terminal tail of Endo I bound to DNA.

4.2.4 the h+1/h0 Parameter

The $\frac{h(+1)}{h(0)}$ parameter (figure 4.3, A) gives a measurement of nitroxide mobility, where greater $\frac{h(+1)}{h(0)}$ values are representative of greater mobilities (Belle et al., 2008). Plotting the $\frac{h(+1)}{h(0)}$ parameter against the labelled residue allowed variations of nitroxide mobilities between labelling sites to be observed (figure 4.3, B). This plot showed labelling sites on Endo I bound to DNA had a consistently lower mobility than labelling sites on free Endo I up to residue 16, where the plots converged. Between residues 6 to 10 on the N-terminal tail of Endo I bound to DNA there is a significant dip in nitroxide mobility, which was partially replicated in Endo I free in solution. This dip corresponded to the rise in height of the 3489 G peak (figure 4.3, C), however, the oscillation observed in the 3489 G peak height plot was not present in the $\frac{h(+1)}{h(0)}$ plot. Additionally, the $\frac{h(+1)}{h(0)}$ parameter from the first 16 N-terminal residues of Endo I bound to DNA show three different motional regimes: a mobile region between binding positions 2 and 6; a structured region between residues 6 and 10; and a region of increased immobility between residues 12 and 16.

4.3 PELDOR

4.3.1 PELDOR Data

Endo I is a homodimer, as such, each spin labelling site produced a spin label pair. This allowed PELDOR to measure distances between Endo I monomer subunits labelled within the first 16 N-terminal positions (figure 4.4). Raw PELDOR data was background corrected and analysed using Tikhonov regularisation with the DeerAnalysis package for matlab (Jeschke et al., 2006). To determine an accurate

distance from PELDOR an oscillation is required. However, if the distribution of distances within the sample is too broad then destructive interference dampens these oscillations. Analysis of the initial drop from background corrected PELDOR data produces a mean distance, for oscillation free data these distances can be interpreted with care to give valuable insights into the underlying protein structure. Out of the first 16 N-terminal residues of Endo I all R1 binding positions except V12R1, A14R1, and R16R1 gave oscillation free data.

4.3.2 Mean Distances

Mean distances between ~56 Å and ~61 Å were measured from the initial drop for binding positions between residues 2 and 10 in Endo I free in solution. On binding DNA the length of distances for R1 bound to these sites reduced to between ~23 Å and ~32 Å (figure 4.5, A). A plot of the mean distance against the R1 binding site showed; distances from Endo I homodimers free in solution with the R1 binding site between residues 2 and 12 were consistently in the 55 Å to 61 Å range, with little variation between sites. Whereas, distances from R1 binding sites on Endo I bound to DNA were progressively shorter from residues 2 to 8, then progressively longer from residues 8 to 14 (figure 4.5, B.). This was interpreted as the N-termini of the Endo I dimer running antiparallel to one another upon binding DNA.

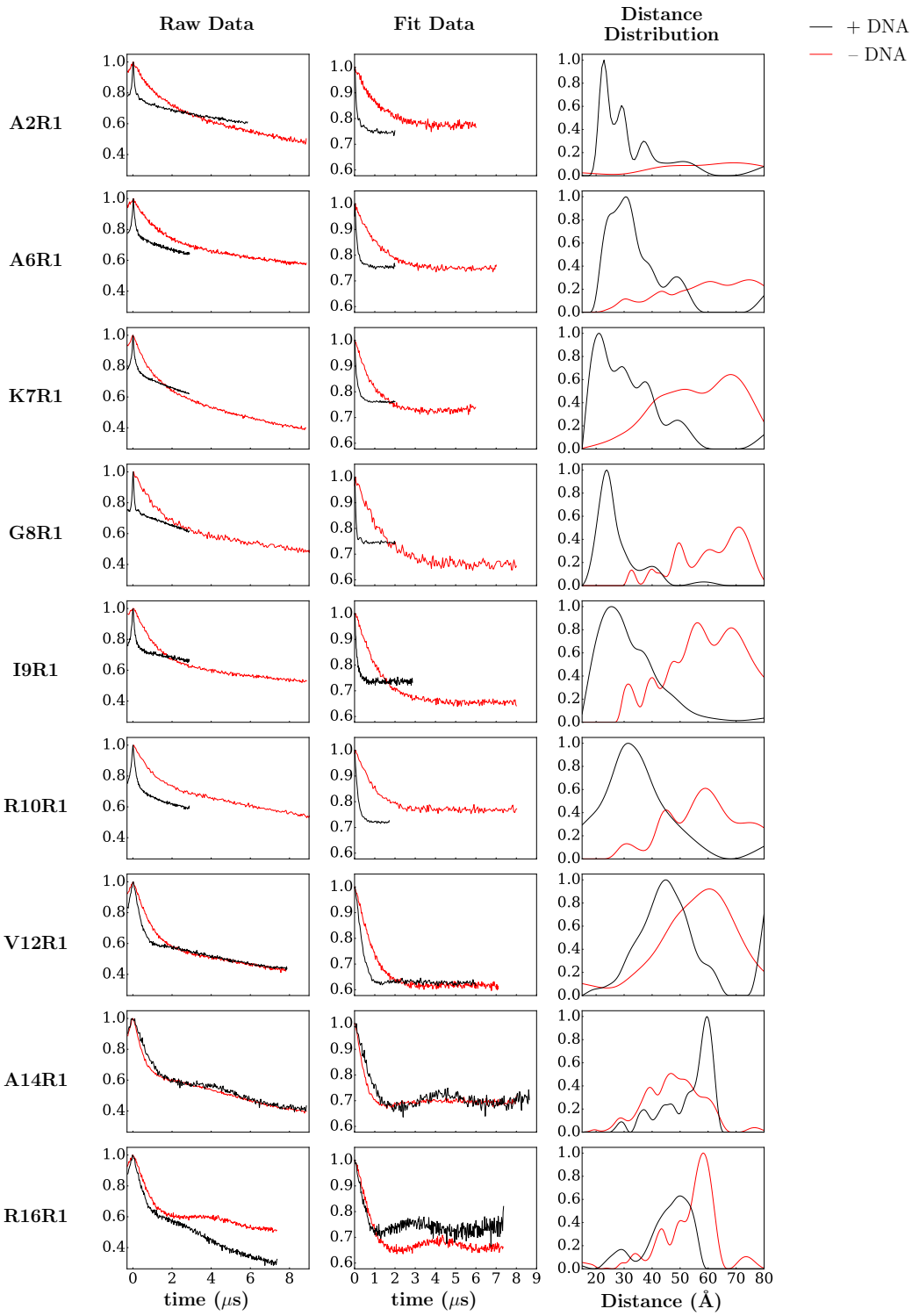

Figure 4.4: Raw, background corrected, and distance distributions from PELDOR measurements of R1 bound to the N-terminal of Endo I. Data from the protein free in solution is shown in red, and data from the protein bound to DNA is shown in black. Distance distributions have been normalised so that the highest peak height out of the free and DNA bound Endo I had a P(r) value of 1.0.

A.

Amino acid position	Distance -DNA (Å)	Distance + DNA (Å)
2	56.0	27.0
6	58.0	28.0
7	56.0	26.0
8	61.0	23.0
9	59.0	28.0
10	56.0	32.0
12	56.0	45.0
14	45.0	59.0
16	58.0	49.0

B.

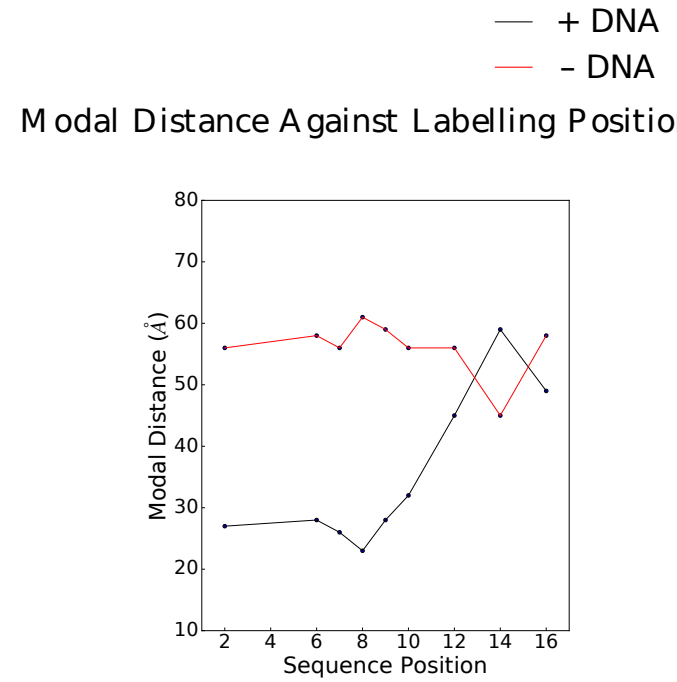

Figure 4.5: Modal distances from the PELDOR data, (A) A table of the modal PELDOR distances for Endo I free in solution (-DNA), and bound to DNA (+DNA) for R1 bound at different positions on the Endo I N terminus. (B) A plot of modal distances from the PELDOR data against R1 binding positions for Endo I free in solution (red) and bound to DNA (black).

4.3.3 Differences in mean distances

Changes in mean distances between sites could be assigned to different regions within the N-terminus of Endo I bound to DNA. Positions 10 to 14 showed steep distance gradients between sites, whilst residues 6 to 10 gave shallower gradients. Finally, there is little variation in distances between binding residues 6 and 2. These different distance regimes are at equivalent sites to the different motional regimes from the $\frac{h(+1)}{h(0)}$ parameter (figure 4.5, B). As such, variations in distances were likely a result of the Endo I N-terminal protein backbone adopting a series of different structural conformations upon binding DNA. A similar equivalence is observed when comparing the minor mean distance deviation for Endo I free in solution between residues 10 and 6, to the minor mobility difference indicated by the $\frac{h(+1)}{h(0)}$ parameter at these binding sites.

4.4 Endo I Structural Implications

4.4.1 PELDOR and Crystal Structure Information

In the crystal structure of the Endo I homodimer bound to DNA, the S17 to S29 α-helices were positioned in a manner that placed their N-termini towards the minor groove of the bound four-way DNA junction. A direct continuation of these helices by residues 1 to 16 would overlap with the position of bound DNA from the crystal structure. Additionally, R16 was resolved in one monomer of the Endo I crystal structure bound to DNA where R16 deviated from the S17 to S29 α-helical structure. Minimal differences between the bound and unbound Endo I crystal structures discounted different distance distributions between the two sites being

a result of dramatic changes in the structure of Endo I between these two conformations.

4.4.2 CW-EPR Data

The relative mobilities of each R1 binding position in relation to one another could be monitored by comparison of the h(+1)/h(0) parameters (figure 4.3). This comparison was used to identify trends in mobilities between R1 binding sites where absolute values regarding the nitroxides motion were unavailable. The key differences between Endo I samples in the presence and absence of DNA were higher h(+1)/h(0) parameters for labelling sites between residues 2 and 14 of Endo I without DNA, indicative of a greater label mobility at these sites. Additionally, the high mobility of R1 bound to Endo I in the absence of DNA from residues 2 to 14 implies the protein backbone was disordered within this region (figure 4.3). This was reflected by unresolved distances in PELDOR data from these labelling sites (figure 4.4). A dip in the h(+1)/h(0) parameter plot (figure 4.3) was observed for binding sites between residues 6 to 10, representing a noticeable reduction in label mobility within this region. This feature is more prominent in data from R1 bound to Endo I samples with DNA, than the equivalent samples without DNA. This reduction in mobility upon binding DNA was indicative of the protein backbone between residues 2 to 14 of Endo I becoming structured upon binding the DNA four-way junction. Additionally, the reduction in mobility could be caused by the labels motion being restricted by local structural features, notably the DNA four-way junction. Taken as a whole, the reduced mobility from Endo I bound to the DNA four-way junction, compared to Endo I free in solution, suggested the N-terminal tail is involved in binding.

The cyclic feature in the h(+1)/h(0) parameter between sites demonstrates cyclic changes in mobilities between residues 6 to 10 of Endo I bound to DNA. The most likely cause of these changes in mobility were interactions between R1 and the bound DNA four-way junction. This implied when Endo I was bound to DNA the protein backbone formed an intrinsically disordered helical structure between residues 6 to 10, located near the DNA four-way junction.

4.4.3 PELDOR Data

For the analysis of PELDOR data it was assumed Endo I bound the DNA four-way junction in a symmetric or nearly symmetric manner. This assumption was based upon the symmetry observed in both the bound and unbound crystal structures for Endo I. The assumption of a perfect symmetry is subverted by the sequential cleavage of the DNA four-way junction by Endo I, facilitated by residues 1 to 16. This is countermanded by the symmetric position of the DNA four-way junction within the Endo I bound to DNA crystal structure (PDB ID: 2PFJ), implying any binding to the un-cleaved junction would be symmetrical.

Mean distances derived from the initial drop in background corrected PELDOR data need to be treated with care. This was done by making observations based upon differences in the relative lengths of mean distances, as opposed to treating each mean distance as an absolute value. PELDOR data from Endo I samples containing DNA had shorter mean distances than data from samples not containing DNA, with little difference in mean distances between sites for samples not containing DNA. The mean distance for samples containing DNA reduced as the labelled position moved from residue 16 to residue 8, followed by a lengthening of

distances up to residue 6, with no significant difference in the mean distances between residues 6 and 2.

The lack of oscillations within PELDOR data is indicative of a disordered or intrinsically disordered protein backbone within residues 2 to 14 of Endo I. As the R1 binding site was moved along the protein backbone from residue 14 to residue 8 in Endo I bound to DNA mean distances shorten, and as R1 was moved along the protein backbone from residue 8 to residue 2 distances lengthened. This pattern of lengthening and shortening distances within a symmetric homodimer is the hallmark of the protein domain adopting an anti-parallel conformation.

4.4.4 R16R1 and A14R1 PELDOR data

Oscillations were observed in the PELDOR data for Endo I A14R1 and R16R1, allowing more accurate distances to be determined for these positions. The current crystal structure of Endo I bound to DNA displays R16 on a single chain (PDB ID: 2PFJ, chain B). To corroborate the crystal structure with PELDOR data the position of R16 was introduced onto the opposing side of the homodimer. This was done by replicating and aligning chain B (where R16 was resolved) to chain A (without R16 resolved) within the crystal structure. R1 was modelled onto these two R16 positions using the MTSL wizard plugin for pymol (Hagelueken et al., 2012) and the distance distribution between the modelled labels was acquired (figure 4.6, A). The distance distribution for Endo I R16R1 from the modelled data was compared against the experimental distance distribution from PELDOR data. The equivalence in these distance distributions showed the modelled distribution of R1 was representative of the experimental R1 distribution (figure 4.6, A). Endo I A14R1 bound to DNA produced a distance distribution at a longer range than Endo

I R16R1 bound to DNA, placing the nitroxide location from A14R1 at a greater distance from the dyad axis than the nitroxide location of R16R1 (figure 4.7, C). As a result, A14 would lie either in this region or within 5 Å of it (the R1 linker distance), placing the residue either outside or on the cusp of the four-way DNA junction.

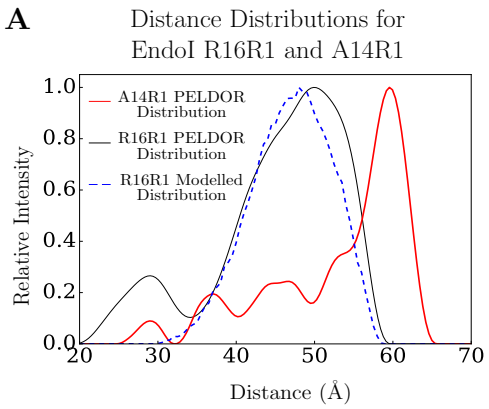

B

Previous Data By A.D.J.Freeman el Al. for DNA Binding and Reaction Kinetics of EndoI N-terminal truncations

EndoI N Terminal Deletion	DNA Binding K_d (pM)	Single Turnover Cleavage rate k_{obs} (10^{-3} s^{-1})
Full Length	3670 ± 560	300 ± 20
Δ9	700 ± 86	110 ± 10
Δ11	195 ± 18	140 ± 10
Δ16	300 ± 16	0.63 ± 0.003

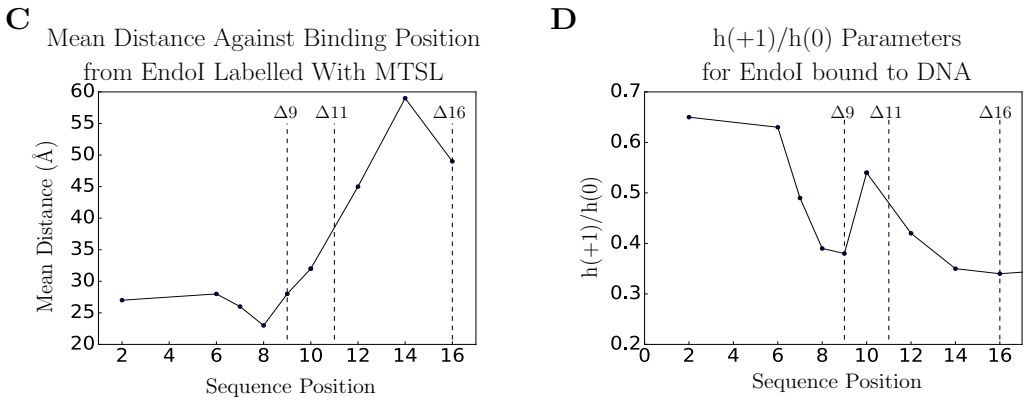

Figure 4.6: Data for the unstructured N-terminus of Endo I: (A.) Distance distributions from Endo I A14R1 (black) and R16R1 (red), alongside the modelled R16R1 distance distribution from Endo I modelled onto R16R1 resolved in the B-chain of the crystal structure (dashed blue line, PDB ID: 2PFJ); the opposing binding site was produced by aligning the B to the A chain and modelling R1 onto the resulting R16 position. (B.) A table showing the K_d of Endo I binding DNA and the Endo I DNA cleavage rates for various N-terminal truncations taken from a previous paper (Freeman et al., 2013). *(C.) The mean distance against binding position for the N-terminal labelling sites of Endo I bound to DNA. Dashed lines indicate locations of truncations performed in the previous study shown in (B). (D.) The h(+1)/h(0) parameter for Endo I bound to DNA, again dashed lines show the location of truncations measured in (B).*

4.4.5 Previous Kinetic and Binding Data for the N Terminus of Endo I

Different regions within the N-terminal tail of Endo I were observed by changes in distance distributions for R1 binding sites between residues 2 to 16 of Endo I bound to DNA. These two regions spanned residues 2 to 10 and residues 10 to 16, aligning with regions in the plot of changes in mobility against R1 binding sites. Changes in distances across the Endo I homodimer bound to DNA for R1 binding sites between residues 2 and 16, span similar regions to trends in DNA binding for Endo I constructs with truncations to the N-terminus ((Freeman et al., 2013), replicated in figure 4.6, B). These truncations showed the binding interaction between Endo I and DNA was stronger when the first 9 or 11 N-terminal residues were truncated (Endo I Δ9 and Endo I Δ11 respectively), than binding interactions involving full-length Endo I. Also shown was the binding interaction between Endo I and DNA was slightly weaker when the first 16 residues of Endo I were truncated (Endo I Δ16), compared to Endo I Δ11. Additionally, significant decreases in the DNA cleavage rate were observed when comparing Endo I with a full length N-terminal tail, to Endo I Δ9, Endo I Δ11 or Endo I Δ16 constructs. Endo I Δ16 gave the most dramatic reduction in the cleavage rate (figure 4.6, B), and showed a propensity for producing singly nicked DNA strands. Comparison between the DNA binding data for truncated Endo I constructs and changes in the distance and mobility gradients between labelling sites presented in this chapter, highlighted different function for the regions spanning residues 2 to 10 and residues 11 to 16 within the N-terminal tail of Endo I (figure 4.6, C and D).

4.4.6 Residues 11 to 16 of the Endo I N-terminal Tail

The region between residues 11 to 16 of Endo I bound to DNA gave a greater change in distance between labelling positions than the region between residues 2 to 10 (figure 4.6, C). Endo I labelling sites between residues 11 to 16 showed an increased mobility as the labelling site was moved from residue 16 to residue 11 (figure 4.6, D). This was a consequence of shifting the labelling site from the more rigid protein backbone at R16, towards a more mobile protein backbone.

Larger differences in distances for spin labelling sites between residues 11 to 16 compared to labelling sites between residues 2 to 10 of Endo I bound to DNA, suggested the protein backbone in this area was more elongated than the more compact structure present for the remainder of the N-terminal tail. The dramatic reduction in Endo I activity between Endo I Δ11 and Endo I Δ16 implied residues 11 to 16 were vital for directing the cleavage of the DNA four-way junction. More telling was the slight increase in the K_d of Endo I binding the DNA four-way junction for Endo I Δ16 compared to Endo I Δ11, this indicated residues 11 to 16 aided in binding the DNA four-way junction.

4.4.7 Residues 1 to 11 of the Endo I N-terminal Tail

Mean distances across the homodimer of Endo I bound to DNA from labelling sites between residues 2 to 10 of Endo I, had shallower distance gradients between consecutive labelling sites than mean distances from labelling sites between residues 11 to 16 of Endo I. Moving the labelling site from residue 2 towards residue 10 gave decreasing followed by increasing mean distances, indicating the N-terminal tails were anti-parallel to one another and crossed within this region of

Endo I bound to DNA. Additionally, the mobility of R1 for consecutive labelling sites within this region was cyclic, which resulted from reduction in the motion of R1 at regular intervals.

Truncation of the first 9 N-terminal residues of Endo I resulted in a decrease of the DNA cleavage rate, and an increase in the affinity between Endo I and the DNA four-way junction. The trend of an increased truncation of the Endo I N-terminal tail increasing the binding affinity and decreasing activity, was observed when Endo I Δ9 was compared to Endo I Δ11. A canonical feature of crystallised DNA junction resolving enzymes are protruding structural elements present in the DNA binding groove that insert themselves into the junctions dyad axis (Biertümpfel et al., 2007; Górecka et al., 2013; Liu et al., 2015). However, Endo I has proven to be an exception to this rule, with the undefined structure of the N-terminal tail a likely candidate to act as this canonical protrusion. This pattern in cleavage rate and DNA four-way junction binding for Endo I lends evidence that such a protrusion is present within the first 11 residues of the N-terminal tail, with the protrusion conducive to increasing the DNA cleavage rates while decreasing the binding affinity.

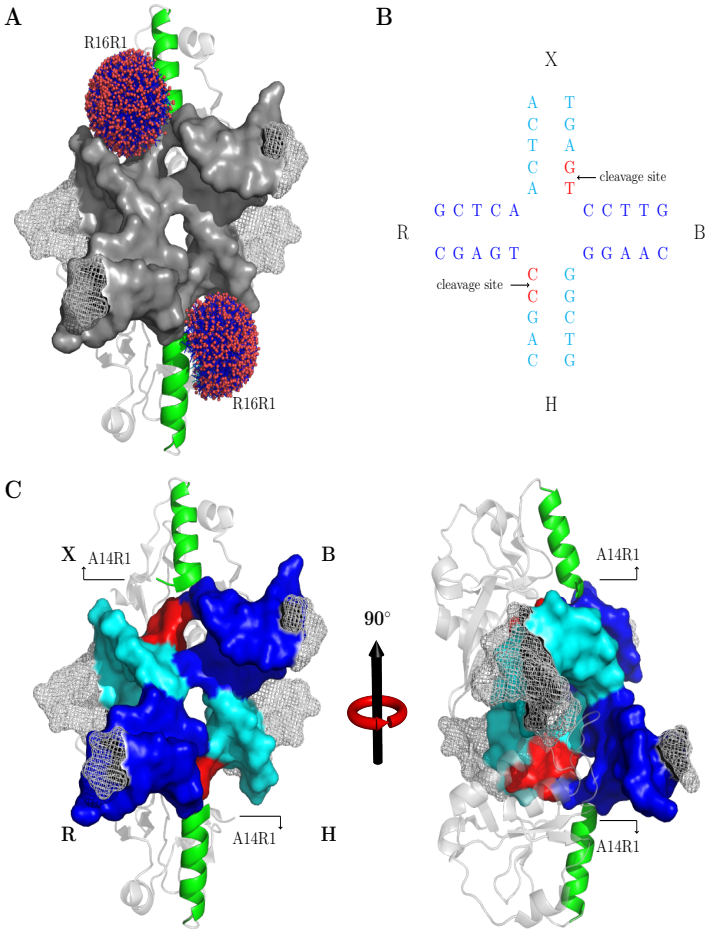

Figure 4.7: The crystal structure of Endo I bound to the four-way DNA junction (PDB ID: 2PFJ) showing likely locations of R1 bound at sites which gave oscillating PELDOR data (R16R1 and A14R1). (A.) A image of Endo I bound to DNA with chain B, where R16 was resolved within the crystal structure, aligned with chain A to determine the likely position of R16R1 across the homodimer (R1 distributions determined using MTSL wizard). (B.) Schematic of the four-way junction used in this study as well as the Endo I crystal structure, strands are labelled X, B, H, and R, with chains bound symmetrically to Endo I highlighted in the same colour (cyan for H and X, blue for B and R). Endo I cleavage sites are highlighted red and indicated by arrows. (C.) Endo I bound to DNA (PDB ID: 2PFJ) with the DNA coloured in the same manner as (B). The N terminus of the crystal structure (the S17 to S29 α-helix) is highlighted green and arrows indicate the likely area A14R1 is placed assuming symmetry across the Endo I homodimer is maintained.

4.4.8 Hypothesis of Function and Binding for the Endo I N-Terminal Tail

The mean distances and mobilities for the Endo I N-terminal tail (residues 1 to 16) indicate these residues formed intrinsically disordered structures, which bind the DNA four-way junction. The increased distance going from Endo I R16R1 to Endo I A14R1 supported the proposal that residues 16 to 14 looped away from the DNA junction. The preceding steep decline in mean distances between residue 14 to residue 10 of Endo I bound to DNA, implied the protein backbone in this region proceeded from residue 14 by placing neighbouring C-terminal residues towards the centre of the complexes' dyad axis. A likely position for this elongated structure is within the minor groove of the four-way DNA junction's X or H strand (figure 4.7, B and C). This located residues 16 to 10 of Endo I within the cleaved DNA strand, which was further supported by the dramatic drop in the cleavage rate for Endo I Δ16 compared to other truncations (figure 4.6, B). The slight increase in K_d for Endo I binding DNA from Endo I Δ11 to Endo I Δ16, implied the region spanning residue 16 to residue 10 is involved in the binding interaction between Endo I and the DNA four-way junction. Altogether, these observations suggested the function of residues 10 to 16 in Endo I is to stabilise the binding of Endo I to the DNA four-way junction, as well as keeping the DNA strand in position long enough to be cleaved.

Smaller variations in mean distances were noticed between labelling sites within residues 2 to 10 of Endo I bound to DNA compared to the variations in mean distances within residues 10 to 16. This suggested a more compact structure is formed in this region. Mobility data from CW-EPR implicated this compact structure contains some helical elements (figure 4.6, C and D; and figure 4.3, B).

The probable position for this structure would be within the central region of the four-way junction. This was because of both the proposed locations of residues 10 to 16 from Endo I bound to DNA, and the range of mean distances observed for labelling sites within residues 2 to 10. It was likely the helical structure was located within the minor groove of the DNA four-way junction's B or R chains (see figure 4.7, B and C). This location would lead to the observed cyclic nature of mobilities from labelling sites between residues 2 to 10 of Endo I bound to DNA.

It is noteworthy the proposed conformation positions residues 1 to 10 of Endo I in a prime location for disrupting the centre of the DNA four-way junction. This disruption was supported by the decreased binding affinity, and increased cleavage rate, for the full-length Endo I construct when compared to Endo I Δ9 or Endo I Δ11 truncations.

4.5 Conclusions and Prospects

The N-terminal tail of Endo I formed and intrinsically disordered helical structure when bound within the DNA four-way junction. The process of investigating the disordered N-terminal tail of Endo I has demonstrated how careful analysis of limited structural information from EPR, such as the h(+1)/h(0) parameter from CW-EPR and oscillation free PELDOR data, can be used for determining probable locations of intrinsically disordered structures. This was particularly informative when combined with other sources of structural and experimental data, such as the Endo I crystal structure and binding kinetics for various N-terminal truncations of Endo I. Looking at all these sources of data revealed what appeared to be two distinct regions in the N-terminal tail of Endo I. Residues 2 to 10 were

likely involved in disruption of the DNA four-way junction. Whereas residues 11 to 16 were likely involved in stabilizing Endo I binding the arm of the DNA four-way junction where the cleavage site was located.

A proposal for continuation of this work would involve constructing Endo I heterodimers containing a single mixed spin-spin distance between labelling sites. For the proposed project a crystallised position on Endo I such as S29, and one of the N-terminal tail residues presented in this study either within the same Endo I monomer, or on the opposite monomer within the Endo I dimer, would be labelled. Producing multiple mean distances for each labelling site on the N-terminal tail of Endo I, would allow triangulation of the labelled site into a rough location in space. It is hoped that further information pertaining to the area in space of each labelling site would support or reject the hypothesised location of the Endo I N-terminal tail when bound to DNA. Such a study would build on the work here in terms of both the biology and methodology for using EPR to determine transient structures within intrinsically disordered areas of proteins.

Chapter 5: Using EPR to Analyse the Conformation of the Coiled Coil Domain from MuRF 1.

5.0 Summary

Muscle regulation factor 1 (MuRF 1) is a member of the tripartite motif (Trim) family of proteins, which are defined by a domain conformation of a Ring finger, followed by one or two B-Boxes and a coiled coil domain. The coiled coil domain acts as a scaffold for the placement of RING, B-Box, and any C terminal domains required for the function of the protein. A fragment of the MuRF 1 coiled coil region had previously been crystallized and was observed to form a tetramer. This was at odds with observations from size exclusion chromatography-multi angle light scattering (SEC-MALS) data that the coiled coil region formed a dimer in solution. Within the coiled coil domain crystal structure there are six potential dimer conformations for the MuRF 1 coiled coil domain, two parallel and four anti parallel. PELDOR data has been presented in this chapter that determined the conformation for a construct of the MuRF 1 coiled coil and COS-Box domains. Differences in distance distributions between R1 labelling sites presented in this chapter implied the coiled coil domain of MuRF 1 was anti-parallel. Additionally, these distance distributions showed the COS-Box domain folded back towards the centre of the coiled coil domain, adopting a similar fold to crystal structures of coiled coil domains from other Trim family proteins deposited in the protein data bank.

5.1 Introduction

5.1.1 The Use of PELDOR in structural biology

Information from PELDOR is most valuable when used for filling in gaps left by other structural techniques. For example, in the previous chapter PELDOR was used to provide complementary structural data for the crystallised region of Endo I

(chapter 4). Another area where PELDOR can be used to complement crystal structures is to differentiate crystal packing artefacts from solution structures within a crystal lattice (Hammond et al., 2016). In this study PELDOR was used for determining conformations of the coiled coil domain from muscle-specific RING finger protein 1 (MuRF 1), a member of the tripartite motif (Trim) family of proteins.

5.1.2 Coiled Coil Domains

The coiled coil domain is a protein fold where one or more α-helices are coiled around each other to form an elongated rod (Crick, 1953; Lupas et al., 2017). Coiled coils are found within a wide variety of protein structures where they are involved in intra and extra cellular processes, often allowing proteins to function over long distances (Burkhard et al., 2001; Collins et al., 2003; Grütter and Luban, 2012; Kuhn et al., 2014). The greatest variation between coiled coil domains is whether they form parallel structures, with C and N-termini of the α-helices on the same ends of the coil; or anti-parallel structures, with C and N-termini of separate α-helices on opposite ends of the coiled coil (Monera et al., 1993). PELDOR is an effective technique for determining whether a homodimeric coiled coil domain is in a parallel or anti-parallel conformation. Labels within a parallel coiled coil shift in tandem with one another as the label site changes, giving a series of short distances which vary little between sites. Labels in anti-parallel coiled coils move either closer together or further apart at different labelling sites, resulting in a wide range of distances (figure 5.1, C and D) (Bagnéris et al., 2015).

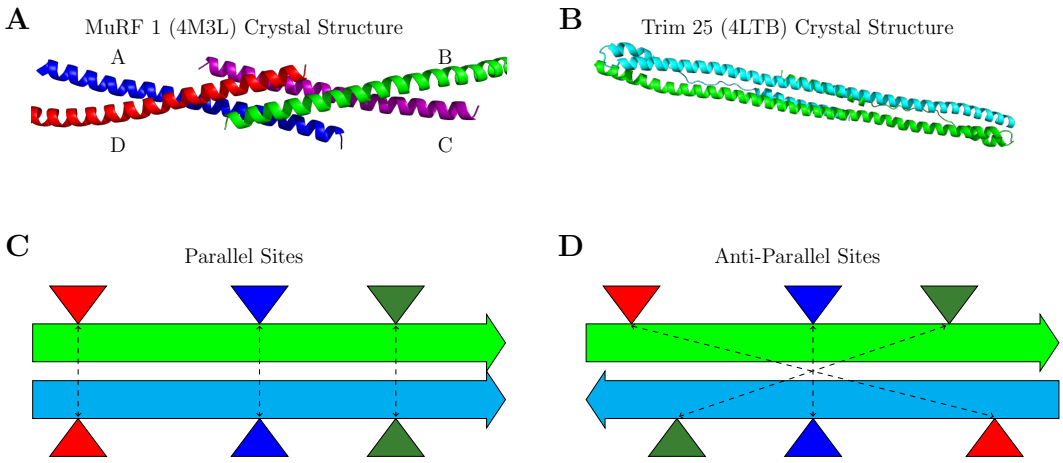

Figure 5.1: Images of the coiled coil domain crystal structures for MuRF 1 (A) along with Trim 25 (B), alongside cartoons illustrating the differences in distances present between parallel (C) and anti-parallel (D) coiled coil domains.

5.1.3 The Tripartite Motif (Trim) Protein Family

The Trim family of proteins are domain related, with each member containing a RING (R) (Freemont, 1993), B-Box (B), and coiled coil (CC) domain, present in an R-B-CC conformation when domains are labelled from the N terminus (Meroni and Diez-Roux, 2005). Trim proteins are the largest family of RING E3 ubiquitin ligases with functions including; marking proteins for degradation (Clarke et al., 2007); activating immune response pathways (Carthagena et al., 2009; Gack et al., 2007); and regulating gene expression (Loedige et al., 2013). The ubiquitin ligase activity of the Trim protein family is reliant upon the placement of the RING domain in relation to the binding domain for the target protein, usually found on the C-terminal of the RBCC motif (Esposito et al., 2017; Short and Cox, 2006). Domain placement is performed by the coiled coil domain, which acts as a scaffold for the protein's structure (Li et al., 2014). The B-Box domain has been observed to stabilize the coiled coil domain and enable formation of higher order Trim

multimers (Li and Sodroski, 2008; Massiah et al., 2006). There are currently no crystal structures of full-length Trim proteins, however, the protein data bank contains structures from a series of isolated domains (James et al., 2007; Mrosek et al., 2008; Sanchez et al., 2014; Weinert et al., 2015).

PELDOR is an ideal tool for putting together the jigsaw presented by these individual domains. However, it relies on the structures of individual domains presenting an accurate representation of the domain in the full-length protein's structure. The crystal structure of approximately half the MuRF 1 coiled coil domain has been solved as a tetramer (Franke et al., 2014) which deviates from canonical full length Trim coiled coil domain structures. This canonical structure features an anti-parallel coiled coil dimerization domain, with any additional C-terminal domains folded back into the centre of the coiled coil forming a 4-helix bundle (Goldstone et al., 2014; Li et al., 2014; Sanchez et al., 2014; Weinert et al., 2015).

5.1.4 The Biological Function of MuRF 1

Muscle mass is a result of a balance between expression (hypertrophy) and degradation (atrophy) of proteins within the sarcomere controlled by a series of interlinked signalling pathways (Glass, 2005; Tawa et al., 1997). Hypertrophy is controlled by the mechanistic target of rapamycin (mTOR) pathway, and muscle atrophy is regulated by the expression levels of E3 ubiquitin ligases MuRF 1 and MAFbx (also known as Atrogin-1) (Bodine and Baehr, 2014; Bodine et al., 2001; Koyama et al., 2008). Factors affecting the regulation of MuRF 1 and MAFbx have been studied in depth, particularly those related to muscle degradation under a variety of different conditions such as ageing (sarcopenia), cancer (cachexia),

chronic kidney disease, diabetes, and chronic obstructive pulmonary disease (Bodine and Baehr, 2014; Gumucio and Mendias, 2013). MuRF 1 expression is promoted by Forkhead box protein O (FOXO) (Milan et al., 2015; Waddell et al., 2008), nuclear factor κB (NF-κB) and the p38 mitogen activated protein kinase (p38MAPK) promoters (Adams et al., 2008). Promotion of MuRF 1 and MAFbx expression by NF-κB and p38MAPK is induced by two main signalling pathways that are activated by the presence of inflammatory cytokines, glucocorticoids, or factors related to oxidative stress. Within these pathways, activation of NF-κB and p38MAPK are controlled by a series of kinases, p38MAPK is phosphorylated by MAPK kinase kinase (MKK) and the IKKβ/IKKα complex phosphorylates NF-κB, leading to trans location of NF-κB and p38MAPK into the nucleus (Kandarian and Jackman, 2006).

5.1.5 Targets of MuRF 1

Upon expression MuRF 1 localises to the M-band of the sarcomere, with a limited amount of MuRF 1 observed close to the Z-disk region. Its binding partners include heavy chain myosin (HCM), light chain myosin (LCM), troponin, and Titin (Mrosek et al., 2007; Witt et al., 2005). MuRF 1 marks proteins for degradation by the 26S proteasome using K48 or K63 linked polyubiquitin.

Ubiquitination is controlled by three categories of enzymes. Firstly ubiquitin is activated in an ATP dependent manner by E1 ubiquitin ligases. Secondly the E1 enzymes transfer ubiquitin to the catalytic cysteine residue in E2 enzymes. Finally E3 ligases target the E2 activated ubiquitin ligases to their substrates (Pickart, 2001).

E3 ubiquitin ligases can be split into two families. Those homologous to the E6-AP carboxyl terminus (HECT) ligases chaperone E2 ubiquitin ligases to the target for ubiquitination and aid in catalysis of the ubiquitin transfer. While RING ligases direct E2 enzymes to their targets without taking part in catalysis (Pickart, 2001).

MuRF 1 is a RING E3 ubiquitin ligase; consequently the ubiquitin ligase activity is dependent on which E2 ligase binds MuRF 1. Interaction with UBcH13/Uev1a results in K63 linked substrates and MuRF 1 interacting with UbcH1 produces K48 linked substrates (Marblestone et al., 2013). MuRF 1 acts as an E3 ubiquitin ligase for both heavy and light chained myosin at hitherto unknown sites. Understanding the structure of MuRF 1 would allow a clearer picture of the proteins structural-functional relationship to be achieved.

5.1.6 The MuRF 1 Crystal Structure

A crystal structure for a fragment of the MuRF 1 coiled coil domain has been determined, showing an α-helical tetramer (Franke et al., 2014). Within the same study size exclusion chromatography-multiple angle light scattering (SEC-MALS) data revealed MuRF 1 was present as a dimer in solution. The crystal structure presented 6 possible conformations for the MuRF 1 dimer. The aim of this study was to determine which, if any, of the MuRF 1 conformations observed in the crystal structure were present in the glass phase. In this study a construct containing the MuRF 1 coiled coil and COS-Box domain (MuRF 1cc) was examined using distance distributions from PELDOR data to determine whether the dimerized coiled coil domain was parallel or antiparallel.

In addition, the location of the C terminal COS-Box domain in relation to the coiled coil was investigated to determine if the COS-Box adopted a similar fold seen in other coiled coil domain structures of Trim family member proteins.

5.2 PELDOR

5.2.1 PELDOR Data

Distances from PELDOR data were determined for a series of different R1 binding sites on the coiled coil and COS-box domains of MuRF 1cc. Raw PELDOR data for E200R1, K212R1, and R230R1 on the MuRF 1 coiled coil domain, as well as E313R1 and R320R1 on the COS-Box domain, contained two or more oscillations allowing a distance distribution to be measured from PELDOR data. In addition, the single oscillation visible in the raw PELDOR data for MuRF 1cc E192R1 allowed a modal distance to be measured at this site (appendix figure S5.1). E243R1 and Q247R1 on the coiled coil domain as well as K297R1 on the COS-Box gave oscillation free data. However, the maximum time from the raw PELDOR data at these sites indicated the maximum distance that could be visible, provided that oscillations within the PELDOR data had not decayed.

5.2.2 The Coiled Coil of MuRF 1 is Anti-Parallel

Modal distances for R1 bound to the coiled coil domain of MuRF 1cc varied more between sites than distance variations expected from a parallel coiled coil conformation (appendix figure S5.2). PELDOR data gave progressively shorter modal distances as the labelling site was moved from the N-terminus of the MuRF 1cc coiled coil domain to MuRF 1cc K212R1. In addition, progressively longer modal distances were observed as the labelling site was moved from MuRF 1cc E222R1 towards the C-terminus of the MuRF 1cc coiled coil domain. This pattern

of changes in the modal distance as labelling sites were moved from the N-terminus to the C-terminus of the MuRF 1cc coiled coil domain, is indicative of an antiparallel homodimer. Labelling sites within the COS-Box domain showed shortening of modal distances as the labelled position was moved from the N-terminus towards the C-terminus (appendix figure S5.1), implying the beginning of an antiparallel homodimer.

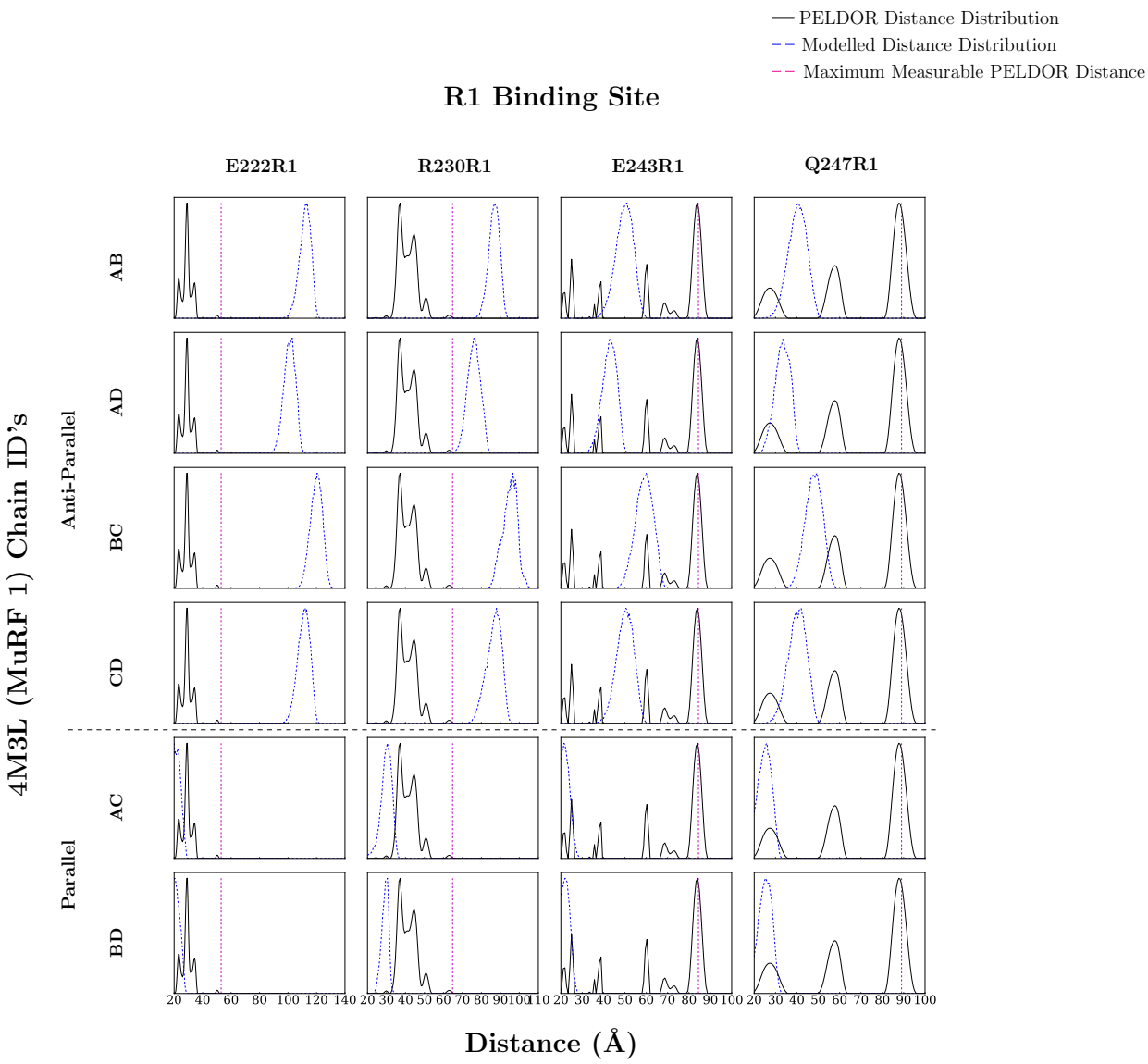

Figure 5.2: Distance distributions of R1 bound to MuRF 1, the solid black line represents the distance distribution determined by PELDOR and the blue dashed line represents distance distributions determined using MTSL Wizard (Hagelueken et al., 2012) on the MuRF 1 crystal structure (PDB ID: 4M3L). The magenta dashed line is the maximum distance that could be measured from a single oscillation spanning the PELDOR time window, with all distributions normalised to give their highest peak an intensity of 1.0. Experimental and model distances were compared for each dimer conformation within the crystal structure, with different conformations labelled by the chains they were composed of (AB, AC, AD, BC, BD and CD).

5.2.3 Distance Distributions from PELDOR Against Those Modelled onto the Crystal Structure

Distance distributions from PELDOR data of MuRF 1cc E222R1, R230R1, E243R1, and Q247R1, were compared to distance distributions from R1 modelled onto the MuRF 1 crystal structure (PDB ID: 4M3L) using MTSL Wizard. Modelled distance distributions were measured between homologous spin label pairs from the six different homodimers within the tetramer observed in the MuRF 1 crystal structure (figure 5.1, A). To determine which, if any, dimer present in the crystal structure fit the PELDOR data, these modelled distance distributions were compared to their experimental counterparts (figure 5.2). This comparison showed that short experimental distance distributions for MuRF 1cc E222R1 and R230R1, were not present in the modelled structure's antiparallel conformations. Additionally, short distances from parallel conformations of the crystal structure were not present in the MuRF 1cc R230R1, E243R1, or Q247R1 experimental distance distributions. These discrepancies indicated none of the dimeric conformations present in the crystal structure matched the conformation within the glass phase structure.

5.3 Homology Model

5.3.1 Crystal Structures of Trim Proteins Coiled Coil Region

Crystal structures for the coiled coil regions of rhesus Trim 5α (PDB ID: 4TN3), Trim 20 (PDB ID: 4CG4), Trim 69 (PDB ID: 4NQJ) and two for Trim 25 (PDB IDs: 4LTB and 4CFG) have been deposited in the protein data bank. These all demonstrated an antiparallel-coiled coil structure that broke into a four-helix bundle in the centre, due to the presence of C-terminal α-helical domains. This structure would produce a similar pattern of distance distributions to the pattern

observed from the MuRF 1cc PELDOR data. To investigate how accurately the other Trim coiled coil domain structures represented MuRF 1cc, homology models of MuRF 1cc were made with modeller (Webb and Sali, 2002) based upon the various Trim coiled coil domain structures. R1 was modelled at the different labelling sites on each homology model using MTSL Wizard (Hagelueken et al., 2012) to produce a modelled distance distribution.

5.3.2 Comparison of Distances from PELDOR Against Modelled Distance Distributions for the Coiled Coil Region (H1)

Modelled distance distributions from the homology models coiled coil domains (H1) were compared to distance distributions from the PELDOR data for MuRF 1cc (figure 5.3 and 5.4). The range of distance distributions from the modelled and experimental data was comparable for all sites where oscillations could be gathered (E192R1, E200R1, K212R1, E222R1, and R230R1). Oscillation free PELDOR data for MuRF 1cc E243R1 and MuRF 1cc Q247R1 gave a minimum modal distance that could be present within the glass phase structure of MuRF 1cc. These minimum distances were based upon the maximum distance that could be determined using a single oscillation with a wavelength of the maximum time from PELDOR data at these sites.

5.3.3 Differences Between PELDOR Distance Distributions and the Homology Model for H1

There were slight differences within modal distances for R1 bound to the coiled coil region of the MuRF 1cc construct when comparing experimental and modelled distance distributions. However, key differences lay in the multimodal distance distribution from PELDOR data, compared to monomodal modelled distance distributions at equivalent sites (figure 5.3, positions between residues 200 and

230). MTSL Wizard models R1 onto a protein structure with immobile amino acid side chains. This is corrected for by allowing a specific number of clashes in the model. Split peaks caused by surrounding amino acids adopting positions that prevent specific conformations of R1 within the MuRF 1 structure are not modelled sufficiently by MTSL Wizard. Additionally, differences in distance distributions from PELDOR data and modelled distance distributions could be caused by different positions of the COS-Box domain (H3) between the glass phase structure and homology models.

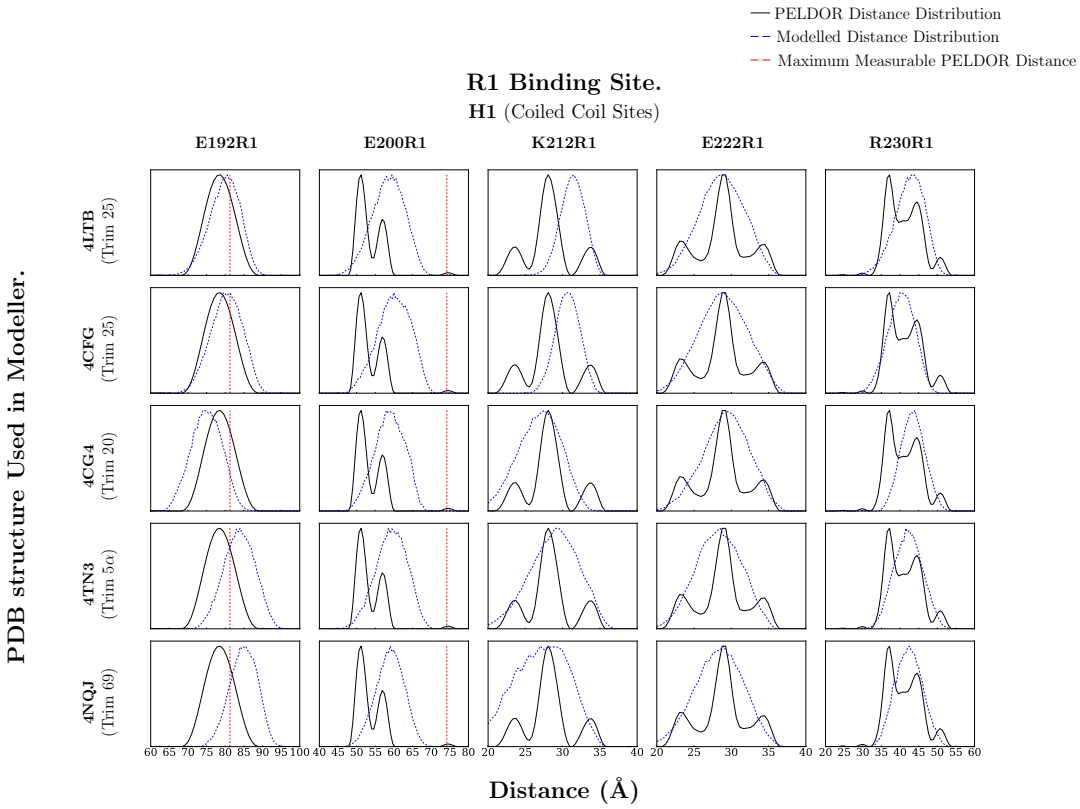

Figure 5.3: Distance distributions for the N terminal and central R1 binding site on the coiled coil domain of MuRF 1, the solid black line represents the distance distribution determined by PELDOR and the blue dashed line represents distance distributions determined using MTSL Wizard (Hagelueken et al., 2012) on homology models of MuRF 1 to various Trim protein coiled coil domain structural templates (labelled on the left). The magenta dashed line is the maximum distance that could be measured from a single oscillation spanning the PELDOR time window, and distributions were normalised to give their highest peak an intensity of 1.0.

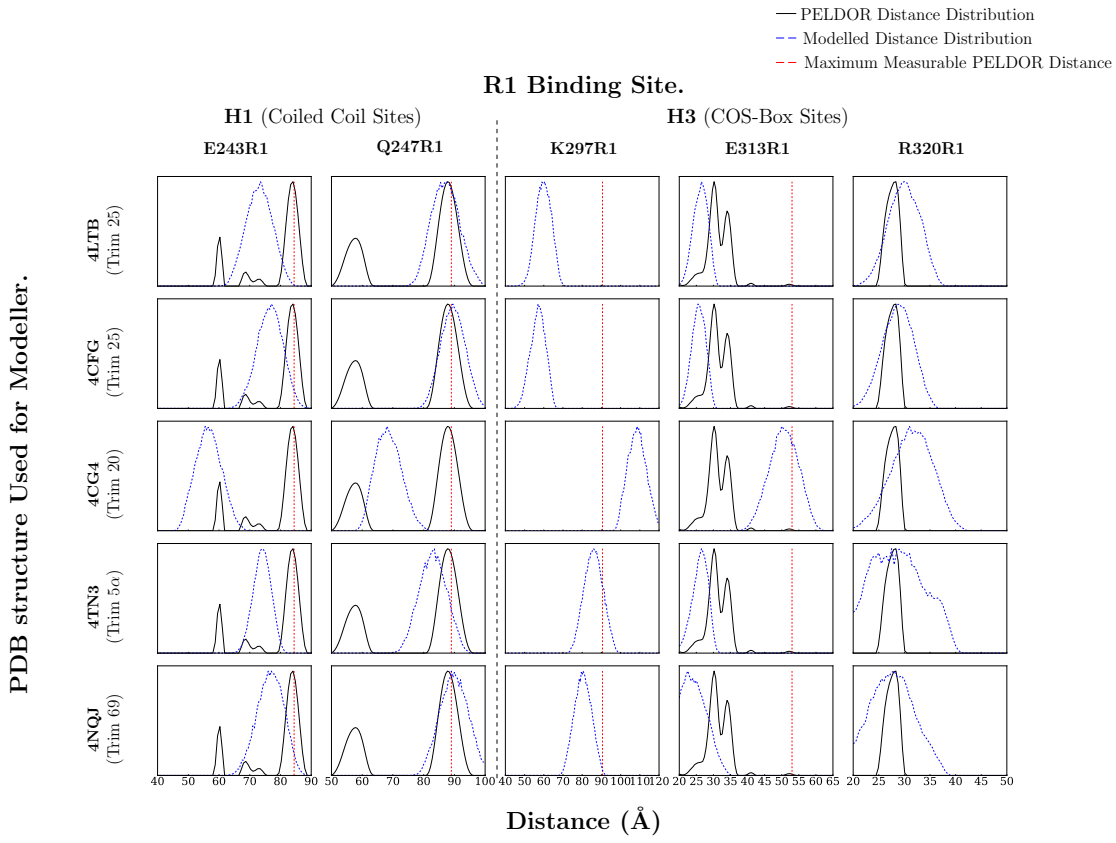

Figure 5.4: Distance distributions for the C terminal coiled coil domain and COS-Box R1 binding sites on MuRF 1cc, the solid black line represents the distance distribution determined by PELDOR and the blue dashed line represents distance distributions determined using MTSL Wizard (Hagelueken et al., 2012) on homology models of MuRF 1 to various Trim protein coiled coil domain structural templates (labelled on the left). The magenta dashed line is the maximum distance that could be measured from a single oscillation spanning the PELDOR time window, and distributions were normalised to give their highest peak an intensity of 1.0.

5.3.4 Comparison of PELDOR data against the homology model for H3

The COS-Box domain was positioned differently in the glass phase structure for MuRF 1cc when compared to the homology models. Evidence for this was differences between distance distributions from the modelled structure and PELDOR data for MuRF 1cc E313R1 and MuRF 1cc K297R1. However, similarities between the modelled and experimental distance distributions were observed for MuRF 1cc R320R1.

Plotting the modal distance against sequence position (figure 5.5, B) showed a shortening then lengthening of distances within the coiled coil domain as the residue number progressed. This pattern would be expected in an antiparallel homodimer. The COS-Box domain had a similar shortening of distances, with E313R1 giving the shortest distance in all modelled structures except for the homology model based upon 4CG4. The position of the shortest modal distance implied crossing of the modelled COS-Box domains close to E313R1. PELDOR data showed modal distances from the COS-Box domain decreased up to at least R320R1, suggesting crossing of COS-Box domains from opposite sides of the homodimer was located beyond this point.

A.

R1 Binding Site	PELDOR Modal Distance	4LTB Modal Distance	4CFG Modal Distance	4CG4 Modal Distance	4TN3 Modal Distance	4NQJ Modal Distance
192	78.7	80.5	79.5	79.0	84.0	85.5
200	51.2	59.5	60.0	58.0	58.5	59.0
212	28.1	31.5	30.5	30.0	29.5	27.0
222	29.2	29.0	29.0	30.0	28.5	29.0
230	37.2	43.0	40.0	44.0	41.5	42.5
243	84.1	73.5	77.0	55.5	74.0	77.0
247	87.8	87.5	89.5	71.0	83.5	89.0
297	86.3	60.5	57.0	110.0	86.0	80.5
313	30.2	26.5	25.5	50.0	26.5	22.5
320	28.3	30.0	29.0	34.0	27.5	28.0

B.

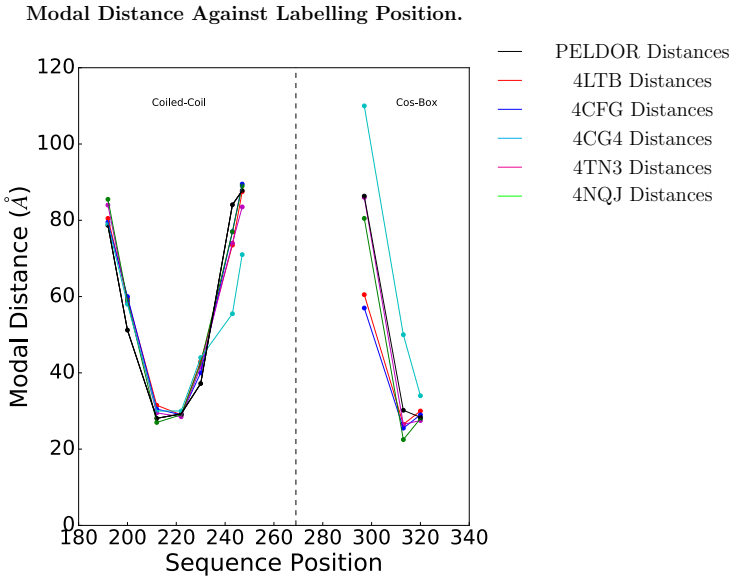

Figure 5.5: (A) A table of the different modal distances from the PELDOR data along with the respective modal distances from R1 modelled at various labelling sites on the threaded protein model. (B) A scatter plot of the modal distances from PELDOR and the threaded structures against labelling position.

5.4 CW-EPR

5.4.1 Differences in CW-EPR Spectra Between Sites

CW-EPR spectra was recorded for the different R1 binding sites on MuRF 1cc. Comparisons of these spectra showed different mobilities of R1 between labelling

sites (figure 5.6). Labelling sites could therefore be grouped based upon the different central line widths from the CW-EPR spectra. Narrow central line widths were thought to be representative of solvent exposed sites, and broader central line widths were thought to be representative of sites with their motion restricted by protein structural features. A scatterplot of the different central line widths against the R1 binding position allowed sites to be split into regions with line widths greater than or less than 3 G (figure 5.6, B).

5.4.2 Explanation of the difference in central line widths

Except for a limited amount of unbound R1 present in some spectra (shown by the presence of sharp, low intensity spectral lines), CW-EPR spectra from R1 bound to MuRF 1cc had a line shape typical of R1 bound to stable protein structural features. Broadening of the central line width was observed at some sites showing restrictions in labels motion. Within MuRF 1cc the most likely restriction to the spin label's mobility was the location of the COS-Box domain.

Sites on both the coiled coil (H1) and COS-Box (H3) domains located in or near the coiled coil / Cos-Box binding interface of the homology model gave CW-EPR central line widths greater than 3 G. Labelling sites away from this binding interface had central line widths less than 3 G. The exception to this observation was E243R1, which showed a central line width greater than 3 G, while the binding site was modelled on the opposite face of the coiled coil domain to the COS-Box binding interface. PELDOR data for MuRF 1cc E243R1 did not contain noticeable oscillations that corresponded to distances in the range of the model structure. This indicated that the homology models presented false positions of E243R1, with

distances across the homodimer shorter than the minimum possible distance in the glass phase MuRF 1cc structure.

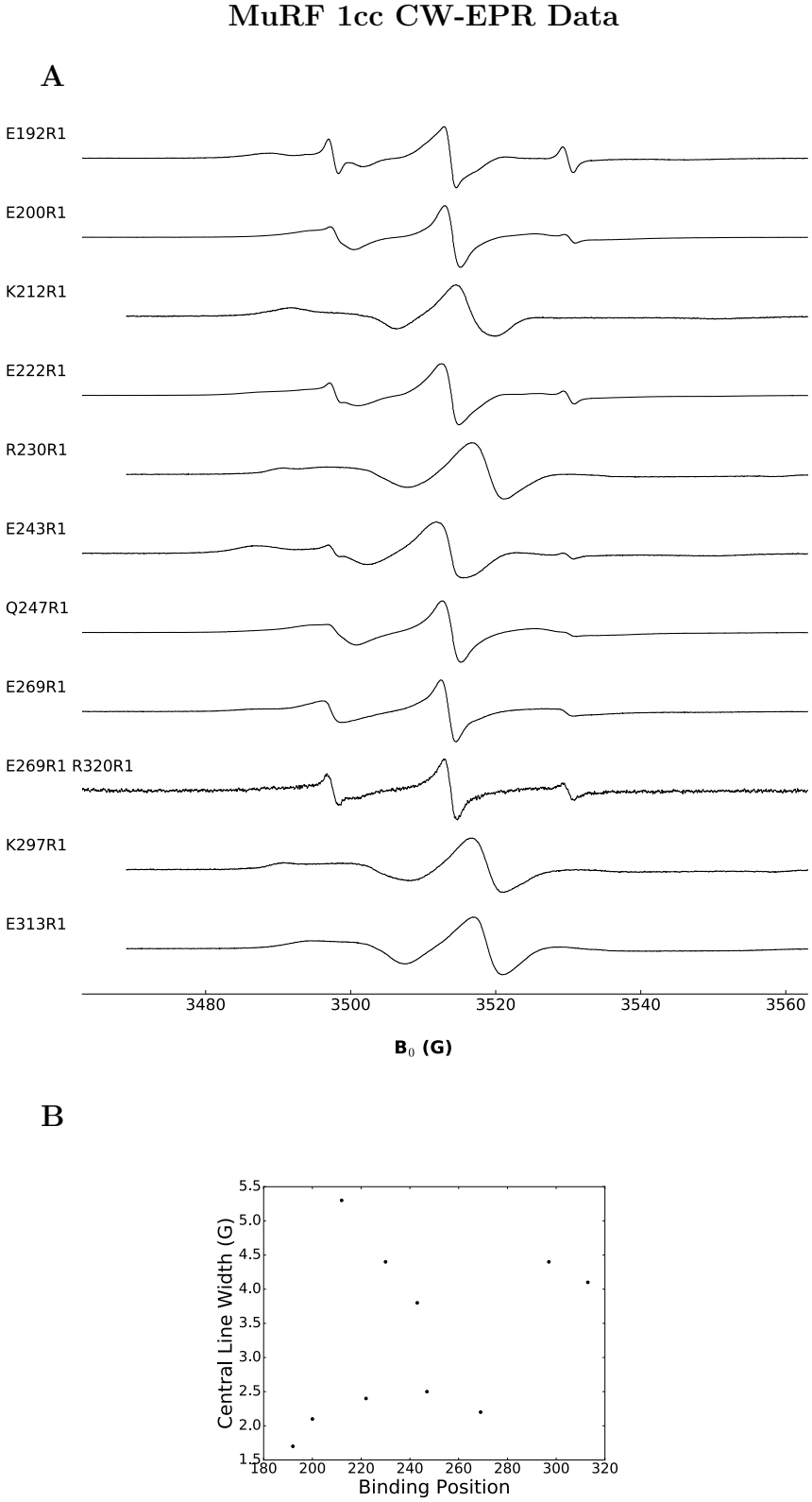

Figure 5.6: (A) CW-EPR spectra for all MuRF 1cc R1 binding positions, the central peak was normalised to an intensity of 1.0 and individual spectra were plotted on the same axis set. (B) A scatterplot of the CW-EPR central line width against R1 binding position.

5.5 The MuRF 1 coiled coil Domain Conformation

5.5.1 Implications of the Parallel or Anti-Parallel Coiled Coil Region

The coiled coil domain of MuRF 1 being in a parallel or antiparallel conformation has drastic implications on the location of functional domains within the protein structure. A parallel coiled coil conformation suggests the RING finger and COS-Box domains of the MuRF 1 homodimer are at opposite ends of the coiled coil domain. While an anti-parallel conformation positions the RING figure domains at opposite ends of the coiled coil domain within the MuRF 1 homodimer. PELDOR data showed conclusively that the coiled coil domain of MuRF 1cc adopted an antiparallel conformation, due to large variations in distances across the homodimer for different R1 labelling sites.

5.5.2 Differences Between the Crystal Structure and Homology Model for the Coiled Coil Domain of MuRF 1:

The MuRF 1 coiled coil domain crystal structure (PDB ID: 4M3L) was determined using the C-terminal half of the MuRF 1 coiled coil domain. Because the MuRF 1 coiled coil domain adopted an antiparallel conformation, the opposing N-terminal half of the MuRF 1 coiled coil, required for dimerization, was missing in crystallisation trials. As a result, it was impossible for the structure of the MuRF 1cc homodimer to be present within the MuRF 1 crystal structure. The antiparallel conformation of the MuRF 1 coiled coil domain possessed similarities to crystal structures of coiled coil domains from other Trim proteins. To further investigate these similarities, homology models of MuRF 1 based upon crystal structures of various Trim protein coiled coil domains were made. These homology models were interrogated by comparing distance distributions from R1 modelled onto the

different homology models using MTSL wizard, to distance distributions from PELDOR data.

5.5.3 Homology Model Distance Distributions

Distance distributions from the MuRF 1cc homology models were within the same range as distance distributions from PELDOR data for the majority of R1 labelling sites. Differences between the modelled and the glass phase structures are localised to either a splitting of the experimental distance distributions into two or more peaks, or experimental distance distributions being located at longer ranges than modelled distance distributions. Splitting of the distance distribution from PELDOR data occurred due to the presence of structural features restricting the label's nitroxide distribution. In the case of MuRF 1 the most likely structural feature causing this restriction was the presence of the COS-Box domain. The shift in the modal distance for MuRF 1cc E243R1 between the homology models and glass phase structure, was likely a result of the coiled coil domains in the homology models having different bending or coiling to the coiled coil domain of the glass phase structure.

5.5.4 CW-EPR reveals Possible Residues in the COS-Box Binding Interface

In addition to causing split distance distributions from the PELDOR data the presence of the COS-Box domain would restrict the motion of R1, causing the CW-EPR spectra to broaden. This was hypothesised to create line widths greater than 3 G for sites located close to the COS-Box/coiled coil domain binding interface. The majority of R1 labelling sites on the coiled coil domain of the homology models adhered to this rule, with the exception of MuRF 1cc E243R1. In MuRF 1cc E243R1

the labelling site was positioned away from the COS-Box binding interface in homology models, while the central line width from the CW-EPR spectrum was greater than 3 G. Combining this observation with the greater modal distance from PELDOR data at this site, suggested the coiling in the glass phase MuRF 1cc structure was different to the coiling of the homology model, moving E243 towards the coiled coil domain's COS-Box binding interface.

5.5.5 The COS-Box Domain

The COS-Box domain was modelled using the C-terminal α-helix from the various Trim protein's crystal structures. None of the Trim crystal structures possessed a COS-Box domain themselves, as such the domains which the homology models were based on were rough approximations of the COS-Box domain's position. This is seen in the more pronounced deviations in PELDOR distance distributions from the modelled distance distributions within the Cos-Box domain of MuRF 1. MuRF 1cc K297R1 was at a distance that should be present in the PELDOR data according to the homology models. However, no distance distribution was observed from the PELDOR data. Similarly, MuRF 1cc E313R1 had a shorter modelled distance distribution than the distance distribution from PELDOR data, supporting a shift of the COS-Box domain in the direction of its N-terminus within the glass phase structure. Modal distances between the PELDOR and modelled data for MuRF 1cc R320R1 were similar. This suggested the shift in the COS-Box domain required for the other COS-Box labelling sites positioned R320 across from its counterpart on the opposing strand of the homodimer within the homology model.

5.5.6 The COS-Box Domain Structure

An NMR structure of the COS-Box domain from MID1 has been resolved (PDB ID: 5IM8, (Wright et al., 2016)) that showed a lengthened linker helix between the coiled coil and C-terminal α-helix (H2) when compared to the various homology models. This lengthening of the helix would effectively shorten the linker between H2 and H3 within the COS-Box domain, pulling H3 towards the C-terminus of the coiled coil region. This shift in the central H3 helices would cause distances measured within the COS-Box to lengthen, conforming to the observed greater length of distances for E313R1 and K297R1 from the PELDOR data when compared to modelled distances.

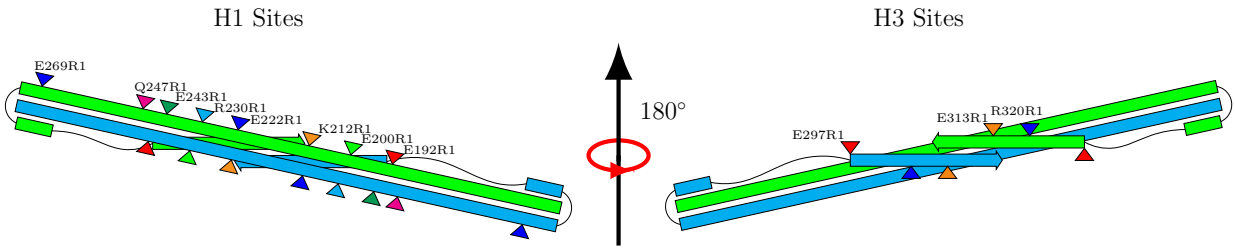

Figure 5.7: Cartoons of the proposed MuRF 1cc structure, with positions of the H1 and H3 labelling sites marked by triangles.

5.6 Structural Implications for MuRF 1 Binding to Titin

From the range of sarcomeric structural proteins MuRF 1 binds to its best-characterised interaction is with Titin. Previous studies have shown the coiled coil domain of MuRF 1 interacts with a subsection of Titin comprising of the

immunoglobulin (Ig) A168, Ig A169, fibrinectin (Fn) A170 and Titin kinase (TK) domains (A168-TK) (Witt et al., 2005)(Centner et al., 2001)(Mrosek et al., 2007), a region close to the M-line of the sarcomere. There is currently no definitive information on the stoichiometry of MuRF 1/Titin interactions. This is due to the higher order oligomers formed by B-Box interactions between full-length MuRF 1 structures. This study has shown the MuRF 1 coiled coil domain forms an elongated anti-parallel dimer. When the proposed homology models were compared to the hypothesised A168-A170 binding groove in Titin, it was apparent this binding interaction would leave approximately half of the homology model exposed.

The location of the Titin binding region within MuRF 1 has been previously observed using a series of MuRF 1 fragments. These observations showed a prevalence of Titin binding between residues 87 to 100 within the B-Box / RING domains, 164 to 176 and 242 to 254 within the coiled coil domain, and 296 to 325 on the COS-Box domain. The limitation of this fragment screen is it does not allow the observation of Titin/MuRF 1 binding over a large region. The proposed anti-parallel coiled coil structure presented here places the binding regions on separate sides of the MuRF 1 coiled coil domain. The symmetry of the Titin binding sites upon the coiled coil/COS-Box domains in the MuRF 1 homology model make it possible for a MuRF 1 dimer to bind two Titin monomers on either end of the coiled coil, or a Titin A168-A170 monomer to bind the central region of the MuRF 1 dimer.

5.6 Conclusion and Prospects

The evidence presented here does not produce a definitive structure of the coiled coil and COS-Box domains from MuRF 1. However, it asserts the coiled coil domain of MuRF 1cc was anti-parallel, giving a similar structure to the coiled coil domain from crystal structures of other Trim family members. The evidence presented here also supported the COS-Box domain folding back towards the centre of the MuRF 1 coiled coil domain, again a similar structural feature that was observed in other Trim family coiled coil crystal structures. This conformation places the B-Box and RING domains of MuRF 1 at the extremities of the coiled coil, and the C-terminal COS-Box domain towards the centre. These domain positions provide valuable information on determining the structural and functional relationship for the ubiquitination of sarcomeric proteins by MuRF 1.

The results from this study could be expanded upon using further PELDOR measurements, allowing a more refined model of the MuRF 1 coiled coil domain to be determined. Additionally, the use of the same labelling sites on a full length MuRF 1 construct would clearly show whether MuRF 1cc was representative of the coiled coil domain conformation within full length MuRF 1. Finally, a more refined MuRF 1cc structure would enable the structure of a MuRF 1cc/Titin A168-Tk complex to be determined, providing valuable structural insights on how MuRF 1 functions within the sarcomere.

Chapter 6: Using Protein Duteration to Measure Spin Label Distances greater than 100 Å within the Coiled Coil Region of Trim 25.

6.0 Summary

A major limiting factor when using PELDOR for determining distances within protein structures is dephasing of electron spins. The major cause of dephasing within protein structures are dipolar interactions between the unpaired electron and surrounding protons. This form of dephasing can be reduced by replacing hydrogen atoms within the sample with deuterium, which has a weaker dipolar coupling to the unpaired electron.

Within this study, it was investigated whether replacing protons within a protein sample with deuterium caused dipolar interactions, and therefore the distance, between unpaired electrons to become a prominent factor in dephasing. To do this a distance ladder was produced by labelling deuterated constructs of the elongated coiled coil domain from tripartite motif protein 25 (Trim 25) with MTSL. Distance distributions and the T_m for each construct were measured to identify any relationship between spin label distance and T_m. A correlation was not found between the spin label distance and T_m. Although, a significant difference was observed between distance distributions from PELDOR data, and distance distributions from R1 modelled onto both Trim 25 crystal structures from the protein data bank (PDB). This implied a difference in the coiling of the coiled coil domain within Trim 25 in solution compared to the coiling observed in the crystal structures.

6.1 Introduction

6.1.1 PELDOR's Spin Echo Modulation

The quality of PELDOR data is dependent upon the observer pulse echo's intensity, as well as the magnitude and persistence of the echo's modulation throughout the experimental time period. Measuring the echo modulation against the timing of the pump pulse (τ) results in an oscillation, which can be fit to produce a distance distribution between unpaired electrons (Jeschke, 2002; Jeschke et al., 2006). The decay of this oscillation results from the distribution of unpaired electrons within the sample, narrower distributions increase the persistence of the oscillation and broader distributions increase oscillation dampening. The modulation depth in a two electron spin system is dependent upon the proportion of electrons excited by the observer pulse that couple to electrons excited by the pump pulse. A higher proportion of coupling electrons results in an increased modulation depth (Giannoulis et al., 2013).

EPR within protein structures is most often performed using SDSL. For SDSL, the persistence of oscillations within PELDOR data is dependent upon the spin label's distribution (Margraf et al., 2007). To produce more persistent oscillations a series of rigid spin labels have been developed, increasing the resolution of the distance distribution from PELDOR data (Cunningham et al., 2015; Fleissner et al., 2011; Hubbell et al., 2013; Toniolo et al., 1998). The modulation depth when using SDSL depends on both the labelling efficiency and the absorption spectra of the unpaired electron (Giannoulis et al., 2017). More commonly used spin labels such as R1 give a high labelling efficiency and an absorption spectra broad enough to accommodate two microwave pulses (DeSensi et al., 2008; Guo et al., 2008). In the

nitroxide spectra from R1, rectangular microwave pulses are able to cover a significant proportion of the spectra, allowing dipolar interactions to be measured between a significant proportion of unpaired electrons within the sample (Kirilina et al., 2005). The development of arbitrary waveform generators (AWGs) for microwave pulses, has enabled the use of non-rectangular and adiabatic pulses to increase the proportion of the electron spectra that can be excited, increasing spin echo intensity and modulation depth (Doll et al., 2013).

6.1.2 PELDOR's Spin Echo Intensity

The spin echo intensity determines the time it takes to produce a PELDOR spectra with a high signal to noise ratio (S/N). Higher echo intensities require fewer averages to give a reasonable S/N (Breitgoff et al., 2017; Ghimire et al., 2009; Ward et al., 2010). The decay in echo intensity over time has a great effect upon the signal intensity measured in PELDOR experiments. Lower rates of echo decay allow experiments to be run over longer time periods with little reduction in S/N (El Mkami et al., 2014).

Lengthening experimental time periods allows the measurement of oscillations with higher wavelengths or a greater number of lower wavelength oscillations. This increases the range of measurable distances and distance distributions (El Mkami et al., 2014; Schmidt et al., 2016). The echo decay is governed by the transverse relaxation time (T_2). T_2 approximates to the phase memory time (T_m) within samples where the longitudinal relaxation time (T_1) is an order of magnitude higher than T_2. This is the case for nitroxide radicals under commonly use experimental conditions in PELDOR. T_m is the time it takes for the electron spins to dephase until the net magnetization in the transverse plane is at 37 % of

its original value (Zecevic et al., 1998). In PELDOR this dephasing is caused by non-recoverable spin-spin coupling between electrons under the observer pulse and the surrounding magnetic environment (Ward et al., 2010).

The limiting factor to T_m values within protein samples is the abundance of protons, which is often reduced by running the sample in a deuterated solvent (Zecevic et al., 1998). Further increases to the T_m for protein samples has been achieved by developing pulse sequences that increase the amount of recoverable dephasing (Doll et al., 2013; Motion et al., 2016), as well as deuterating the underlying protein structure to decrease dephasing to the local magnetic environment (Ward et al., 2010).

6.1.3 T_m and the Distance Between Unpaired Electrons

It is commonly stated that the maximum measurable distance by PELDOR is 80 Å within a protein sample. This value is based upon the maximum experimental time period of 10 μs when using 4-pulse PELDOR on a protonated protein in a deuterated solvent (Jeschke, 2002). Deuteration of the protein backbone (Ward et al., 2010) as well as enhanced pulse sequences (Doll et al., 2013; Motion et al., 2016), have proven this to be a gross underestimate of the distance range available from PELDOR. Determining the maximum distance measurable within a protein sample is valuable information for those wishing to apply EPR as a tool for structural biology. In addition understanding the less dominant but significant pathways of spin-spin relaxation within protein structures would direct further enhancement of the technique.

Deuteration of the underlying protein structure makes it possible to study the effect of these weaker but significant spin-spin interactions upon T_m (El Mkami et al., 2014). One noticeable factor is the effect of electron spin-spin distance upon T_m, with a reduction in T_m observed for systems where electron spins are closer together (Wyk et al., 1997). The aim of this study was to investigate what effects the distance between spin labels within a deuterated protein have on the T_m of the sample.

6.1.4 The Retinoic Acid Inducible Gene 1 (RIG1) Pathway

The Trim family member used in this study was Trim 25, which functions in the oestrogen response system, cell proliferation, and the innate immune response system (Sanchez et al., 2016). Out of these different functions, the interaction between Trim 25 and RIG 1 in the innate immune response system has been best characterised (Gack et al., 2007; Kawai and Akira, 2008).

RIG 1 is activated by its helicase domains binding viral RNA; this induces a structural change that exposes the two caspase recruitment domains (2CARD). The PRY-SPRY domain of Trim 25 binds to the 2CARD domains of RIG 1, inducing polyubiquitination of the 2CARD domains using K63 linked ubiquitin chains (Davis and Gack, 2015; Gack et al., 2007). Ubiquitination of the RIG1 2CARD domains cause the formation of a stable 2CARD tetramer, which interacts with the CARD domain of the mitochondrial protein MAVS (also known as CARDIF, VISA, or ISF-I) in a “lock washer” conformation. This interaction sets up a signalling cascade to generate the type 1 interferon response (Altenbach et al., 1989; Castanier et al., 2012; Perry et al., 2005; Seth et al., 2006).

It has been found the Trim 25 RING domain is only active as a dimer. Crystal structures of the Trim 25 homodimer coiled coil region indicate the two RING domains are located on opposite ends of its ~170 Å long coiled coil. This leads to the hypothesis that Trim 25 activates the RIG1 pathway in higher oligomeric states (Sanchez et al., 2014).

6.1.5 Influenza A Viral (IAV) repression of Trim 25

To proliferate viruses have developed a series of techniques for repressing the innate immune response system. The repression of RIG1 like receptors (RLR) signalling pathways involves the production of constructs that shield the 5'ppp viral RNA, bind directly to RIG1, or act as an antagonist for other signalling molecules in the pathway (Yoo et al., 2014). The non-structurally binding protein 1 (NS1) of IAV targets a multitude of host proteins within the innate immune system, including specific species of Trim 25 (Rajsbaum et al., 2012). Human Trim 25 binds a wide range of IAV NS1 isomers, whereas mouse Trim 25 has been observed not to bind NS1 from any IAV species tested (Gack et al., 2009; Rajsbaum et al., 2012).

Binding of Trim 25 to NS1 suppresses the ubiquitination of RIG1 within human cells. Conversely, inhibition of RIG1 ubiquitination in mice occurs by NS1 binding Riplet, a Trim like protein (Oshiumi et al., 2010). Binding and ubiquitination of RIG1 is carried out by the PRY-SPRY and RING domains of Trim 25 respectively. NS1 suppresses Trim 25 activity by binding to the coiled coil scaffolding domain, suggesting signalling by Trim 25 is repressed by a structural change to the coiled coil domain caused by binding NS1 (Gack et al., 2009).

6.1.6 Trim 25 domains

Crystal structures for the RING (Sanchez et al., 2016), coiled coil (Sanchez et al., 2014) and PRY-SPRY (D'Cruz et al., 2013) domains of Trim 25 have been determined previously. However, there has been no structure determined for the full-length protein. The Trim 25 coiled coil dimerization domain (Trim 25cc) provides the most convenient structure for producing a ladder of distances, owing to its length of ~170 Å observed in both crystal structures present in the PDB (PDB IDs: 4CFG and 4LTB)(Sanchez et al., 2014). This enabled the measurement of an extensive range of distances using PELDOR, allowing distant dependent variations in T_m to be observed.

For this study, a series of different R1 sites were introduced onto the Trim 25cc domain, producing distances between 36 Å and ~120 Å across the coiled coil homodimer. R1 sites were modelled onto both Trim 25cc crystal structures deposited in the PDB using MTSL Wizard, and modelled distance distributions between identical labelling sites across the homodimer were measured. Comparisons between modelled distance distributions and experimental distance distributions acquired using PELDOR, were used to evaluate how closely the Trim 25cc crystal structures reflected the glass phase structure. Additionally, T_m measurements were compared to the modal distances from PELDOR data for each labelling site, or against the modelled modal distances for cases where PELDOR data could not be run over a great enough time period to measure one full oscillation.

6.2 PELDOR

6.2.1 PELDOR Measurements

A ladder of distances from different R1 binding positions was measured on deuterated Trim 25cc constructs using PELDOR (figure 6.1, for full data see figure S6.1). Deuteration allowed PELDOR data to be acquired over time periods up to 60 μs, allowing the measurement of distances up to and including 124 Å. To produce experimental distance distributions, PELDOR data was acquired over long enough time periods to give 2 full oscillations where possible, and a single oscillation where not (i.e. Trim 25cc E293R1). R1 was modelled onto the Trim 25cc crystal structures (PDB IDs: 4CFG and 4LTB) using MTSL Wizard, and model distance distributions were measured between the modelled R1 nitroxide nitrogens.

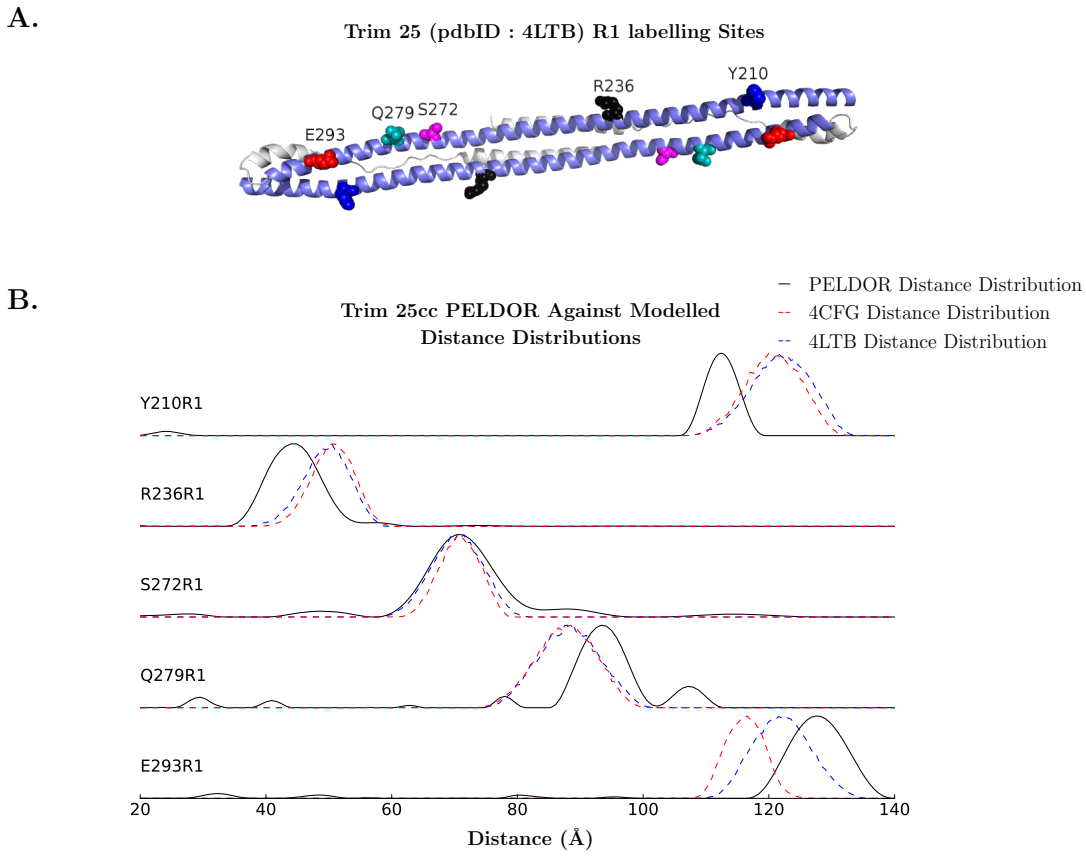

Figure 6.1: (A) The Trim 25cc crystal structure showing the protein backbone as a cartoon and different labelling positions as spheres. (B) Distance distributions derived from the PELDOR data (solid black line), and R1 modelled onto the two Trim 25cc crystal structures (PDB ID 4LTB: blue dashed line; and PDB ID 4CFG: red dashed line), in all cases distributions were normalised so their maxima were equivalent.

6.2.2 Comparison Between Experimental and Modelled Distance Distributions

Experimental distance distributions differed from model distance distributions for both Trim 25cc crystal structures at all labelling sites except for Trim 25cc S272R1 (figure 6.1). Deviations in distances between experimental and modelled distance distributions followed a pattern. Experimental distance distributions shifted to shorter ranges than their modelled counterpart as the labelling site was moved

towards the N-terminus of Trim 25cc from S272, and longer ranges as the labelling site was moved towards the C-terminus of Trim 25cc from S272. Modelled distance distributions also varied between the two Trim 25cc crystal structures, seen most prominently at Trim 25cc E293R1 (figure 6.1).

6.3 T_m Measurements

6.3.1 Measuring and Fitting T_m Data

T_m was measured for four different 4'-amino TEMPO concentrations along with the different labelling sites on deuterated Trim 25cc. T_m was determined by fitting the stretched exponential from equation 6.1 to the experimental data.

$$P(t) = P(0)e^{-\left(\frac{t}{T_m}\right)^x} \qquad (6.1)$$

Where P(t) is the echo height at time t; P(0) is the echo height at time 0, fixed at 1.0 for the fits; and x is a dimensionless value. In all cases Trim 25cc T_m data contained both ESEEM and dipolar oscillations, making fitting of the T_m curve non-trivial. As a result T_m decays were truncated to remove the ESEEM and dipolar oscillations before being fitted in the manner previously reported (Lindgren et al., 1997).

It was reasoned that: the presence of ESEEM or dipolar coupling would increase decay from the fit, lowering the T_m value. Therefore, the level of truncation that excluded ESEEM or dipolar coupling would give the maximum T_m. To determine maximum T_m values, experimental T_m data was fitted using various truncations from the zero time (t(0)). T_m values from fits using different levels of truncation to the experimental data were plotted against the time the truncation was carried out

to. These plots gave noticeable maxima of T_m values in most cases, which was treated as the T_m of the labelling site (figures S6.2, S6.3, and S6.4).

For cases where no clear maxima could be observed (marked with a *; figures S6.2, S6.3, and S6.4), the T_m value used for the labelling site was the maximum value outside of the noise in the T_m against level of truncation plots. This noise was introduced by the reduction in S/N at greater truncations of the experimental T_m data.

6.3.2 Tm measurement Analysis

A scatterplot of the T_m against 4'-amino TEMPO concentration showed the T_m increased as the concentration was lowered. With lower concentrations decreasing the effective mean distance between 4'-amino TEMPO molecules (figure 6.2, A). In a scatter plot of modal distances for the different Trim 25 labelling sites against the labelling site's T_m, there was no clear relationship between the T_m and the modal distance (figure 6.2, B.). This suggested another relaxation mechanism was dominant for R1 bound to a deuterated protein structure.

A.

1.) 4'-Amino TEMPO Concentration Against T_m Scatter Plot

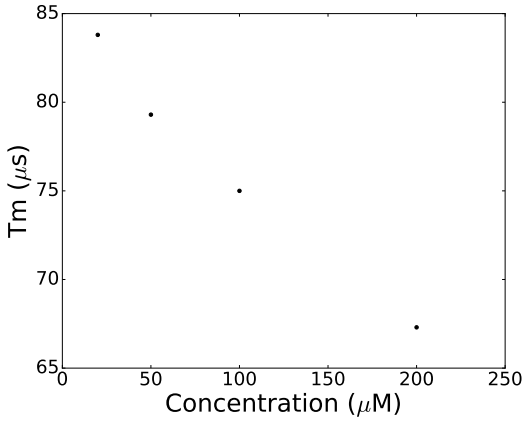

2.) A Table of 4'-Amino TEMPO Concentration along With the Respective T_m

4' Amino TEMPO Concentration (μM)	Tm (μs)
20	83.8
50	79.3
100	75.0
200	67.3

B.

1.) Deuterated Trim 25 Modal Distance Against T_m Scatter Plot

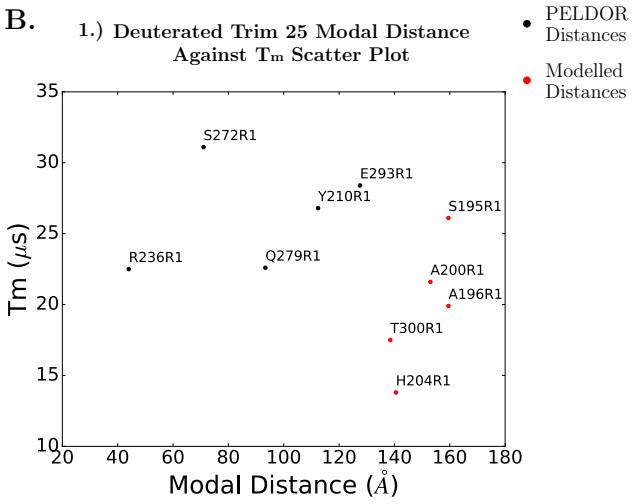

2.) A Table of the Trim 25cc Modal Distances along With the Respective T_m At the different R1 Labeeling Sites

R1 binding Site	Modal Distance ($\AA$)	Tm (μs)
S195R1	159.5	26.1
A196R1	159.5	19.9
A200R1	153.0	21.6
H204R1	140.5	13.8
Y210R1	112.4	26.8
R236R1	44.0	22.5
S272R1	71.0	31.1
Q279R1	93.4	22.6
E293R1	127.5	28.4
T300R1	138.5	17.5

Figure 6.2: (A) A scatterplot (1) and table (2) of 4' amino TEMPO Tm values against sample concentration. (B) A scatterplot (1) and table (2) of the modal distance determined by PELDOR (black), or modelled onto the Trim 25cc crystal structure (PDB ID: 4LTB, red), against the T_m of different R1 binding positions onto Trim 25cc.

6.4 Structure of the Coiled Coil Domain from Trim 25

6.4.1 Differences Between Distances from R1 Modelled onto the Crystal Structures and PELDOR Data

Differences between modelled and experimental distance distributions were observed between the crystal and glass phase structures of Trim 25cc. These implied differences between the Trim 25cc crystal and glass phase structures, likely due to changes in bending or coiling of the coiled coil domain.

Of these two possibilities, differences to the coiling of the coiled coil domain was thought to be more likely. The evidence behind this was: depending on whether the R1 binding site was towards the N or C-terminus of Trim 25cc from residue S272, experimental distance distributions were located at longer or shorter ranges than modelled distance distributions (figure 6.1). Bending of the coiled coil would be expected to produce shifts in the range of distance distributions dependent upon the topology of the coiled coil where the labelling site was located.

Further coiling or uncoiling of the coiled coil would shift distances in a manner dependent upon which α-helix forming the coiled coil the labelling site was located upon. Because Trim 25cc forms an antiparallel homodimer, at most sites the coiled coil was made up of one α-helix towards the C-terminus, and one α-helix towards the N-terminus of the constituent Trim 25cc monomers. This would produce the observed pattern where distance distributions shift to longer or shorter ranges in a manner dependent upon whether the labelling site was towards the N or C-terminus of Trim 25cc.

Further supporting this hypothesis is the observation that the coiled coil domains within the crystal structures produced different distance distributions based upon different coiling of the coiled coil domains at their extremities (figure 6.3).

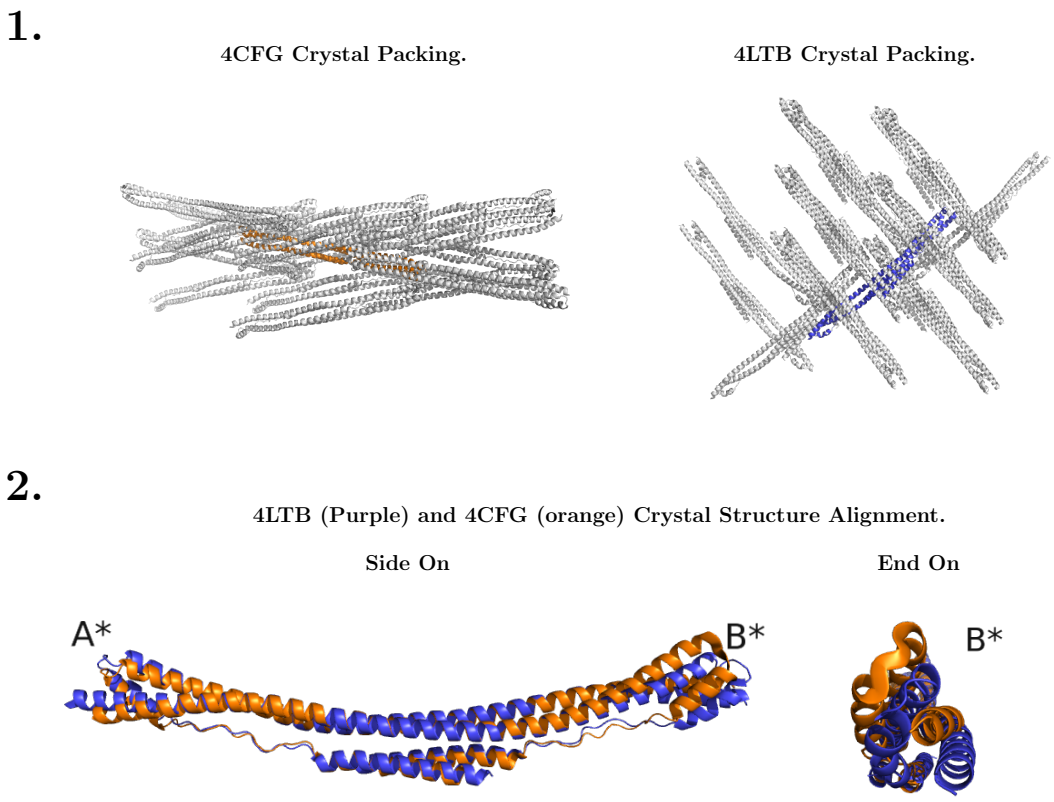

Figure 6.3: (A) Different crystal packing for the Trim 25cc crystal structures (PDB ID: 4LTB and PDB ID: 4CFG). (B) (left) An alignment of the two different crystal structures (4LTB in blue and 4CFG shown in orange). The two ends were assigned A and B*, with the B* end having greater discrepancies in the alignment than the A* end. (right) A view of the aligned structure looking down the B* end, differences in coiling and bending between the aligned structures are observable.*

6.4.2 The Difference in the Hydrophobic Interactions between Trim 25 Crystal Structures Coiled Coil Domains

Differences in the coiling of the coiled coil domain suggested a change in the interactions at the hydrophobic interface. This was investigated by taking advantage of the difference in coiling between the two crystal structures deposited in the PDB (PDB IDs: 4CFG and 4LTB). The hydrophobic interface of the Trim 25 coiled coil domain was split into 'holes' and 'knobs'. The 'hole' was the area of the hydrophobic interaction containing two hydrophobic residues. These created a gap which a single hydrophobic residues from the opposing α-helix, the 'knob', slotted into. To investigate any differences in hydrophobic interactions, the protein backbone of the 'hole' from the two crystal structures were aligned at each hydrophobic interaction in the area where the coiled coil domains began to diverge. This allowed differences in the position of the corresponding 'knobs' to be observed (figure 6.4).

In most cases there was little difference in the hydrophobic interaction between the two different crystal structures. However, there was a notable shift in the position of A216 in the K284'/K285' hole between crystal structures (figure 6.4, B). This shift implied the Trim 25cc domain could dynamically coil and uncoil, due to the large hydrophobic hole produced by K284'/K285' giving the relatively small A216 room to move.

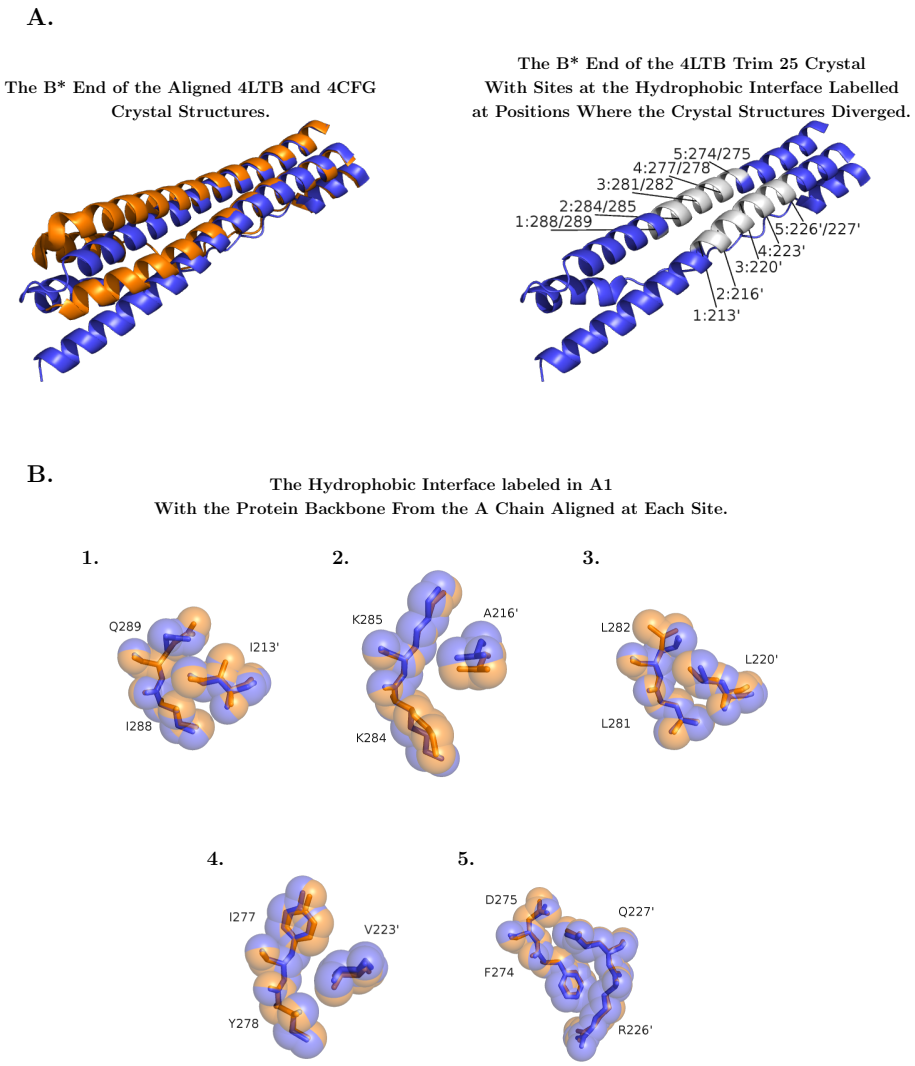

Figure 6.4: (A) (left) The B end of the Trim 25cc crystal structure alignment (PDB ID: 4LTB in blue and PDB ID: 4CFG in orange) showing the region where the aligned structures began to diverge. (right) The coiled coil region of 4LTB with the coiled coil domain where the crystal structures alignment began to diverge shown in white, residues contributing to the hydrophobic dimerization domain within this region are labelled with the B chain residues identified with an ' after the number. (B) Alignments of the protein backbone for the A chain (higher numbered residues) at each hydrophobic site labelled in A (right), allowing local deviations*

6.5 Structural Implications

The modelled modal distance from Trim 25cc 4CFG E293R1 was shorter than the modelled modal distance from Trim 25cc 4LTB E293R1. Alignment of the two crystal structures revealed the main difference between 4CFG and 4LTB was an increased left-handed coiling for 4CFG at the extremity of the coiled coil domain. The experimental distance distribution for Trim 25cc E293R1 was at a longer range than the modelled distance distribution for 4LTB. Provided left-handed or right-handed coiling results in similar distance shifts to those observed between the two crystal structures, this would indicate that in the glass phase the coiled coil domain of Trim 25cc became more right-handed.

This change could be a consequence of the K284'/K285' to A216 'hole' and 'knob' pairing. Within this region a shift of A216 towards K284' was observed to enable Trim 25cc 4CFG to have a more left-handed coiled coil domain than Trim 25cc 4LTB (figure 6.4). There is room within the K284'/K285' 'hole' for A216 to be shifted towards K285' from its position in the Trim 25cc 4LTB crystal structure. Such a shift could enable the coiled coil domain to form a more right-handed coil than observed in Trim 25cc 4LTB. This raises the possibility that the Trim 25cc coiled coil domain undergoes dynamic coiling and uncoiling in solution.

The data presented here can be seen as a possible starting point to determine the conformations and dynamics of the coiled coil domain of Trim 25 in solution. The first objective to find out if distances from PELDOR change when the SUMO tag is removed, and secondly whether there are any changes in the position of the C-terminal helix (the L2 domain) in constructs with and without the SUMO tag. The

L2 domain positions are important because they define where the PRY-SPRY domains are placed in relation to the rest of the protein construct. The observation of a change to the coiled coil domain due to the presence of the SUMO tag, would raise the question of whether coiling is affected by the presence of the B-Box and RING domains.

6.6 The Effect of Protein Deuteration on T_m

6.6.1 Extension of the T_m Using Protein Deuteration

This study along with previous work (Ward et al., 2010) has demonstrated the large gains in PELDOR sensitivity that can be achieved by deuterating the solvent and the underlying protein structure. There were no strong correlations observed between T_m and intramolecular spin label distances. However, significant differences in T_m values were observed between labelling sites, making it likely that hitherto unknown factors were primarily responsible for dephasing within deuterated protein structures.

The presence of deuterium ESEEM and oscillations caused by electron spin-spin interactions, compounded by the lack of echo intensity at the 0 μs time point, made fitting experimental T_m data non-trivial. Sharp drops caused by both ESEEM and electron spin-spin interactions prevented the estimation of an accurate echo intensity at 0 μs, introducing an error into the fit. In addition, oscillations caused by ESEEM and electron spin-spin interactions negatively affect the accuracy of the T_m fit. No method was determined to find an accurate echo intensity at 0 μs. However, errors from ESEEM and the electron spin-spin interactions could be reduced by fitting experimental T_m data after oscillations had fully decayed. The point where oscillations within the T_m data had decayed to 0, was determined by

first plotting the T_m from fitting the experimental data within the first n μs removed against the value of n for the fit (referred to as the T_m plot). The maximum T_m value from the T_m plot was then used as the T_m of the sample. The maximum T_m from the plot was chosen because ESEEM and electron spin-spin interactions resulted in an enhanced echo decay in the T_m curve, making errors induced by the presence of oscillations cause the fit to have a lower T_m than the actual T_m of the system.

This method had some disadvantages:

- The S/N ratio gets progressively smaller as the truncation to is the T_m curve is increased.
- The initial measured echo intensity was assumed to be the intensity at 0 μs in the fits.
- There were cases where the T_m value does not reach a maximum before a significant amount of noise was introduced into the T_m plot, leading to the choice of the maximum value before noise was introduced into the T_m plot for the T_m.

These slight errors may result in unreliable data; however, they do not account for the lack in correlation between variations in the T_m with spin-spin distances, nor the observed variations in T_m curves.

6.6.2 4'-amino TEMPO T_m Against Deuterated Trim 25cc T_m

T_m values from varying concentrations of 4'-amino TEMPO were 3 or 4 times the T_m values within Trim 25cc. This suggests large increases in sensitivity would be available if label distance becomes the only limiting factor for echo decay.

In a recent study the time period of PELDOR experiments was seen to increase further than was measured here using sparse labelling of the multimeric protein GroEL (Schmidt et al., 2016). It is likely the increase in T_m due to sparse labelling was down to a lower multi spin effect within the protein system. The longest T_m measured for GroEL was 26 μs, within the range of T_m measurements shown in this study, suggesting a greater initial echo intensity could allow PELDOR data to be recorded out to 80 μs. Additionally, the idea that singularly labelled species within the GroEL samples increased the time period of PELDOR, raises the tantalising possibility of increasing the time period of PELDOR experiments at a sacrifice to modulation depth by the addition of free spin label to the protein sample.

6.7 Conclusion and Prospects

Trim 25cc presented a rod like protein structure, which provided PELDOR experimental time periods greater than previous work on a deuterated globular H3-H4 tetramer (El Mkami et al., 2014). This observation of Tm being depend upon the topology of the underlying protein structure, has the caveat that the large and globular multimeric membrane protein GroEL has been demonstrated to give equivalent values of T_m to those observed for Trim 25cc under sparse labelling

conditions (Schmidt et al., 2016). These discrepancies highlight that further investigations are required to study the effect a deuterated protein environment has on dephasing within EPR.

Future investigations on the effect of a deuterated protein environment upon T_m would first test differences in T_m from a range of different protein folds, that are singularly labelled with R1 at solvent exposed sites. This information on the change in T_m with labelling site would allow a more directed approach to improve sample preparation for biological PELDOR, as well as possibly providing a means to gain limited structural information based upon spin label relaxation.

A second avenue of investigation would be to investigate the possible gains in experimental time period by increasing the ratio of unbound nitroxide to labelled protein within a PELDOR sample. Additionally, the extent the ratio of unbound nitroxide to labelled protein reduces the modulation depth of the sample is valuable information on whether using this increased experimental time period is viable.

Protein deuteration is only recently being used regularly for PELDOR measurements. Consequently, there is a dearth of information on the extent of the enhancement to PELDOR measurements because of protein deuteration, and the significant relaxation pathways within a fully deuterated environment. Results of this study have shown site-specific differences in T_m values for R1 bound at different positions on the Trim 25 coiled coil region (Trim 25cc). R1 binding positions used in this study covered a range of distances between 36 Å to 124 Å, with measurements within this range not showing the expected trend of

lengthening T_m values and distances in tandem. There were significant variations in T_m values between sites suggesting relaxation mechanisms related to the underlying protein structure were present. In addition, discrepancies between modelled and PELDOR distance distributions showed differences between the crystal and glass phase structure of Trim 25cc, further confirmed by different distances for R1 modelled onto the two Trim 25cc crystal structures.

The coiled coil domain acts as a scaffold for Trim 25, causing different coiled coil conformations to affect the positions of the binding (PRY-SPRY) and functional (RING) domains of Trim 25. Results from this study are inconclusive on both relaxation within a deuterated sample and the glass phase structure of Trim 25cc. Nevertheless they provide a starting point for future studies into these features of the deuterated system.

Chapter 7: Suitability of the Rigid Spin Label Rx for Orientation Selective PELDOR

7.0 Summary

At present PELDOR is used for determining distances within biological structures, however there is also orientation data present within PELDOR. To access orientation data two conditions must be met: the spin label must be rigid enough to present a well-defined orientation distribution; and PELDOR should be run under a high enough magnetic field strength to take advantage of any anisotropy in the g factor. Within this chapter the former of these conditions has been addressed by presenting PELDOR and molecular dynamic data for different binding conformations of the bifunctional nitroxide spin label Rx. It was observed binding Rx between residues numbered i and i+1 on the α-helix produced a tight monomodal distribution, ideal for making orientation measurements. Additionally, constraints on the labels motion at this position were caused by steric hindrance created by buttressing amino acid residues, presenting the bulk of these residues as an additional consideration when choosing Rx binding sites for making orientation measurements using PELDOR.

7.1 Introduction

7.1.1 Orientation Selective PELDOR

The pulsed EPR technique most often used within biological structures is PELDOR, which allows measurements of distances between labelled sites. Raw PELDOR data also has an orientation component that is rarely exploited for refining biological structures due to the conformational heterogeneity of commonly used spin labels, along with low microwave frequencies often used in PELDOR experiments. Recent advances in spectrometers available for pulsed EPR measurements has led to the commonly used frequency rising from X-band (~9.4 GHz) to Q-band (~35 GHz)

(Kuzhelev et al., 2015; Zou and Mchaourab, 2010), this leads to increased sensitivity of PELDOR experiments, allowing faster data acquisition and higher sensitivity(Ghimire et al., 2009). Orientation measurements ideally require a further raising of the microwave frequency to W-band (~95 GHz) (Denysenkov et al., 2006; Kaminker et al., 2013; Reginsson et al., 2012b; Schiemann et al., 2009). This increase in frequency and field strength broadens absorption spectra from unpaired electron containing species, consequently encompassing the spectra requires a broader available bandwidth than at lower frequencies. Introduction of a resonant cavity free W-band spectrometer using high-powered microwave radiation (HiPeR) (Cruickshank et al., 2009) enables the placement of microwave pulses across the whole spin label absorption spectra. This lack of resonant cavity gives an additional advantage, allowing loading of greater sample volumes into the spectrometer (Cruickshank et al., 2009).

7.1.2 Spin Label Properties

This study focuses on how spin labelling can be improved to accommodate orientation measurements within most protein structures. For distance measurements using PELDOR the important factor to consider is how predictable the spin label distribution is in relation to the protein backbone (Hagelueken et al., 2012), the majority of spin labels have a 'leg' attaching to the Cα on the protein backbone, flexible enough to average out spin label orientations (Jeschke, 2013). A series of different methods have already been used to reduce spin label flexibility for the purpose of CW-EPR measurements (Hubbell et al., 2013; Toledo Warshaviak et al., 2013) such as; increasing the spin labels bulk (Hubbell et al., 2013); using an unnatural amino acid spin label (Toniolo et al., 1998); and binding the label to the protein backbone at multiple sites (Fleissner et al., 2011). The

unnatural amino acid TOAC (Toniolo et al., 1998) gives the most rigid label distributions, however its use is limited by difficulty of introduction into larger protein structures. Increasing the bulk of a spin label provides a less dramatic reduction in spin label motion to the introduction of TOAC, however allows labels to be introduced onto protein backbone with greater ease. Using a bifunctional spin label gives a tighter distribution than bulky mono-functional labels, while being able to be introduced into a protein structure with greater ease than unnatural amino acids (Cunningham et al., 2015; Fleissner et al., 2011). The use of a bifunctional label for orientation measurements raises the question of which, if any, label binding conformations to the protein backbone gives distributions suitable for orientation measurements?

7.1.3 Issues Using R1 for Orientation PELDOR

The most commonly used nitroxide label is R1, which binds cysteine residues using methane methyl sulphonate chemistry. It has a single attachment point to the protein backbone structure giving a single binding 'leg' with a high degree of flexibility, making them suitable for orientation studies only under very specific structural conditions (Polyhach et al., 2011b). The bifunctional version of R1 is Rx, where the nitroxide ring is stabilized by the introduction of a second binding 'leg', previous studies have used Rx as a cross linking agent or rigid spin label for CW-EPR. Investigations into its application for CW-EPR showed the motion of Rx was close to the rigid limit, indicative of a highly constrained distribution of the nitroxide ring; an observation further supported by a tight distance distribution from PELDOR data (Fleissner et al., 2011). This constrained distance distribution suggested Rx was localized enough to allow orientation measurements. To be useful for protein structural determination the nitroxide must be bound to a

commonly found structural feature, limiting the sites tested for binding Rx to the α-helix or β-sheet. Within this chapter data is presented from Rx bound to the α-helix or β-sheet of a model protein in a series of different attachments, the label distribution was modelled using molecular dynamics and experimental confirmation of the model was achieved by comparing distance distributions between the modelled structure and experimental data.

7.1.4 The Structure of vacuolar protein sorting-associated protein 75 (Vps 75)

The model protein chosen for this study was vacuolar protein sorting-associated protein 75 (Vps 75) which has a series of crystal structures deposited into the protein data bank (Berndsen et al., 2008; Hammond et al., 2016; Park et al., 2008). Crystal structures show a nucleosome assembly protein 1 (Nap1) like fold consisting of an anti-parallel α-helical dimerization domain and two 'earmuff' domains, each formed by a β-sheet lying on top of a hydrophobic pocket (Park et al., 2008; Tsubota et al., 2007); allowing the investigation of symmetrical Rx sites bound to either the β-sheet or α-helix.

7.1.5 The Biological Function of Vps 75

Vps 75 is a member of the nucleosome assembly protein (Nap) family of proteins, it is found in yeast alongside the families founding member, nucleosome assembly protein 1 (Nap1) (Ishimi et al., 1987; Selth and Svejstrup, 2007). In cells Vps 75 is a histone chaperon with an affinity for all four-core histones (H2A, H2B, H3, and H4), along with the histone acetyl transferase (HAT) regulator of Ty1 transposition 109 (Rtt109) (Driscoll et al., 2007; Hammond et al., 2016; Park et al., 2008). This combination of binding partners gives Vps 75 a role in the acetylation of K56 on H3 (H3-K56ac) and K9 on H3 (H3-K9ac), fulfilling a similar function to Anti

silencing function 1 (Asf1) (Berndsen et al., 2008). H3-K56ac is important for allowing DNA to unravel from the histone octamer in the double strand break repair pathway (Tsubota et al., 2007), and H3-K9ac is an important modification for the deposition of histones onto DNA (D'Arcy and Luger, 2011; Fillingham et al., 2008).

7.1.6 Vps 75 binding Partners

The main binding partners of Vps 75 are Rtt109 and H3-H4. Each partner binds its own particular site on Vps 75: Rtt109 binds the Vps 75 earmuff regions; and H3-H4 binds the central groove of the Vps 75 dimer. Vps 75 binds Rtt109 at a stoichiometry of 2:1 or 2:2, and the H3-H4 dimer at a stoichiometry of 2:1 or 4:2 (Breitgoff et al., 2017; Fillingham et al., 2008; Hammond et al., 2016). Under physiological salt conditions, Vps 75 forms a ring shaped tetramer, evident from low resolution crystal structures, presenting a possible open and closed conformation (Bowman et al., 2014). The central binding groove of the closed conformation is too narrow to accommodate a H3-H4 tetramer, which suggests the tetramer of Vps 75 splits apart upon binding H3-H4, with each homodimer of Vps 75 interacting with an H3-H4 dimer (Hammond et al., 2016). This leads to the possibility Vps 75 adopts a tetrameric conformation in order to self-chaperone by occluding the Rtt109 and H3-H4 binding sites.

7.1.7 Binding Rx to Vps 75

Rx has previously been used as a cross linking agent to produce singly labelled Vps 75 dimers and a rigid spin label for CW-EPR, Although the crosslinked Vps 75 system was used to determine the tetrameric arrangement by measurement of Rx orientation, there has yet to be a comprehensive assessment of the suitability of Rx

for making orientation measurements within protein structures. In this chapter the possibility of using Rx for orientation measurements when bound to commonly found protein structural features has been investigated. To this end, data is shown for Rx bound in 3 different arrangements on the α-helix and 3 different arrangements on the β-sheet. Taking i as the residue number, these conformations were from i to i+1, i to i+3, and i to i+4 on the α-helix; and from i to i+2, perpendicularly between β-strands, and diagonally between β-strands on the β-sheet. Sites were modelled onto the crystal structure of Vps 75 (PDB ID: 2ZD7) using Xplor (figure 7.1), and model accuracy was confirmed by comparing distances from modelled Rx distributions and distance distributions observed experimentally using PELDOR. The suitability of different Rx binding sites for orientation measurements was determined by analysing modelled orientation distributions for the nitroxide ring with respect to the bound secondary structural feature. Different binding arrangements of Rx greatly affect its suitability for orientation selective PELDOR, showing binding Rx from i to i+1 on the α-helix to be the most promising site for making orientation measurements.

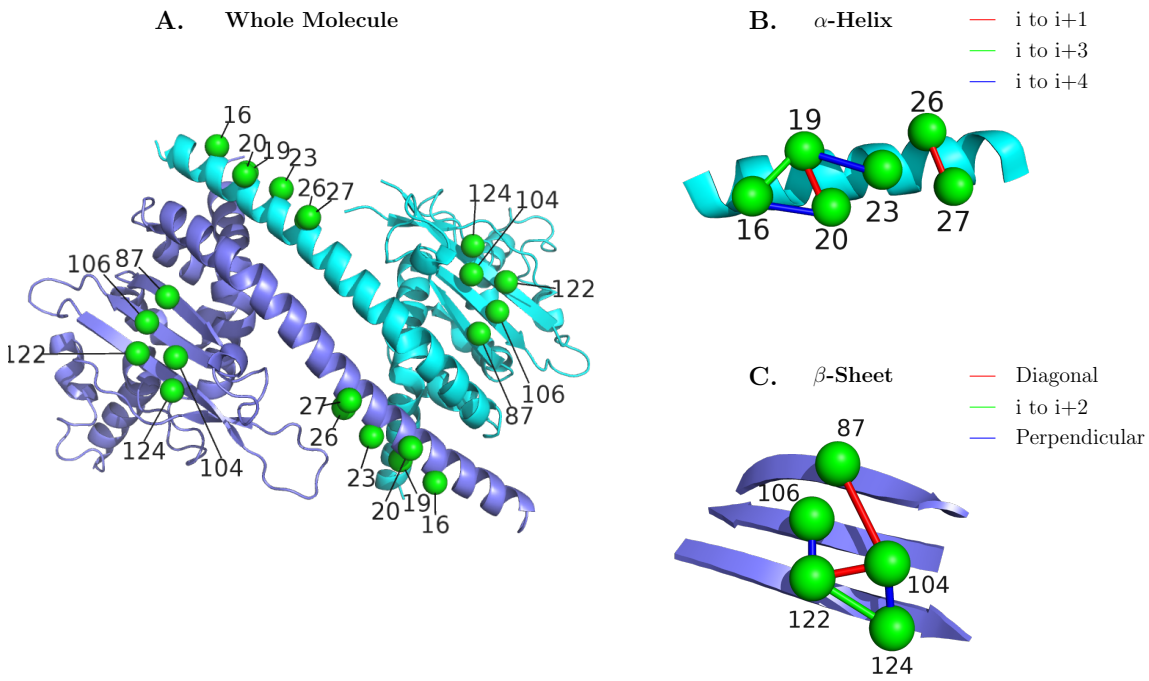

Figure 7.1: The Vps 75 homodimer crystal structure (PDB ID: 2ZD7) with the A chain monomer coloured in cyan and the B chain monomer coloured in purple, green spheres highlight residues involved in Rx labelling sites. (A) An image of the full Vps 75 homodimer with annotations designating sites used for labelling. (B) A region of the Vps 75 α-helix with pairs of residues used for binding Rx linked, the line colour was changed to show Rx bound between i to i+1 (red), i to i+3 (green), or i to i+4 (blue). (C) Sites for Rx bound to the β-sheet with each binding site linked and the line colour changed based upon whether Rx was bound at i to i+2 (green), perpendicularly between strands (blue), or diagonally between strands (red).

7.2 PELDOR and Xplor Distance Distributions

7.2.1 PELDOR distance distributions

PELDOR data from Vps 75 constructs mutated to contain the chosen Rx binding sites were analysed to produce experimental distance distributions. Confirmation of modelled structures relied on comparing experimental distance distributions to

distance distributions from molecular dynamics. This required reliable experimental distance distributions, consequently raw PELDOR data from each site had to contain at least two oscillations (appendix figures S7.1 and S7.2). Experimental distance distributions were bimodal at the majority of sites, with individual distribution widths of ~10 Å. The most notable exception to this rule was T106-T122Rx, which produced a monomodal distance distribution with a width of ~20 Å (figure S7.2). Previous studies have demonstrated the nitroxide ring of Rx is preferentially present as a bimodal distribution (Fleissner et al., 2011), which is likely the primary factor leading to split distance distributions. As such, it is possible experimental data from T106-T122Rx results from Rx being oriented in a manner that presented a broad monomodal distribution. Other sites that produced a monomodal distance distribution, A19-K20Rx and S104-T122Rx, had similar distance distribution widths to those from individual bimodal distance distributions. These were thought to be a consequence of one or both Rx nitroxide ring distributions being obscured at these sites.

7.2.2 Xplor distance distributions

Molecular dynamics were performed on Rx, modelled onto a crystal structure of Vps 75 (PDB ID : 2ZD7) using Xplor (Schwieters et al., 2003). During the dynamics run the protein backbone was constrained using a spatial harmonic restraint, leaving only the backbone of the Rx binding sites and side chains mobile. Modelled distance distributions were determined by measuring distances from each individual nitroxide nitrogen from Rx conformations modelled on one side of the dimer to the nitroxide nitrogen of all modelled conformations on the opposing side.

7.2.3 Comparison between Modelled and Experimental Distance Distributions for β-sheet sites

Model fidelity was assessed by comparing experimental and modelled distance distributions. These comparisons revealed significant differences for most β-sheet sites; with modelled data presenting multiple different peaks at T122-V124Rx (i to i+2); an absence of experimental distance distributions at S104-V124Rx (perpendicularly between β-strands) and K87-S104Rx (diagonally between β-strands); or a shift in the modal distance at S104-T122Rx, K87-S104Rx (both diagonally between β-strands) and T106-T122Rx (perpendicularly between β-strands) (figure 7.2, B). Sites displaying additional peaks in the experimental data, S104-V124Rx (perpendicularly between β-strands) and K87-S104Rx (diagonally between β-strands), were both located on the edge of the β-sheet closest to the adjacent α-helix/loop motif. The cause of differences between modelled and experimental distance distributions at these sites were likely differences in the position of the α-helix and loop region between the modelled (crystal) and experimental (glass-phase) structures of Vps 75. Additional possible causes of differences between modelled and experimental distance distributions within the β-sheet were deformations to the glass-phase structure from binding Rx; crystal packing forces within the crystal structure used for molecular dynamics; or deformations of the underlying hydrophobic pocket between glass-phase and crystal structures (Park et al., 2008). T106-T122Rx, bound perpendicularly between β-strands with one binding site in the centre of the β-sheet, gave the greatest observable difference between modelled and experimental data. At this site the modelled modal distance was shorter with a narrower width than its experimental counterpart. The greater divergence for T106-T122Rx compared to remaining sites, where both binding sites were positioned around the edge of the

sheet, support the underlying hydrophobic pocket creating a convex or concave distortion to the β-sheet in the glass-phase structure compared to the crystal structure. Regardless of cause, significant differences between modelled and experimental distance distributions from β-sheet Rx sites reduced reasonable conclusions that could be made from modelled structures.

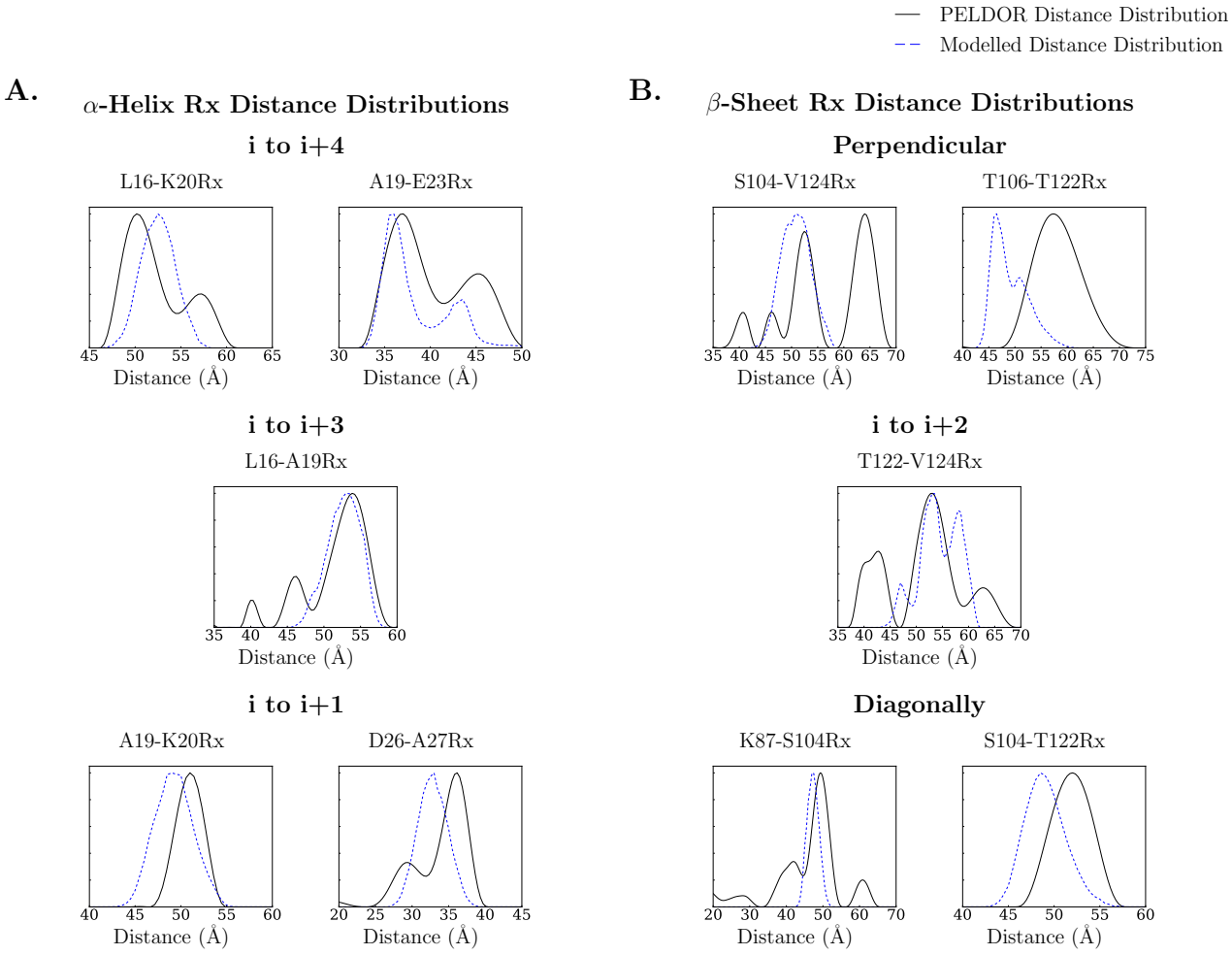

Figure 7.2: Distance distributions from PELDOR data (solid black line) plotted alongside Rx modelled on the Vps 75 crystal structure (PDB ID: 2ZD7, dashed blue line) for Rx binding sites on the α-helix (A) and β-sheet (B).

7.2.4 Comparison Between Modelled and Experimental Distance Distributions for α-Helical Sites

Modelled distance distributions for Rx bound to the α-helix differed from their experimental counterparts by either; producing a monomodal modelled distribution in contrast to bimodal experimental distributions at sites L16-K20Rx (i to i+4) and D26-A27Rx (i to i+1); or shifting the breadth and range of the modelled distance distribution compared to the experimental distance distribution at sites A19-E23Rx (i to i+4) and A19-K20Rx (i to i+1) (figure 7.2, A). These discrepancies were likely caused by oversampling naturally unfavourable energy conformations of Rx in the molecular dynamics run, a result of the simulation only taking bonding, harmonic restraints and Van Der Waals (VDW) interactions into consideration. Experimental distance distributions were thought to be a result of the canonical bimodal nitroxide distribution for Rx, the shift in distance distributions between the modelled and experimental data were likely caused by unfavourable Rx energy states modelled onto the protein backbone. The rationale behind this conclusion is: for the modelled distance distribution to become monomodal the distribution of the Rx nitroxide group had to become monomodal; the placement of the mode from the modelled distance between modes of the bimodal experimental distance implied the monomodal nitroxide distribution acted as a spatial average of the nitroxide; such a spatial average would be achieved by oversampling of unfavourable energy states for Rx in between the naturally occurring bimodal distribution. Factors that make these states unfavourable are the bimodal conformations being made energetically favoured due to interactions between Rx and the protein backbone, or dihedral restraints in the binding legs of Rx making the central nitroxide distribution energetically unfavourable.

7.2.5 Rx Binding Sites

The α-helix provided Rx binding sites with comparable experimental and modelled distance distributions. β-sheet sites gave fewer similarities and differences in modelled and experimental distance distributions were more difficult to explain by modelling error, this made these discrepancies likely a consequence of deformations in the underlying secondary structural feature. The most promising sites for orientation selective PELDOR were A19-K20Rx (i to i+1) on the α-helix, and S104-T122Rx (Diagonally between strands) on the β-sheet, both gave monomodal distance distributions with widths of ~10 Å (figure 7). Additionally, A19-K20Rx (i to i+1) on the α-helix gave the greatest similarity to the modelled structure, making it the most promising site for performing orientation selective PELDOR.

7.3 Xplor Angles Plot

7.3.1 Tilt, Twist and Roll Distributions

Nitroxide ring orientations were described by three rotational transformations that positioned the nitroxide ring in a predefined orientation with respect to the underlying secondary structural feature (chapter 3, section 3.3.4). Rotational angles were labelled Tilt, Twist and Roll; Tilt represented a rocking motion around the Cα to Cα vector of the Rx binding position; Twist represented a waving motion across the Cα to Cα vector; and Roll represented a turning motion around the nitroxide axes. The Tilt, Twist and Roll motions were restricted by different features of Rx binding conformations; the Twist motion is affected by Rx binding at two points to the protein backbone; the Tilt motion is dependent on the surrounding protein structure; and the Roll motion is dependent on the ability of

the ‘legs’ of Rx to move independently of one another. Orientation distributions for each α-helical and β-sheet site were made by producing histograms of the rotational transformations for structures pulled off the molecular dynamics run at each site (figures 7.3 and 7.4). To make an informed decision on what constitutes a good Rx binding conformation for orientation measurements, comparisons of the Tilt, Twist and Roll were made between the different binding sites on either the α-helix or β-sheet.

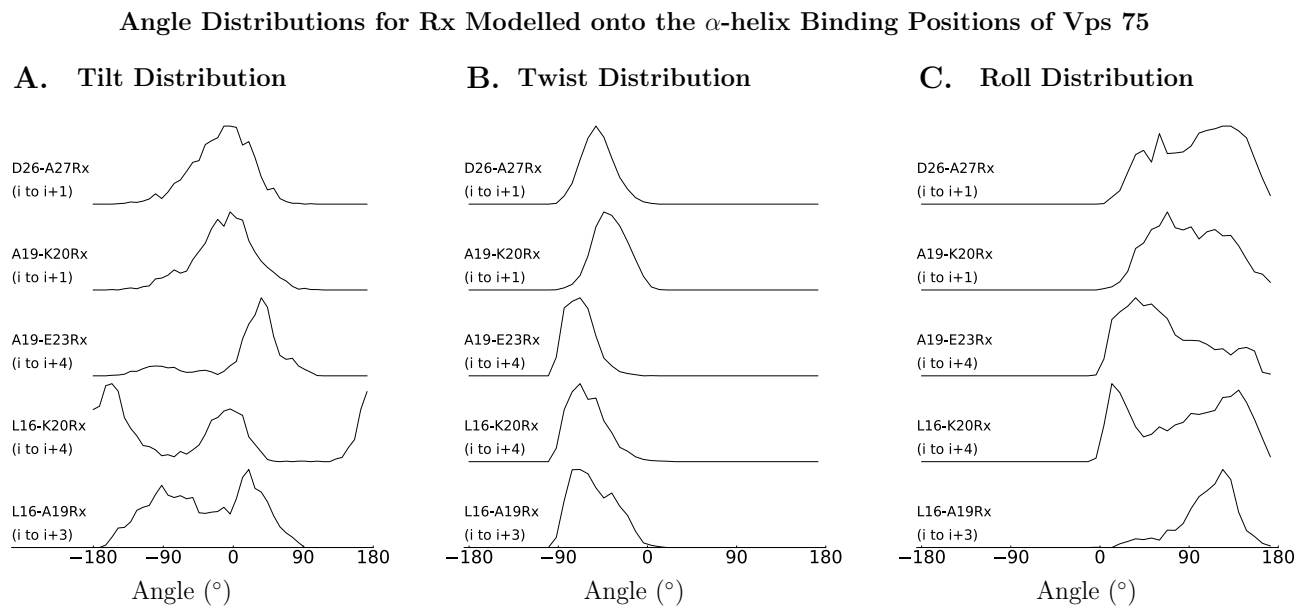

Figure 7.3: Tilt (A), Twist (B), and Roll (C) angle distributions for Rx modelled onto the α-helix of Vps 75.

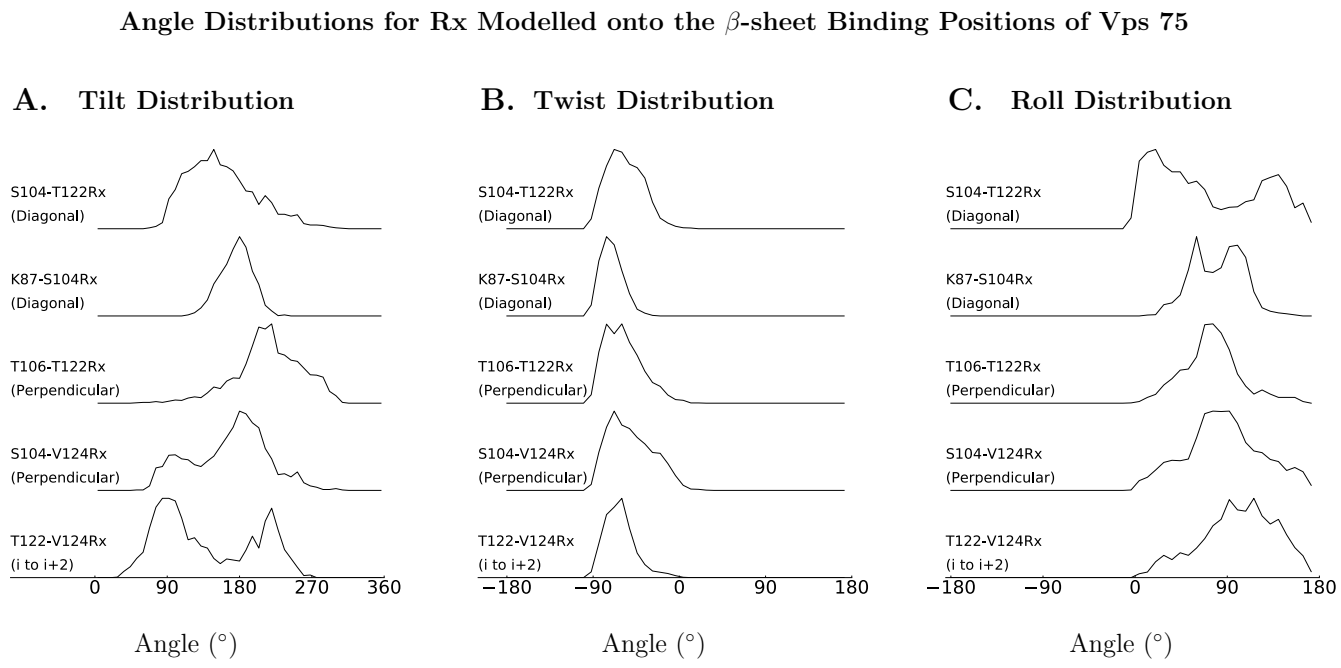

Figure 7.4: Tilt (A), Twist (B), and Roll (C) angle distributions for Rx modelled onto the β-sheet of Vps 75.

7.3.2 α-Helix Binding Sites

In α-helix angle plots, Twist distributions were narrow with little variation between sites; Roll distributions covered a similar range of angles with no observable pattern based upon the binding conformation of Rx; and Tilt distributions were bimodal for Rx bound from i to i+3 (L16-A19Rx) or i to i+4 (L16-K20Rx and A19-E23Rx), and monomodal for Rx bound from i to i+1 (A19-K20Rx and D26-A27Rx). This pattern identifies Tilt as the motional regime most dependent upon the binding arrangement of Rx. When performing orientation measurements using PELDOR it is important to limit the range of possible nitroxide ring orientations, this was best achieved when the ring was forced into a monomodal Tilt distribution. Of the α-helical sites only Rx bound from i to i+1 (A19-K20Rx and D26-A27Rx) gave monomodal Tilt distributions, enforced by the position of buttressing amino acid residues that obfuscate one or both of the low energy conformations of Rx.

7.3.3 β-sheet Binding Sites

Angle plots for Rx binding conformations on the β-sheet have no experimental validation, as such any conclusions reached should only be treated as a hypothesis based entirely upon the molecular dynamics run. Roll and Twist angle distributions showed similar patterns in β-sheet sites as observed at α-helix sites. Tilt angle distributions were bimodal for S104-V124Rx (perpendicularly between β-strands) and T122-V124Rx (i to i+2), and mono modal for K87-S104Rx (diagonally between β-strands), S104-T122Rx (diagonally between β-strands) and T106-T122Rx (perpendicularly between β-strands). β-sheets have less uniform topologies than α-helices, complicating the prediction of structural features within

the β-sheet that interfere with Rx nitroxide distributions. In the case of T106-T122Rx (perpendicularly between β-strands) these deformations created a monomodal Tilt distribution by changing the orientation of Rx binding legs and the position of surrounding amino acid side chains. Sites where Rx was bound diagonally between strands of the β-sheet (K87-S104Rx and S104-T122Rx) also produced monomodal Tilt distributions (figure 7.3), a result of buttressing amino acid residues positioned in a similar manner as i to i+1 on the α-helix.

7.4 CW-EPR Data

7.4.1 CW-EPR

CW-EPR spectra for the different Rx binding sites revealed nitroxide motions were close to the rigid limit (figure S7.3). This was indicated by an increase in central line width and spectral width observed between the low field peak and high field trough, referred to as the 2Azz' value (Mason and Freed, 1974). The 2Azz' values were measured from CW-EPR spectra of the different Rx binding sites to display slight but significant difference in nitroxide mobility, with higher 2Azz' values representing lower mobility (figure 7.5). Rx binding sites on the β-sheet gave consistently higher 2Azz' values than sites on the α-helix, with no noticeable similarities within β-sheet binding conformations. Spectra measured for α-helical Rx binding sites showed similar 2Azz' values when Rx was bound from i to i+3 (L16-A19Rx) and bound from i to i+4 (L16-K20Rx and A19-E23Rx). The 2Azz' values measured for Rx when bound from i to i+1 (A19-K20Rx and D26-A27Rx) varied more between sites than 2Azz' values measured for Rx bound from i to i+3, and bound from i to i+4. On the β-sheet, 2Azz' values of ~71 G were measured for one site in each different binding conformation (T122-V124Rx for i to i+2; T106-T122Rx for perpendicularly between β-strands; and K87-S104Rx for diagonally

between β-strands). While the other site in each conformation displayed a lower 2Azz' value than this.

7.4.2 α-Helical 2Azz' Values

A comparison between 2Azz' and Tilt angle distributions for α-helical sites showed a relationship between the modality of the Tilt angle distribution and the 2Azz' value. Higher 2Azz' values were measured from sites exhibiting bimodal Tilt distributions (Rx bound from i to i+3 (L16-A19Rx) and from i to i+4 (L16-K20Rx and A19-E23Rx)), than for monomodal Tilt distributions (Rx was bound from i to i+1 (A19-K20Rx and D26-A27Rx)). A greater range of angles within bimodal Tilt distributions (higher 2Azz') was recorded than within monomodal Tilt distributions (lower 2Azz'). However, it was expected the range of angles within the Tilt distribution would decrease as 2Azz' increased due to higher 2Azz' values being indicative of lower mobility. This expectation turned out to be correct within the context of modal widths; the widths of Tilt distributions exhibiting bimodality were narrower than the width of Tilt distributions exhibiting monomodality. Altogether, these suggest transitions of Rx between different modes within a bimodal conformation had a low likelihood of occurring during the experimental time scale. This low likelihood suggested a high-energy barrier between different, with high-energy states located in between. It was hypothesized that buttressing residues forced Rx to adopt these high energy states when bound from i to i+1, resulting in a greater breadth of nitroxide motion and a lower 2Azz' value.

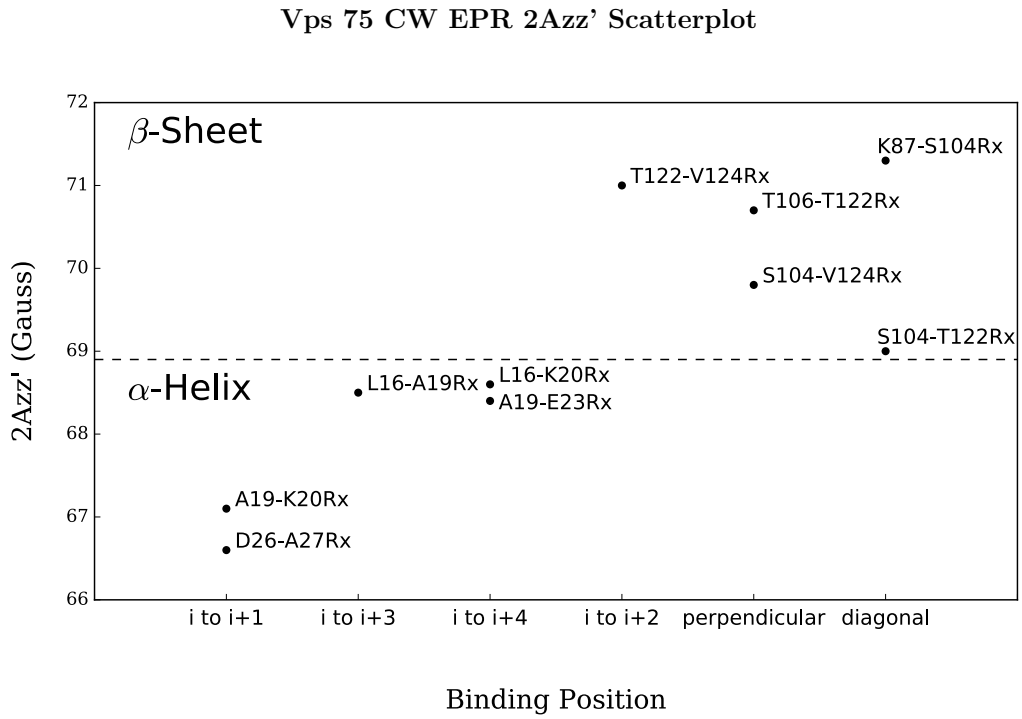

Figure 7.5: A plot of the 2Azz' values against the binding position on the α-helix or β-sheet, the dashed line at 68.9 G marks a divide between 2Azz' values from α-helix sites and β-sheet sites.

7.5 A19-K20Rx as a Model for i to i + 1 mobility

7.5.1 Buttressing Residue Mutations

When Rx was bound from i to i+1 on the α-helix the bimodal Tilt distribution was obfuscated by buttressing amino acid residues. Residues buttressing the i to i+1 Rx binding sites were positioned on adjacent turns towards the C or N terminus of the α-helix. The relationship between the level of obfuscation and bulk of buttressing amino acid residues was investigated by mutating one or both residues buttressing Vps 75 A19-K20Rx to alanine. Vps 75 A19-K20Rx sites were orientated across the dimerization domain in a manner that caused a shift in the experimental distance distribution towards longer or shorter distances to indicate a shift in the Rx

nitroxide ring distribution towards the N or C terminus of the α-helix respectively. Allowing experimental distance distributions to measure the effect of the C and N terminal buttressing residues bulk on the distribution of Rx.

7.5.2 Comparison Between the PELDOR Distance Distributions for Different Buttressing Residue Mutations

Noticeable shifts in distance distributions from wild type buttressing residues were observed for all mutations, the degree of these shifts changed whether the N or C-terminal buttressing residue was reduced in bulk. Reduction in bulk of the N terminal buttressing residue (L16A) produced a slight shift in the distance distribution towards longer distances, and reduction in bulk of the C terminal residue (E23A) caused a more dramatic shift in the distance distribution towards shorter distances. Reducing the bulk of both the C and N terminal buttressing residues caused the modal distance to shift towards shorter ranges than the wild type, with a broadened distance distribution. These observations are all supportive of our model for Rx buttressing and its consequences.

7.5.3 Translated Distances

Different magnitudes of the shift in distance distribution, when the N or C terminal buttressing residue of Vps 75 A19-K20Rx were reduced in bulk, were a consequence of the slant in the Cα to Cβ vector towards the helices N terminus for residues within the α-helix. This created a more expansive gap on the C terminal side of the nitroxide group than the N terminal side, requiring a bulkier amino acid residue to prevent tilting of Rx towards the C terminus. This caused the bulk of the C terminal buttressing residues to have a greater effect on the motion of Rx than the bulk of the N-terminal buttressing residue.

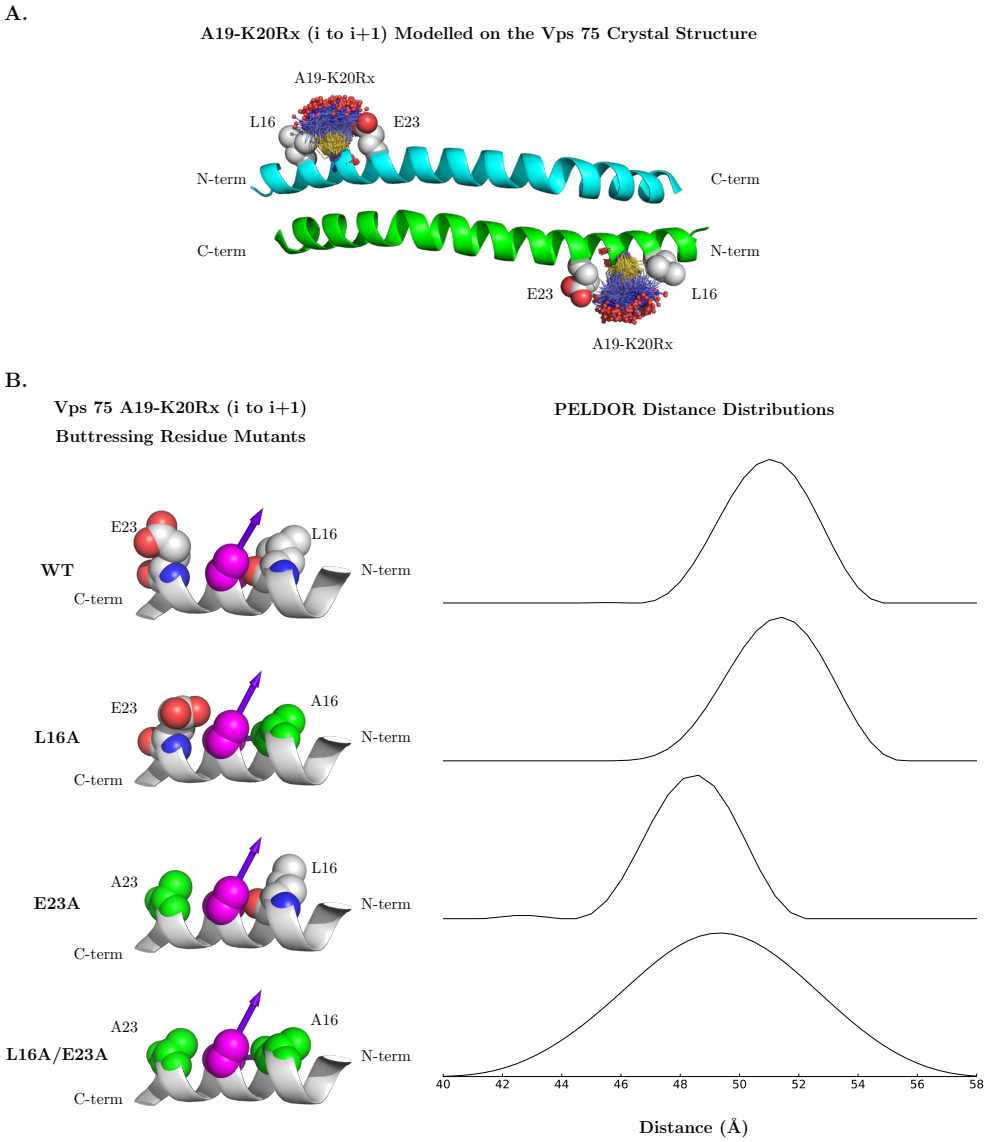

Figure 7.6: Experimental distance distributions of A19-K20Rx constructs with none, one or both buttressing residues mutated to alanine alongside images of the respective buttressing residues. (A) An image of A19-K20Rx modelled onto the Vps 75 dimerization domain with the buttressing residues displayed as grey spheres. Due to the orientation of Rx across the homodimer an increase in the spin labels motion towards the C-terminus would shorten the spin-spin distance; and an increase in motion towards the N terminus would cause distances to lengthen. (B) (left) An image of different buttressing mutations along with the Cα to Cβ vector for A19 and K20 shown in magenta. Wild type buttressing residues are displayed in the same colour as the cartoon backbone and alanine mutations are highlighted in green. (right) Experimental distance distributions from Vps 75 A19-K20Rx with wild type, L16A, E23A, or L16A/E23A buttressing residue mutations.

7.6 Conclusion

7.6.1 The α-Helix is the Most Reliable Secondary Structural feature to Bind Rx for Orientation Selective PELDOR Measurements

The aim of this project was to determine and assess the suitability of Rx binding sites for performing orientation selective PELDOR. Modelled and experimental distance distributions were similar for Rx sites on the α-helix and significantly different when Rx was bound to the β-sheet. The β-sheet is a tertiary structural feature where the sheets plane, defined by the orientation of the protein backbone for each β-strand, is highly dependent on the proteins overall tertiary or quaternary structure. Changes in the β-sheets plane can modify the Rx nitroxide ring distribution with respect to the protein backbone, limiting the ability to predict the location of the protein backbone in relation to the distribution of Rx.

7.6.2 The Nitroxide ring of Rx is in a bimodal distribution when bound to a protein

Previous studies (Fleissner et al., 2011) observed the nitroxide ring from Rx had a bimodal distribution located either side of the binding sites Cα to Cα vector. A bimodal distribution has a greater range of orientations between spin label pairs than a mono modal distribution, lowering the quality of orientation data from bimodal nitroxide ring distributions. Blocking one or both bimodal nitroxide ring distributions using protein structural features caused the nitroxide to adopt a monomodal distribution. This study was aimed at determining a generic Rx binding site, so the most important restrictions to Rx were imposed by residues positioned either side of the Cα to Cα vector of the Rx binding site, referred to as buttressing residues. Differences in the motion of Rx caused by buttressing residues were observable within the Tilt angle distribution measured from molecular dynamics of Rx modelled onto the Vps 75 crystal structure (figures 7.3

and 7.4). Where i to i+1 on the α-helix (A19-K20Rx and D26-A27Rx) was the most reliable site for positioning buttressing residues to interfere with the bimodal Tilt distribution.

7.6.3 β-Sheet Buttressing Residues

Alternating residues on the β-strand are placed with the Cα to Cβ bond pointing out of opposite faces of the β-strand, therefore holes were created in the β-strand at i+/-1 from the binding site. When Rx was bound between i to i+2 and perpendicularly between β-strands these holes align with locations of the bimodal distributions of Rx, preventing surrounding amino acids from blocking the bimodal distribution of Rx in a predictable manner. The most promising β-sheet binding sites were diagonally bound between separate β-strands, allowing residues at i+/-2 from the Rx binding site to buttress the spin label.

7.6.4 α-Helix Buttressing Resides

Buttressing residues on the α-helix all point away from the helical axis. This created holes for the Rx nitroxide ring where buttressing residues are rotated around the helical axis away from the Rx binding conformation. This occurred for Rx bound from i to i+3 or i to i+4 on the α-helix, allowing the nitroxide ring of Rx to adopt a bimodal distribution at these sites. Binding Rx from i to i+1 on the α-helix positioned the i-3 and i+4 residues in locations that buttressed the Rx binding site, forcing the Rx nitroxide ring into a monomodal distribution. In this case the bulk of residues affected the nitroxide distribution differently when buttressing Rx on the C (at i+4) or N (at i-3) terminal side.

7.6.5 Rx Bound Between i and i+1 has its Motion Reduced by Buttressing Amino Acid Residues

To explain the effect of different buttressing residues on the Rx distribution, it first must be considered that the Cα to Cβ bond within α-helices leans towards the N terminus. This presented different C and N terminal gaps for the bimodal nitroxide ring distribution of Rx. As a result, the area available for the nitroxide ring had a smaller volume on the N terminal side of Rx than the C terminal side. This was reflected in experimental distance distributions for Vps 75 A19-K20Rx, where large shift in the modal distance when the C terminal residue was reduced in bulk, and a small change in the modal distance when the N terminal residue was reduced in bulk (figure 7.6). This asymmetry posed the question, which set of buttressing residues provided the most desirable sites for binding Rx between i and i+1? The tightest distance distribution of Rx was produced by ensuring only the C-terminal nitroxide distribution, using a C terminal buttressing residue with a low bulk, and a N-terminal buttressing residue with a large bulk (Vps 75 A19-K20Rx / E23A, figure 7.6 B).

7.7 Prospects

The biggest consideration for choosing a Rx binding site for making orientation selective PELDOR measurements is the presence and bulk of buttressing amino acid residues. Based upon this finding, when the only available structural feature is the β-sheet it was predicted that a mono-modal distribution could be enforced when Rx was bound diagonally between β-strands. Further investigations into the effect of the bulk of β-sheet buttressing residues upon the motion of Rx within a protein with a more reliable β-sheet topology could answer the question of whether it was possible to restrict the nitroxide ring distribution in the same way

as has been shown for the α-helix. Once a suitable model β-sheet could be determined these differences could be examined by first splitting amino acids into groups based upon their bulk, then measuring the effect on the Rx nitroxides distribution based upon the bulk of the buttressing amino acid residues. Such a study would also involve examining how large the effect of different β-sheet topologies upon the motion of Rx bound diagonally between β-strands. In addition, the properties of i to i+1 bound to the α-helix could be expanded by determining the effect of multiple different amino acids on the motion of Rx when positioned at one or both C and N terminal buttressing residues.

Chapter 8: Conclusion

8.0 Summary

Data presented within this thesis highlighted applications of EPR for answering questions posed when solving protein structures. These involved investigation of an intrinsically disordered structural region, and determining the orientation of a dimerization interface. Additionally, improvements to PELDOR sample preparation for solving protein structures have been investigated, showing distance distribution's range and accuracy measured using PELDOR were improved by deuteration of protein samples. Also, the rigid spin label Rx restricts the nitroxide distribution to a level that could allow orientations to be measured between labelled sites, particularly when bound from i to i+1 on the α-helix. The future direction of this work is to improve methods for incorporating PELDOR orientation measurements in structural refinement, and further elucidate underlying relaxation mechanisms within deuterated protein systems.

8.1 Overview

Two aims of this thesis are:

- to demonstrate how EPR can be used to answer questions about protein structures;
- and show improvements to PELDOR by increasing the quantity of information available for solving protein structures.

To demonstrate the use of EPR for solving protein structures, chapter 4 presented CW-EPR and PELDOR data for the N-terminal tail of Endo I, showing the region to be intrinsically ordered when bound to DNA. Chapter 5 presented PELDOR data in

support of the MuRF 1 homodimer's coiled coil domain lying in an anti-parallel conformation.

Increasing the quantity of structural information when using PELDOR has been addressed in a twofold manner. Data presented in chapter 6 showed deuteration of Trim 25 increased the sensitivity of PELDOR measurements by reducing T_2 relaxation. This increased the time span of PELDOR experiments, in turn increasing the range of accessible distances. Secondly, chapter 7 presented data suggesting the bifunctional spin label Rx was rigid enough for making orientation measurements within protein structures using PELDOR. Binding Rx from i to i+1 upon an α-helix presented a monomodal nitroxide distribution, as opposed to the bimodal distribution seen when bound to other conformations. The restriction of the nitroxide ring of Rx to a monomodal distribution is preferable when making and interpreting orientation measurements.

8.2 The N-terminal Tail of Endo I forms an Intrinsically Disordered Structure.

CW-EPR and PELDOR data supported the claim that the intrinsically disordered N-terminal tails of the Endo I homodimer became ordered upon binding the minor groove of a DNA four-way junction. Furthermore, variations in distances across the homodimer and spin label mobility between labelling sites, showed two distinct structural regions within these N-terminal tails. The length of distances measured between residues 10 and 16 of Endo I implied labelling sites were positioned outside the centre of the DNA four-way junction. The variation of distances across the Endo I homodimer for residues between 10 and 16 supported an elongated

protein backbone. Shorter distances between labelling sites enclosed by residues 1 to 10 on Endo I bound to DNA, positioned these residues within the centre of the bound DNA junction. Additionally, changes in mobility between R1 binding sites within this region implied the formation of a helical structure. These two regions reflect data from previous work (Freeman et al., 2013), where truncations within the first 16 residues of Endo I stabilized its binding to the DNA four-way junction, at the cost of activity. Alternatively, deletion of the first 16 N-terminal residues of Endo I showed a decreased binding affinity between Endo I and the DNA four-way junction in comparison to deletion of the first 11 N-terminal residues.

An overall analysis of these data sets led to the hypothesis that residues 1 to 10 of Endo I adopted a helical structure upon binding the DNA four-way junction, responsible for destabilising the junction. While residues 10 to 15 formed an elongated structure that increased the affinity of Endo I to the DNA four-way junction.

8.3 The Coiled Coil Region of MuRF 1 is Anti-Parallel and Conforms to a Trim Coiled Coil Structural Archetype.

Moving the spin labelling site from the N-terminus to the C-terminus of MuRF 1's coiled coil domain gave an arrangement of distances indicating an antiparallel homodimer. The longest distances were observed towards extremities of the coiled coil, the C or N terminus of the structure, with shorter distances observed at sites towards the centre of the coiled coil. The proposed structure of MuRF 1 was similar to coiled coil regions from crystal structures of other Trim family members. Structural similarities between Trim family members and MuRF 1 extended to the C-terminal helices, which folded back towards the centre of the coiled coil domain.

8.4 Deuteration of the Trim 25 Coiled Coil Region Allows PELDOR to be Measured Over Expanded Distances, Revealing Differences Between the Solution and Crystal Structures.

There was no discernible correlation between modal distances for R1 spin-labels bound to the Trim 25 coiled coil domain and the measured T_m. Although no other correlations were observable, for example between the deuteron density and T_m, the variation in T_m strongly suggested that there was an underlying relationship between it and the spin label's protein environment. Additionally, the structure of the Trim 25 coiled coil domain was observed to differ from both crystal structures deposited in the protein data bank. Differences observed in modelled distance distributions between the two crystal structures, as well as the change in distance distributions derived by PELDOR, implied crystal packing forces were able to change the coiling of the coiled coil domain. Differences in coiling were facilitated by the width of the hydrophobic pocket produced by K284 and K285 within the coiled coil domain of Trim 25, and the relatively small size of the opposing hydrophobic residue (A216).

8.5 The Binding of Rx from i to i+1 on the α–Helix Presents a Generic Spin Label Site for use in Orientation Measurements.

A consistent, predictable and translatable generic labelling site for use in PELDOR orientation measurements was produced when Rx was bound from i to i+1 on the α-helix. Analysis of the motion of Rx showed when the Rx label was sterically limited (buttressed) by large amino acid side chains situated on either side of the spin-label, the nitroxide from Rx was in a monomodal distribution. This mono-modal distribution enables orientation measurements to be performed upon Rx bound to i to i+1. The limited number of conformations Rx could adopt at this

binding site would simplify the translation of PELDOR orientation measurements to structural data for the protein backbone. Other positions of attachment that lacked buttressing residues displayed a bimodal distribution, making orientation analysis more difficult. In conclusion, a generic Rx labelling site for potentially making orientation measurements within protein structures has been found, and considerations of the surrounding amino acid sequence that should be made when choosing the labelling site were investigated.

8.6 Conclusions and Prospects.

PELDOR provides information that is most effectively used for combining and clarifying structural data from a series of different techniques. The quality of PELDOR data and interpretation of distance measurements is vital for its correct use within structural biology. In this regard, the significance of DeerAnalysis in combination with MTSL wizard and MMM is hard to overstate. To expand the use of the technique, the ability to give simple answers to the question of what PELDOR can and cannot say regarding protein structures is critical.

Deuteration has expanded the distance range that can be achieved by increasing the T_m of the sample, however the possible extent of this increase is not fully understood. Data in both this thesis and recent studies (Schmidt et al., 2016) gives a possible maximum T_m value of approximately 30 µs. This allows PELDOR experiments to be run over 60 to 80 µs, giving maximum measurable modal distances of around 140 Å to 160 Å.

However, questions remain on what aspects of the underlying protein structure are limiting the T_m, and whether the stated values are the limits to the modal

distance that can be measured using PELDOR within protein structures. A rough idea of whether the value stated (30 μs) is the maximum possible T_m values for labelled protein structures, could be investigated by measuring the T_m of 4'-amino TEMPO at increasing concentrations until the mean spin-spin distance is within the range of distances found within a protein structure (15-150 Å). This would produce a rough estimate for the limit of T_m within a protein system. In addition, the observed variation of T_m from Trim 25 labelled with R1 suggested an impact from the local underlying protein structure. This effect can be investigated on a macro scale by exploring differences in relaxation when a solvent exposed spin label is introduced onto different protein folds. Additionally, it can be investigated on a micro scale by modifying specific amino acids within the protein. The aim of future studies would be to determine the limit of distances that can be measured using PELDOR, and investigated the use of EPR as a means to probe the underlying protein structure. Knowledge of the full capability of PELDOR is valuable when considering its use in studying protein structures. A clear example of this requirement would be the use of long-range PELDOR measurements upon full-length constructs of MuRF 1. These measurements would allow locations of domains across the elongated coiled coil scaffolding domain to be determined, and to investigate structural-functional relationships for MuRF 1.

The use of orientation data from EPR for structural refinement would be a valuable tool in structural biology. The current study showed orientation measurements on Rx bound from i to i+1 on the α-helix of Vps 75 gave an angle distribution with its modal angle aligning with that from the modelled distribution of Rx (Stevens et al., 2016). The next stage in advancing the use of orientation measurements in structural biology is to develop methodologies for implementing them in protein

structural refinement. Initially this would involve using rigid body refinement to determine how accurately the Vps 75 dimer can be refined from Vps 75 monomers using the distances and orientations available. In doing this the number of distances and angles that are required to produce the structure would be determined, tested and refined. In addition, to increase the usefulness of Rx in refining protein structures the modelled distribution of the label would be made more accurate; and a method to simply model the label's distribution onto protein structures would be developed.

It would be of interest to use Rx upon the coiled coil region of Trim 25 to allow measurements of changes in coiling between the crystal and glass phase structures. This would enabling methodologies for refinement using orientation measurements to be tested in a potentially biologically relevant study. In a similar manner, it would be of interest to develop a methodology for using the limited information available from intrinsically disordered regions within protein structure refinement.

The research presented here has produced valuable insights into the structure of Trim proteins and provided a starting point for the further investigation of Trim protein structures. Further investigations would use orientation measurements, and deuteration of the underlying protein structure. Orientation measurements allow a greater amount of structural data to be determined using fewer constructs, and deuteration allows structural data to be gathered over greater distances. Both these facets are important in studying the elongated Trim family of proteins, with the investigation of Trim 25 highlighting the importance of understanding the

orientations of separate helices within coiled coil domains with respect to one another.

The canonical Trim protein structure involved an elongated anti-parallel coiled coil which separated the other structural domains by long distances. This highlights the importance of measuring long distance ranges within protein structures. Further expansion of this work could be carried out using protein deuteration to determine domain positions within full-length protein structures of Trim 25 and MuRF 1. The primary focus for all these investigations would be to develop methods for implementing orientation data into structural refinement, and pushing the limit of distances PELDOR can measure.

References:

Abdullin, D., Hagelueken, G., Hunter, R.I., Smith, G.M., and Schiemann, O. (2015). Geometric model-based fitting algorithm for orientation-selective PELDOR data. Mol. Phys. *113*, 544–560.

Adams, V., Mangner, N., Gasch, A., Krohne, C., Gielen, S., Hirner, S., Thierse, H.-J., Witt, C.C., Linke, A., Schuler, G., et al. (2008). Induction of MuRF1 Is Essential for TNF-α-Induced Loss of Muscle Function in Mice. J. Mol. Biol. *384*, 48–59.

Alexander, N., Al-Mestarihi, A., Bortolus, M., Mchaourab, H., and Meiler, J. (2008). De Novo High-Resolution Protein Structure Determination from Sparse Spin-Labeling EPR Data. Structure *16*, 181–195.

Altenbach, C., Flitsch, S.L., Gobind Khorana, H., and Hubbell, W.L. (1989). Structural Studies on Transmembrane Proteins. 2. Spin Labeling of Bacteriorhodopsin Mutants at Unique Cysteines. Biochemistry (Mosc.) *28*, 7806–7812.

Back, J.W., de Jong, L., Muijsers, A.O., and de Koster, C.G. (2003). Chemical Cross-Linking and Mass Spectrometry for Protein Structural Modeling. J. Mol. Biol. *331*, 303–313.

Bagguley, D.M.S., and Griffiths, J.H.E. (1947). Paramagnetic Resonance and Magnetic Energy Levels in Chrome Alum. Nature *160*, 532–533.

Bagnéris, C., Rogala, K.B., Baratchian, M., Zamfir, V., Kunze, M.B.A., Dagless, S., Pirker, K.F., Collins, M.K., Hall, B.A., Barrett, T.E., et al. (2015). Probing the Solution Structure of IκB Kinase (IKK) Subunit γ and Its Interaction with Kaposi Sarcoma-associated Herpes Virus Flice-interacting Protein and IKK Subunit β by EPR Spectroscopy. J. Biol. Chem. *290*, 16539–16549.

Bagryanskaya, E.G., Polovyanenko, D.N., Fedin, M.V., Kulik, L., Schnegg, A., Savitsky, A., Möbius, K., Coleman, A.W., Ananchenko, G.S., and Ripmeester, J.A. (2009). Multifrequency EPR Study of the Mobility of Nitroxides in Solid-State Calixarene Nanocapsules. Phys. Chem. Chem. Phys. *11*, 6700–6707.

Bai, X., Yan, C., Yang, G., Lu, P., Ma, D., Sun, L., Zhou, R., Scheres, S.H.W., and Shi, Y. (2015). An Atomic Structure of Human γ-Secretase. Nature *525*, 212–217.

Bartesaghi, A., Matthies, D., Banerjee, S., Merk, A., and Subramaniam, S. (2014). Structure of β-galactosidase at 3.2-Å resolution obtained by cryo-electron microscopy. Proc. Natl. Acad. Sci. *111*, 11709–11714.

Becker, E.D. (1993). A Brief History of Nuclear Magnetic Resonance. Anal. Chem. *65*, 295A–302A.

Becker, C.F.W., Lausecker, K., Balog, M., Kálai, T., Hideg, K., Steinhoff, H.-J., and Engelhard, M. (2005). Incorporation of Spin-Labelled Amino Acids into Proteins. Magn. Reson. Chem. *43*, S34–S39.

Belle, V., Rouger, S., Costanzo, S., Liquière, E., Strancar, J., Guigliarelli, B., Fournel, A., and Longhi, S. (2008). Mapping Alpha-Helical Induced Folding Within the Intrinsically Disordered C-Terminal Domain of the Measles Virus Nucleoprotein by Site-Directed Spin-Labeling EPR Spectroscopy. Proteins *73*, 973–988.

Benial, A.M.F., Dhas, M.K., and Jawahar, A. (2011). Rotational Correlation Time Studies on Nitroxyl Radicals Using 300 MHz ESR Spectrometer in High Viscous Liquid. Appl. Magn. Reson. *40*, 311.

van den Berg, S., Löfdahl, P.-Å., Härd, T., and Berglund, H. (2006). Improved Solubility of TEV Protease by Directed Evolution. J. Biotechnol. *121*, 291–298.

Berliner, L.J. (2012). History of the Use of Nitroxides (Aminoxyl Radicals) in Biochemistry: Past, Present and Future of Spin Label and Probe Method. In Nitroxides - Theory, Experiment and Applications, (Chapter 1), pp. 3–24.

Berliner, L.J., Grunwald, J., Hankovszky, H.O., and Hideg, K. (1982). A novel reversible thiol-specific spin label: Papain active site labeling and inhibition. Anal. Biochem. *119*, 450–455.

Berman, H., Henrick, K., Nakamura, H., and Markley, J.L. (2007). The Worldwide Protein Data Bank (wwPDB): Ensuring a Single, Uniform Archive of PDB Data. Nucleic Acids Res. *35*, D301–D303.

Berman, H.M., Kleywegt, G.J., Nakamura, H., and Markley, J.L. (2014). The Protein Data Bank Archive as an Open Data Resource. J. Comput. Aided Mol. Des. *28*, 1009–1014.

Berndsen, C.E., Tsubota, T., Lindner, S.E., Lee, S., Holton, J.M., Kaufman, P.D., Keck, J.L., and Denu, J.M. (2008). Molecular Functions of the Histone Acetyltransferase Chaperone Complex Rtt109-Vps75. Nat. Struct. Mol. Biol. *15*, 948–956.

Biertümpfel, C., Yang, W., and Suck, D. (2007). Crystal Structure of T4 Endonuclease VII Resolving a Holliday Junction. Nature *449*, 616–620.

Bloch, F. (1946). Nuclear Induction. Phys. Rev. *70*, 460–474.

Bloch, F., Hansen, W.W., and Packard, M. (1946). The Nuclear Induction Experiment. Phys. Rev. *70*, 127.

Blume, R.J. (1958). Electron Spin Relaxation Times in Sodium-Ammonia Solutions. Phys. Rev. *109*, 1867–1873.

Bodine, S.C., and Baehr, L.M. (2014). Skeletal Muscle Atrophy and the E3 Ubiquitin Ligases MuRF1 and MAFbx/atrogin-1. Am. J. Physiol. - Endocrinol. Metab. *307*, E469–E484.

Bodine, S.C., Latres, E., Baumhueter, S., Lai, V.K.-M., Nunez, L., Clarke, B.A., Poueymirou, W.T., Panaro, F.J., Na, E., Dharmarajan, K., et al. (2001). Identification of Ubiquitin Ligases Required for Skeletal Muscle Atrophy. Science *294*, 1704–1708.

Borbat, P.P., Costa-Filho, A.J., Earle, K.A., Moscicki, J.K., and Freed, J.H. (2001). Electron Spin Resonance in Studies of Membranes and Proteins. Science *291*, 266–269.

Bowman, A., Hammond, C.M., Stirling, A., Ward, R., Shang, W., El-Mkami, H., Robinson, D.A., Svergun, D.I., Norman, D.G., and Owen-Hughes, T. (2014). The

Histone Chaperones Vps75 and Nap1 form Ring-Like, Tetrameric Structures in Solution. Nucleic Acids Res. *42*, 6038–6051.

Breitgoff, F.D., Polyhach, Y.O., and Jeschke, G. (2017). Reliable Nanometre-Range Distance Distributions from 5-Pulse Double Electron Electron Resonance. Phys. Chem. Chem. Phys. *19*, 15754–15765.

Bruni, F., and Leopold, A.C. (1991). Glass Transitions in Soybean Seed 1. Plant Physiol. *96*, 660–663.

Burkhard, P., Stetefeld, J., and Strelkov, S.V. (2001). Coiled coils: a Highly Versatile Protein Folding Motif. Trends Cell Biol. *11*, 82–88.

Burr, M., and Koshland, D.E. (1964). Use of ``Reporter Groups'' in Structure-Function Studies of Proteins. Proc. Natl. Acad. Sci. U. S. A. *52*, 1017–1024.

Bystranowska, D., Siejda, B., Ożyhar, A., and Kochman, M. (2012). The Dityrosine Cross-Link as an Intrinsic Donor For Assembling FRET Pairs in the Study of Protein Structure. Biophys. Chem. *170*, 1–8.

Carthagena, L., Bergamaschi, A., Luna, J.M., David, A., Uchil, P.D., Margottin-Goguet, F., Mothes, W., Hazan, U., Transy, C., Pancino, G., et al. (2009). Human TRIM Gene Expression in Response to Interferons. PLOS ONE *4*, e4894.

Castanier, C., Zemirli, N., Portier, A., Garcin, D., Bidère, N., Vazquez, A., and Arnoult, D. (2012). MAVS Ubiquitination by the E3 Ligase TRIM25 and Degradation by the Proteasome is Involved in Type I Interferon Production After Activation of the Antiviral RIG-I-like Receptors. BMC Biol. *10*, 44.

Cavalli, A., Salvatella, X., Dobson, C.M., and Vendruscolo, M. (2007). Protein Structure Determination from NMR Chemical Shifts. Proc. Natl. Acad. Sci. *104*, 9615–9620.

Centner, T., Yano, J., Kimura, E., McElhinny, A.S., Pelin, K., Witt, C.C., Bang, M.-L., Trombitas, K., Granzier, H., Gregorio, C.C., et al. (2001). Identification of Muscle Specific Ring Finger Proteins as Potential Regulators of the Titin Kinase Domain. J. Mol. Biol. *306*, 717–726.

Chu, F., Shan, S., Moustakas, D.T., Alber, F., Egea, P.F., Stroud, R.M., Walter, P., and Burlingame, A.L. (2004). Unraveling the Interface of Signal Recognition Particle and its Receptor by Using Chemical Cross-Linking and Tandem Mass Spectrometry. Proc. Natl. Acad. Sci. U. S. A. *101*, 16454–16459.

Clarke, B.A., Drujan, D., Willis, M.S., Murphy, L.O., Corpina, R.A., Burova, E., Rakhilin, S.V., Stitt, T.N., Patterson, C., Latres, E., et al. (2007). The E3 Ligase MuRF1 Degrades Myosin Heavy Chain Protein in Dexamethasone-Treated Skeletal Muscle. Cell Metab. *6*, 376–385.

Collins, N.C., Thordal-Christensen, H., Lipka, V., Bau, S., Kombrink, E., Qiu, J.-L., Hückelhoven, R., Stein, M., Freialdenhoven, A., Somerville, S.C., et al. (2003). SNARE-Protein-Mediated Disease Resistance at the Plant Cell Wall. Nature *425*, 973–977.

Commoner, B., Townsend, J., and Pake, G.E. (1954). Free Radicals in Biological Materials. Nature *174*, 689–691.

Cowieson, N.P., Kobe, B., and Martin, J.L. (2008). United We Stand: Combining Structural Methods. Carbohydr. Glycoconj. Biophys. Methods *18*, 617–622.

Crick, F. (1953). The Packing of Alpha-Helices: Simple Coiled-Coils. Acta Crystallogr. *6*, 689–697.

Cruickshank, P.A.S., Bolton, D.R., Robertson, D.A., Hunter, R.I., Wylde, R.J., and Smith, G.M. (2009). A Kilowatt Pulsed 94 GHz Electron Paramagnetic Resonance Spectrometer With High Concentration Sensitivity, High Instantaneous Bandwidth, and Low Dead Time. Rev. Sci. Instrum. *80*, 103102.

Cunningham, T.F., Putterman, M.R., Desai, A., Horne, W.S., and Saxena, S. (2015). The Double-Histidine Cu2+-Binding Motif: A Highly Rigid, Site-Specific Spin Probe for Electron Spin Resonance Distance Measurements. Angew. Chem. Int. Ed. *54*, 6330–6334.

D'Arcy, S., and Luger, K. (2011). Understanding histone acetyltransferase Rtt109 structure and function: how many chaperones does it take? Curr. Opin. Struct. Biol. *21*, 728–734.

Davis, M.E., and Gack, M.U. (2015). Ubiquitination in the Antiviral Immune Response. 60th Anniv. Issue *479*, 52–65.

D'Cruz, A.A., Kershaw, N.J., Chiang, J.J., Wang, M.K., Nicola, N.A., Babon, J.J., Gack, M.U., and Nicholson, S.E. (2013). Crystal Structure of the TRIM25 B30.2 (PRYSPRY) Domain: a Key Component of Antiviral Signalling. Biochem. J. *456*, 231–240.

Déclais, A., Fogg, J.M., Freeman, A.D.J., Coste, F., Hadden, J.M., Phillips, S.E.V., and Lilley, D.M.J. (2003). The Complex Between a Four-Way DNA Junction and T7 Endonuclease I. EMBO J. *22*, 1398.

Déclais, A.-C., Liu, J., Freeman, A.D.J., and Lilley, D.M.J. (2006). Structural Recognition Between a Four-way DNA Junction and a Resolving Enzyme. J. Mol. Biol. *359*, 1261–1276.

Denysenkov, V.P., Prisner, T.F., Stubbe, J., and Bennati, M. (2006). High-Field Pulsed Electron–Electron Double Resonance Spectroscopy to Determine the Orientation of the Tyrosyl Radicals in Ribonucleotide Reductase. Proc. Natl. Acad. Sci. *103*, 13386–13390.

DeSensi, S.C., Rangel, D.P., Beth, A.H., Lybrand, T.P., and Hustedt, E.J. (2008). Simulation of Nitroxide Electron Paramagnetic Resonance Spectra from Brownian Trajectories and Molecular Dynamics Simulations. Biophys. J. *94*, 3798–3809.

Doll, A., Pribitzer, S., Tschaggelar, R., and Jeschke, G. (2013). Adiabatic and Fast Passage Ultra-Wideband Inversion in Pulsed EPR. J. Magn. Reson. *230*, 27–39.

Doll, A., Qi, M., Wili, N., Pribitzer, S., Godt, A., and Jeschke, G. (2015). Gd(III)–Gd(III) Distance Measurements With Chirp Pump Pulses. J. Magn. Reson. *259*, 153–162.

Driscoll, R., Hudson, A., and Jackson, S.P. (2007). Yeast Rtt109 Promotes Genome Stability by Acetylating Histone H3 on Lysine 56. Science *315*, 649–652.

Du, J.L., Eaton, G.R., and Eaton, S.S. (1995). Temperature, Orientation, and Solvent Dependence of Electron Spin-Lattice Relaxation Rates for Nitroxyl Radicals in Glassy Solvents and Doped Solids. J. Magn. Reson. A *115*, 213–221.

El Mkami, H., Ward, R., Bowman, A., Owen-Hughes, T., and Norman, D.G. (2014). The Spatial Effect of Protein Deuteration on Nitroxide Spin-Label Relaxation: Implications for EPR Distance Measurement. J. Magn. Reson. *248*, 36–41.

Esposito, D., Koliopoulos, M.G., and Rittinger, K. (2017). Structural Determinants of TRIM Protein Function. Biochem. Soc. Trans. *45*, 183.

Fernandez-Leiro, R., and Scheres, S.H.W. (2016). Unravelling Biological Macromolecules With Cryo-Electron Microscopy. Nature *537*, 339–346.

Fielding, A.J., Concilio, M.G., Heaven, G., and Hollas, M.A. (2014). New Developments in Spin Labels for Pulsed Dipolar EPR. Molecules *19*, 16998–17025.

Fillingham, J., Recht, J., Silva, A.C., Suter, B., Emili, A., Stagljar, I., Krogan, N.J., Allis, C.D., Keogh, M.-C., and Greenblatt, J.F. (2008). Chaperone Control of the Activity and Specificity of the Histone H3 Acetyltransferase Rtt109. Mol. Cell. Biol. *28*, 4342–4353.

Fleissner, M.R., Brustad, E.M., Kálai, T., Altenbach, C., Cascio, D., Peters, F.B., Hideg, K., Peuker, S., Schultz, P.G., and Hubbell, W.L. (2009). Site-directed Spin Labeling of a Genetically Encoded Unnatural Amino Acid. Proc. Natl. Acad. Sci. U. S. A. *106*, 21637–21642.

Fleissner, M.R., Bridges, M.D., Brooks, E.K., Cascio, D., Kálai, T., Hideg, K., and Hubbell, W.L. (2011). Structure and Dynamics of a Conformationally Constrained Nitroxide Side Chain and Applications in EPR Spectroscopy. Proc. Natl. Acad. Sci. *108*, 16241–16246.

Franke, B., Gasch, A., Rodriguez, D., Chami, M., Khan, M.M., Rudolf, R., Bibby, J., Hanashima, A., Bogomolovas, J., Castelmur, E. von, et al. (2014). Molecular Basis for the Fold Organization and Sarcomeric Targeting of the Muscle Atrogin MuRF1. Open Biol. *4*, 130172.

Franklin, R.E., and Gosling, R.G. (1953). The Structure of Sodium Thymonucleate Fibres. I. The Influence of Water Content. Acta Crystallogr. *6*, 673–677.

Freeman, A.D.., Déclais, A.-C., and Lilley, D.M.. (2003). Metal Ion Binding in the Active Site of the Junction-resolving Enzyme T7 Endonuclease I in the Presence and in the Absence of DNA. J. Mol. Biol. *333*, 59–73.

Freeman, A.D.J., Ward, R., El Mkami, H., Lilley, D.M.J., and Norman, D.G. (2011). Analysis of Conformational Changes in the DNA Junction-Resolving Enzyme T7 Endonuclease I on Binding a Four-Way Junction Using EPR. Biochemistry (Mosc.) *50*, 9963–9972.

Freeman, A.D.J., Déclais, A.-C., and Lilley, D.M.J. (2013). The Importance of the N-Terminus of T7 Endonuclease I in the Interaction with DNA Junctions. J. Mol. Biol. *425*, 395–410.

Freeman, A.D.J., Stevens, M., Declais, A.-C., Leahy, A., Mackay, K., El Mkami, H., Lilley, D.M.J., and Norman, D.G. (2016). Analysis of the Intrinsically Disordered N-Terminus of the DNA Junction-Resolving Enzyme T7 Endonuclease I: Identification of Structure Formed upon DNA Binding. Biochemistry (Mosc.) *55*, 4166–4172.

Freemont, P.S. (1993). The RING Finger. Ann. N. Y. Acad. Sci. *684*, 174–192.

Gack, M.U., Shin, Y.C., Joo, C.-H., Urano, T., Liang, C., Sun, L., Takeuchi, O., Akira, S., Chen, Z., Inoue, S., et al. (2007). TRIM25 RING-Finger E3 Ubiquitin Ligase is Essential for RIG-I-Mediated Antiviral Activity. Nature *446*, 916–920.

Gack, M.U., Albrecht, R.A., Urano, T., Inn, K.-S., Huang, I.-C., Carnero, E., Farzan, M., Inoue, S., Jung, J.U., and García-Sastre, A. (2009). Influenza A Virus NS1 Targets the Ubiquitin Ligase TRIM25 to Evade Recognition by the Host Viral RNA Sensor RIG-I. Cell Host Microbe *5*, 439–449.

Gasteiger, E., Hoogland, C., Gattiker, A., Duvaud, S., Wilkins, M.R., Appel, R.D., and Bairoch, A. (2005). Protein Identification and Analysis Tools on the ExPASy Server. In The Proteomics Protocols Handbook, (Humana Press), pp. 571–607.

Gelis, I., Vitzthum, V., Dhimole, N., Caporini, M.A., Schedlbauer, A., Carnevale, D., Connell, S.R., Fucini, P., and Bodenhausen, G. (2013). Solid-State NMR Enhanced by Dynamic Nuclear Polarization as a Novel Tool for Ribosome Structural Biology. J. Biomol. NMR *56*, 85–93.

Gerlach, W., and Stern, O. (1922a). Das magnetische Moment des Silberatoms. Z. Für Phys. *9*, 353–355.

Gerlach, W., and Stern, O. (1922b). Der experimentelle Nachweis der Richtungsquantelung im Magnetfeld. Z. Für Phys. *9*, 349–352.

Gerlach, W., and Stern, O. (1922c). Der experimentelle Nachweis des magnetischen Moments des Silberatoms. Z. Für Phys. *8*, 110–111.

Ghimire, H., McCarrick, R.M., Budil, D.E., and Lorigan, G.A. (2009). Significantly Improved Sensitivity of Q-Band PELDOR/DEER Experiments Relative to X-Band Is Observed in Measuring the Intercoil Distance of a Leucine Zipper Motif Peptide (GCN4-LZ). Biochemistry (Mosc.) *48*, 5782–5784.

Giannoulis, A., Ward, R., Branigan, E., Naismith, J.H., and Bode, B.E. (2013). PELDOR in Rotationally Symmetric Homo-Oligomers. Mol. Phys. *111*, 2845–2854.

Giannoulis, A., Oranges, M., and Bode, B.E. (2017). Monitoring Complex Formation by Relaxation-Induced Pulse Electron Paramagnetic Resonance Distance Measurements. ChemPhysChem *18*, 2318–2321.

Glass, D.J. (2005). Skeletal Muscle Hypertrophy and Atrophy Signaling Pathways. Muscle Wasting Mol. Regul. Nov. Ther. *37*, 1974–1984.

Goldfarb, D. (2012). Metal-Based Spin Labeling for Distance Determination. In Structural Information from Spin-Labels and Intrinsic Paramagnetic Centres in the Biosciences, (Springer, Berlin, Heidelberg), pp. 163–204.

Goldstone, D.C., Walker, P.A., Calder, L.J., Coombs, P.J., Kirkpatrick, J., Ball, N.J., Hilditch, L., Yap, M.W., Rosenthal, P.B., Stoye, J.P., et al. (2014). Structural Studies of Postentry Restriction Factors Reveal Antiparallel Dimers That Enable Avid Binding to the HIV-1 Capsid Lattice. Proc. Natl. Acad. Sci. *111*, 9609–9614.

Gonzalez, A., Cordomí, A., Caltabiano, G., and Pardo, L. (2012). Impact of Helix Irregularities on Sequence Alignment and Homology Modeling of G Protein-Coupled Receptors. ChemBioChem *13*, 1393–1399.

Gorasia, D.G., Veith, P.D., Hanssen, E.G., Glew, M.D., Sato, K., Yukitake, H., Nakayama, K., and Reynolds, E.C. (2016). Structural Insights into the PorK and PorN Components of the Porphyromonas Gingivalis Type IX Secretion System. PLOS Pathog. *12*, e1005820.

Gordy, W., Ard, W.B., and Shields, H. (1955). Microwave Spectroscophy of Biological Substances. I. Paramagnetic Resonance in X-Irradiated Amino Acids and Proteins. Proc. Natl. Acad. Sci. *41*, 983–996.

Górecka, K.M., Komorowska, W., and Nowotny, M. (2013). Crystal Structure of RuvC Resolvase in Complex with Holliday Junction Substrate. Nucleic Acids Res. *41*, 9945–9955.

Greife, A., Felekyan, S., Ma, Q., Gertzen, C.G.W., Spomer, L., Dimura, M., Peulen, T.O., Wöhler, C., Häussinger, D., Gohlke, H., et al. (2016). Structural Assemblies of the Di- and Oligomeric G-Protein Coupled Receptor TGR5 in Live Cells: an MFIS-FRET and Integrative Modelling Study. Sci. Rep. *6*, srep36792.

Grijalba, M.T., Vercesi, A.E., and Schreier, S. (1999). Ca2+-Induced Increased Lipid Packing and Domain Formation in Submitochondrial Particles. A Possible Early Step in the Mechanism of Ca2+-Stimulated Generation of Reactive Oxygen Species by the Respiratory Chain. Biochemistry (Mosc.) *38*, 13279–13287.

Grütter, M.G., and Luban, J. (2012). TRIM5 Structure, HIV-1 Capsid Recognition, and Innate Immune Signaling. Virus Struct. Funct. Emerg. Viruses *2*, 142–150.

Gumucio, J.P., and Mendias, C.L. (2013). Atrogin-1, MuRF-1, and Sarcopenia. Endocrine *43*, 12–21.

Guo, Z., Cascio, D., Hideg, K., and Hubbell, W.L. (2008). Structural Determinants of Nitroxide Motion in Spin-Labeled Proteins: Solvent-Exposed Sites in Helix B of T4 Lysozyme. Protein Sci. *17*, 228–239.

Hadden, J.M., Convery, M.A., Déclais, A.-C., Lilley, D.M.J., and Phillips, S.E.V. (2001). Crystal Structure of the Holliday Junction Resolving Enzyme T7 Endonuclease I. Nat. Struct. Mol. Biol. *8*, 62–67.

Hadden, J.M., Déclais, A., Phillips, S.E.V., and Lilley, D.M.J. (2002). Metal Ions Bound at the Active Site of the Junction-Resolving Enzyme T7 Endonuclease I. EMBO J. *21*, 3505.

Hadden, J.M., Declais, A.-C., Carr, S.B., Lilley, D.M.J., and Phillips, S.E.V. (2007). The Structural Basis of Holliday Junction Resolution by T7 Endonuclease I. Nature *449*, 621–624.

Hadley, C., and Jones, D.T. (1999). A Systematic Comparison of Protein Structure Classifications: SCOP, CATH and FSSP. Structure *7*, 1099–1112.

Hagelueken, G., Ward, R., Naismith, J.H., and Schiemann, O. (2012). MtsslWizard: In Silico Spin-Labeling and Generation of Distance Distributions in PyMOL. Appl. Magn. Reson. *42*, 377–391.

Hammond, C.M., Owen-Hughes, T., and Norman, D.G. (2014). Modelling multi-protein complexes using PELDOR distance measurements for rigid body minimisation experiments using XPLOR-NIH. Methods San Diego Calif *70*, 139–153.

Hammond, C.M., Sundaramoorthy, R., Larance, M., Lamond, A., Stevens, M.A., El-Mkami, H., Norman, D.G., and Owen-Hughes, T. (2016). The Histone Chaperone Vps75 forms Multiple Oligomeric Assemblies Capable of Mediating Exchange Between Histone H3–H4 Tetramers and Asf1–H3–H4 Complexes. Nucleic Acids Res. *44*, 6157–6172.

Helliwell, J.R. (1984). Synchrotron X-radiation protein crystallography: instrumentation, methods and applications. Rep. Prog. Phys. *47*, 1403–1497.

Haugland, M.M., Anderson, E.A., and Lovett, J.E. (2016). Tuning the Properties of Nitroxide Spin Labels for use in Electron Paramagnetic Resonance Spectroscopy Through Chemical Modification of the Nitroxide Framework. In Electron Paramagnetic Resonance, pp. 1–34.

Hirst, S.J., Alexander, N., Mchaourab, H.S., and Meiler, J. (2011). RosettaEPR: An Integrated Tool for Protein Structure Determination from Sparse EPR Data. J. Struct. Biol. *173*, 506–514.

Holm, L., and Sander, C. (1994). The FSSP Database of Structurally Aligned Protein Fold Families. Nucleic Acids Res. *22*, 3600–3609.

Holm, L., and Sander, C. (1996). Mapping the Protein Universe. Science *273*, 595–602.

Hubbell, W.L., Mchaourab, H.S., Altenbach, C., and Lietzow, M.A. (1996). Watching Proteins Move Using Site-Directed Spin Labeling. Structure *4*, 779–783.

Hubbell, W.L., López, C.J., Altenbach, C., and Yang, Z. (2013). Technological advances in site-directed spin labeling of proteins. Protein-Carbohydr. Interact. Biophys. Methods *23*, 725–733.

Huber, M. (2009). Introduction to magnetic resonance methods in photosynthesis. Photosynth. Res. *102*, 305–310.

Inoue, H., Nojima, H., and Okayama, H. (1990). High efficiency transformation of Escherichia coli with plasmids. Gene *96*, 23–28.

Ishimi, Y., Kojima, M., Yamada, M., and Hanaoka, F. (1987). Binding Mode of Nucleosome-Assembly Protein (AP-I) and Histones. Eur. J. Biochem. *162*, 19–24.

Islam, S.M., Stein, R.A., Mchaourab, H.S., and Roux, B. (2013). Structural Refinement from Restrained-Ensemble Simulations Based on EPR/DEER Data: Application to T4 Lysozyme. J. Phys. Chem. B *117*, 4740–4754.

Jagtap, A.P., Krstic, I., Kunjir, N.C., Hänsel, R., Prisner, T.F., and Sigurdsson, S.T. (2015). Sterically shielded spin labels for in-cell EPR spectroscopy: Analysis of stability in reducing environment. Free Radic. Res. *49*, 78–85.

James, L.C., Keeble, A.H., Khan, Z., Rhodes, D.A., and Trowsdale, J. (2007). Structural Basis for PRYSPRY-Mediated Tripartite Motif (TRIM) Protein Function. Proc. Natl. Acad. Sci. *104*, 6200–6205.

Jeschke, G. (2002). Distance Measurements in the Nanometer Range by Pulse EPR. ChemPhysChem *3*, 927–932.

Jeschke, G. (2013). Conformational Dynamics and Distribution of Nitroxide Spin Labels. Prog. Nucl. Magn. Reson. Spectrosc. *72*, 42–60.

Jeschke, G. MMM: A Toolbox for Integrative Structure Modelling. Protein Sci.

Jeschke, G., and Polyhach, Y. (2007). Distance Measurements on Spin-Labelled Biomacromolecules by Pulsed Electron Paramagnetic Resonance. Phys. Chem. Chem. Phys. *9*, 1895–1910.

Jeschke, G., Chechik, V., Ionita, P., Godt, A., Zimmermann, H., Banham, J., Timmel, C.R., Hilger, D., and Jung, H. (2006). DeerAnalysis2006—a Comprehensive Software Package for Analyzing Pulsed ELDOR Data. Appl. Magn. Reson. *30*, 473–498.

Junk, M.J.N. (2012). Electron Paramagnetic Resonance Theory. In Assessing the Functional Structure of Molecular Transporters by EPR Spectroscopy, M. J.N.Junk, ed. (Berlin, Heidelberg: Springer Berlin Heidelberg), pp. 7–52.

Kalisman, N., Adams, C.M., and Levitt, M. (2012). Subunit order of eukaryotic TRiC/CCT chaperonin by cross-linking, mass spectrometry, and combinatorial homology modeling. Proc. Natl. Acad. Sci. *109*, 2884–2889.

Kaminker, I., Tkach, I., Manukovsky, N., Huber, T., Yagi, H., Otting, G., Bennati, M., and Goldfarb, D. (2013). W-Band Orientation Selective DEER Measurements on a Gd3+/Nitroxide Mixed-Labeled Protein Dimer With a Dual Mode Cavity. J. Magn. Reson. *227*, 66–71.

Kandarian, S.C., and Jackman, R.W. (2006). Intracellular Signaling During Skeletal Muscle Atrophy. Muscle Nerve *33*, 155–165.

Kawai, T., and Akira, S. (2008). Toll-like Receptor and RIG-1-like Receptor Signaling. Ann. N. Y. Acad. Sci. *1143*, 1–20.

Kendrew, J.C., Bodo, G., Dintzis, H.M., Parrish, R.G., Wyckoff, H., and Phillips, D.C. (1958). A Three-Dimensional Model of the Myoglobin Molecule Obtained by X-Ray Analysis. Nature *181*, 662–666.

Kerry, P.S., Turkington, H.L., Ackermann, K., Jameison, S.A., and Bode, B.E. (2014). Analysis of Influenza A Virus NS1 Dimer Interfaces in Solution by Pulse EPR Distance Measurements. J. Phys. Chem. B *118*, 10882–10888.

Kim, S., Brandon, S., Zhou, Z., Cobb, C.E., Edwards, S.J., Moth, C.W., Parry, C.S., Smith, J.A., Lybrand, T.P., Hustedt, E.J., et al. (2011). Determination of Structural Models of the Complex between the Cytoplasmic Domain of Erythrocyte Band 3 and Ankyrin-R Repeats 13–24. J. Biol. Chem. *286*, 20746–20757.

Kirilina, E.P., Prisner, T.F., Bennati, M., Endeward, B., Dzuba, S.A., Fuchs, M.R., Möbius, K., and Schnegg, A. (2005). Molecular Dynamics of Nitroxides in Glasses as Studied by Multi-Frequency EPR. Magn. Reson. Chem. *43*, S119–S129.

Klug, C.S., and Feix, J.B. (2008). Methods and Applications of Site-Directed Spin Labeling EPR Spectroscopy. Methods Cell Biol. *84*, 617–658.

Koyama, S., Hata, S., Witt, C.C., Ono, Y., Lerche, S., Ojima, K., Chiba, T., Doi, N., Kitamura, F., Tanaka, K., et al. (2008). Muscle RING-Finger Protein-1 (MuRF1) as a Connector of Muscle Energy Metabolism and Protein Synthesis. J. Mol. Biol. *376*, 1224–1236.

Krumkacheva, O., and Bagryanskaya, E. (2017). EPR-Based Distance Measurements at Ambient Temperature. J. Magn. Reson. *280*, 117–126.

Kuhn, M., Hyman, A.A., and Beyer, A. (2014). Coiled-Coil Proteins Facilitated the Functional Expansion of the Centrosome. PLOS Comput. Biol. *10*, e1003657.

Kuzhelev, A.A., Trukhin, D.V., Krumkacheva, O.A., Strizhakov, R.K., Rogozhnikova, O.Y., Troitskaya, T.I., Fedin, M.V., Tormyshev, V.M., and Bagryanskaya, E.G. (2015). Room-Temperature Electron Spin Relaxation of Triarylmethyl Radicals at the X- and Q-Bands. J. Phys. Chem. B *119*, 13630–13640.

Langen, R., Oh, K.J., Cascio, D., and Hubbell, W.L. (2000). Crystal Structures of Spin Labeled T4 Lysozyme Mutants: Implications for the Interpretation of EPR Spectra in Terms of Structure. Biochemistry (Mosc.) *39*, 8396–8405.

Lasker, K., Förster, F., Bohn, S., Walzthoeni, T., Villa, E., Unverdorben, P., Beck, F., Aebersold, R., Sali, A., and Baumeister, W. (2012). Molecular Architecture of the 26S Proteasome Holocomplex Determined by an Integrative Approach. Proc. Natl. Acad. Sci. *109*, 1380–1387.

Li, X., and Sodroski, J. (2008). The TRIM5α B-Box 2 Domain Promotes Cooperative Binding to the Retroviral Capsid by Mediating Higher-Order Self-Association. J. Virol. *82*, 11495–11502.

Li, Y., Wu, H., Wu, W., Zhuo, W., Liu, W., Zhang, Y., Cheng, M., Chen, Y.-G., Gao, N., Yu, H., et al. (2014). Structural Insights into the TRIM Family of Ubiquitin E3 Ligases. Cell Res *24*, 762–765.

Liao, M., Cao, E., Julius, D., and Cheng, Y. (2013). Structure of the TRPV1 ion channel determined by electron cryo-microscopy. Nature *504*, 107–112.

Lindgren, M., Eaton, G.R., Eaton, S.S., Jonsson, B.-H., Hammarström, P., Svensson, M., and Carlsson, U. (1997). Electron Spin Echo Decay as a Probe of Aminoxyl Environment in Spin-Labeled Mutants of Human Carbonic Anhydrase II. J. Chem. Soc. Perkin Trans. 2 *0*, 2549–2554.

Liu, Y., Freeman, A.D.J., Déclais, A.-C., Wilson, T.J., Gartner, A., and Lilley, D.M.J. (2015). Crystal Structure of a Eukaryotic GEN1 Resolving Enzyme Bound to DNA. Cell Rep. *13*, 2565–2575.

Loedige, I., Gaidatzis, D., Sack, R., Meister, G., and Filipowicz, W. (2013). The Mammalian TRIM-NHL Protein TRIM71/LIN-41 is a Repressor of mRNA Function. Nucleic Acids Res. *41*, 518–532.

Lueders, P., Jeschke, G., and Yulikov, M. (2011). Double Electron−Electron Resonance Measured Between Gd3+ Ions and Nitroxide Radicals. J. Phys. Chem. Lett. *2*, 604–609.

Lupas, A.N., Bassler, J., and Dunin-Horkawicz, S. (2017). The Structure and Topology of α-Helical Coiled Coils. In Fibrous Proteins: Structures and Mechanisms, D.A.D. Parry, and J.M. Squire, eds. (Cham: Springer International Publishing), pp. 95–129.

Mainz, A., Religa, T.L., Sprangers, R., Linser, R., Kay, L.E., and Reif, B. (2013). NMR Spectroscopy of Soluble Protein Complexes at One Mega-Dalton and Beyond. Angew. Chem. Int. Ed. *52*, 8746–8751.

Marblestone, J.G., Butt, S., McKelvey, D.M., Sterner, D.E., Mattern, M.R., Nicholson, B., and Eddins, M.J. (2013). Comprehensive Ubiquitin E2 Profiling of Ten Ubiquitin E3 Ligases. Cell Biochem. Biophys. *67*, 161–167.

Margraf, D., Bode, B.E., Marko, A., Schiemann, O., and Prisner, T.F. (2007). Conformational Flexibility of Nitroxide Biradicals Determined by X-Band PELDOR Experiments. Mol. Phys. *105*, 2153–2160.

Marsh, D. (2010). Spin-Label EPR for Determining Polarity and Proticity in Biomolecular Assemblies: Transmembrane Profiles. Appl. Magn. Reson. *37*, 435–454.

Martin, R.E., Pannier, M., Diederich, F., Gramlich, V., Hubrich, M., and Spiess, H.W. (1998). Determination of End-to-End Distances in a Series of TEMPO Diradicals of up to 2.8 nm Length with a New Four-Pulse Double Electron Electron Resonance Experiment. Angew. Chem. Int. Ed. *37*, 2833–2837.

Mason, R.P., and Freed, J.H. (1974). Estimating Microsecond Rotational Correlation Times From Lifetime Broadening of Nitroxide Electron Spin Resonance Spectra Near the Rigid Limit. J. Phys. Chem. *78*, 1321–1323.

Massiah, M.A., Simmons, B.N., Short, K.M., and Cox, T.C. (2006). Solution Structure of the RBCC/TRIM B-box1 Domain of Human MID1: B-box with a RING. J. Mol. Biol. *358*, 532–545.

Matalon, E., Huber, T., Hagelueken, G., Graham, B., Frydman, V., Feintuch, A., Otting, G., and Goldfarb, D. (2013). Gadolinium(III) Spin Labels for High-Sensitivity

Distance Measurements in Transmembrane Helices. Angew. Chem. Int. Ed. *52*, 11831–11834.

Mchaourab, H.S., Steed, P.R., and Kazmier, K. (2011). Toward the Fourth Dimension of Membrane Protein Structure: Insight into Dynamics from Spin-Labeling EPR Spectroscopy. Structure *19*, 1549–1561.

McPherson, A., and Gavira, J.A. (2014). Introduction to Protein Crystallization. Acta Crystallogr. Sect. F *70*, 2–20.

Means, G.E., and Feeney, R.E. (1990). Chemical Modifications of Proteins: History and Applications. Bioconjug. Chem. *1*, 2–12.

Meroni, G., and Diez-Roux, G. (2005). TRIM/RBCC, a Novel Class of 'Single Protein RING Finger' E3 Ubiquitin Ligases. BioEssays *27*, 1147–1157.

Meselson, M.S., and Radding, C.M. (1975). A General Model for Genetic Recombination. Proc. Natl. Acad. Sci. *72*, 358–361.

Miao, J., Ishikawa, T., Robinson, I.K., and Murnane, M.M. (2015). Beyond Crystallography: Diffractive Imaging Using Coherent X-Ray Light Sources. Science *348*, 530–535.

Milan, G., Romanello, V., Pescatore, F., Armani, A., Paik, J.-H., Frasson, L., Seydel, A., Zhao, J., Abraham, R., Goldberg, A.L., et al. (2015). Regulation of Autophagy and the Ubiquitin–Proteasome System by the FoxO Transcriptional Network During Muscle Atrophy. Nat. Commun. *6*, ncomms7670.

Milov, A.D., Maryasov, A.G., and Tsvetkov, Y.D. (1998). Pulsed Electron Double Resonance (PELDOR) and its Applications in Free-Radicals Research. Appl. Magn. Reson. *15*, 107–143.

Mims, W.B. (1965). Pulsed Endor Experiments. Proc. R. Soc. Lond. Ser. Math. Phys. Sci. *283*, 452–457.

Mims, W.B., Nassau, K., and McGee, J.D. (1961). Spectral Diffusion in Electron Resonance Lines. Phys. Rev. *123*, 2059–2069.

Monera, O.D., Zhou, N.E., Kay, C.M., and Hodges, R.S. (1993). Comparison of Antiparallel and Parallel Two-Stranded Alpha-Helical Coiled-Coils. Design, Synthesis, and Characterization. J. Biol. Chem. *268*, 19218–19227.

Motion, C.L., Lovett, J.E., Bell, S., Cassidy, S.L., Cruickshank, P.A.S., Bolton, D.R., Hunter, R.I., El Mkami, H., Van Doorslaer, S., and Smith, G.M. (2016). DEER Sensitivity Between Iron Centers and Nitroxides in Heme-Containing Proteins Improves Dramatically Using Broadband, High-Field EPR. J. Phys. Chem. Lett. *7*, 1411–1415.

Mrosek, M., Labeit, D., Witt, S., Heerklotz, H., Castelmur, E. von, Labeit, S., and Mayans, O. (2007). Molecular Determinants for the Recruitment of the Ubiquitin-Ligase MuRF-1 onto M-Line Titin. FASEB J. *21*, 1383–1392.

Mrosek, M., Meier, S., Ucurum-Fotiadis, Z., von Castelmur, E., Hedbom, E., Lustig, A., Grzesiek, S., Labeit, D., Labeit, S., and Mayans, O. (2008). Structural Analysis of B-Box 2 from MuRF1: Identification of a Novel Self-Association Pattern in a RING-like Fold. Biochemistry (Mosc.) *47*, 10722–10730.

Murzin, A.G., Brenner, S.E., Hubbard, T., and Chothia, C. (1995). SCOP: A Structural Classification of Proteins Database for the Investigation of Sequences and Structures. J. Mol. Biol. *247*, 536–540.

Narr, E., Godt, A., and Jeschke, G. (2002). Selective Measurements of a Nitroxide–Nitroxide Separation of 5 nm and a Nitroxide–Copper Separation of 2.5 nm in a Terpyridine-Based Copper(II) Complex by Pulse EPR Spectroscopy. Angew. Chem. Int. Ed. *41*, 3907–3910.

Nielsen, R.D., Canaan, S., Gladden, J.A., Gelb, M.H., Mailer, C., and Robinson, B.H. (2004). Comparing Continuous Wave Progressive Saturation EPR and Time Domain Saturation Recovery EPR over the Entire Motional Range of Nitroxide Spin Labels. J. Magn. Reson. *169*, 129–163.

Orengo, C., Michie, A., Jones, S., Jones, D., Swindells, M., and Thornton, J. (1997). CATH – a Hierarchic Classification of Protein Domain Structures. Structure *5*, 1093–1109.

Oshiumi, H., Miyashita, M., Inoue, N., Okabe, M., Matsumoto, M., and Seya, T. (2010). The Ubiquitin Ligase Riplet Is Essential for RIG-I-Dependent Innate Immune Responses to RNA Virus Infection. Cell Host Microbe *8*, 496–509.

Owenius, R., Engström, M., Lindgren, M., and Huber, M. (2001). Influence of Solvent Polarity and Hydrogen Bonding on the EPR Parameters of a Nitroxide Spin Label Studied by 9-GHz and 95-GHz EPR Spectroscopy and DFT Calculations. J. Phys. Chem. A *105*, 10967–10977.

Paletta, J.T., Pink, M., Foley, B., Rajca, S., and Rajca, A. (2012). Synthesis and Reduction Kinetics of Sterically Shielded Pyrrolidine Nitroxides. Org. Lett. *14*, 5322–5325.

Palmer, M.R., Suiter, C.L., Henry, G.E., Rovnyak, J., Hoch, J.C., Polenova, T., and Rovnyak, D. (2015). Sensitivity of Nonuniform Sampling NMR. J. Phys. Chem. B *119*, 6502–6515.

Pannier, M., Veit, S., Godt, A., Jeschke, G., and Spiess, H.W. (2011). Dead-Time Free Measurement of Dipole–Dipole Interactions Between Electron Spins. J. Magn. Reson. *213*, 316–325.

Park, Y.-J., Sudhoff, K.B., Andrews, A.J., Stargell, L.A., and Luger, K. (2008). Histone Chaperone Specificity in Rtt109 Activation. Nat Struct Mol Biol *15*, 957–964.

Parkinson, M.J., and Lilley, D.M.. (1997). The Junction-Resolving Enzyme T7 Endonuclease I: Quaternary Structure and Interaction with DNA. J. Mol. Biol. *270*, 169–178.

Parthasarathy, S., Nishiyama, Y., and Ishii, Y. (2013). Sensitivity and Resolution Enhanced Solid-State NMR for Paramagnetic Systems and Biomolecules Under Very Fast Magic Angle Spinning. Acc. Chem. Res. *46*, 2127–2135.

Pauli, W. (1940). The Connection Between Spin and Statistics. Phys. Rev. *58*, 716–722.

Perrakis, A., Morris, R., and Lamzin, V.S. (1999). Automated Protein Model Building Combined with Iterative Structure Refinement. Nat. Struct. Mol. Biol. *6*, 458–463.

Perry, A.K., Chen, G., Zheng, D., Tang, H., and Cheng, G. (2005). The Host Type I Interferon Response to Viral and Bacterial Infections. Cell Res. *15*, 407–422.

Pickart, C.M. (2001). Mechanisms Underlying Ubiquitination. Annu. Rev. Biochem. *70*, 503–533.

Plato, M., Steinhoff, H.-J., Wegner, C., Torring, J.T., Savitsky, A., and Mobius, K. (2002). Molecular Orbital Study of Polarity and Hydrogen Bonding Effects on the g and Hyperfine Tensors of Site Directed NO Spin Labelled Bacteriorhodopsin. Mol. Phys. *100*, 3711–3721.

Politis, A., Stengel, F., Hall, Z., Hernández, H., Leitner, A., Walzthoeni, T., Robinson, C.V., and Aebersold, R. (2014). A Mass Spectrometry-Based Hybrid Method for Structural Modeling of Protein Complexes. Nat. Methods *11*, 403–406.

Polyhach, Y., Bordignon, E., and Jeschke, G. (2011a). Rotamer Libraries of Spin Labelled Cysteines for Protein Studies. Phys. Chem. Chem. Phys. PCCP *13*, 2356–2366.

Polyhach, Y., Bordignon, E., and Jeschke, G. (2011b). Rotamer Libraries of Spin Labelled Cysteines for Protein Studies. Phys. Chem. Chem. Phys. *13*, 2356–2366.

Pornsuwan, S., Giller, K., Riedel, D., Becker, S., Griesinger, C., and Bennati, M. (2013). Long-Range Distances in Amyloid Fibrils of α-Synuclein from PELDOR Spectroscopy. Angew. Chem. Int. Ed Engl. *52*, 10290–10294.

Potter, H., and Dressler, D. (1976). On the Mechanism of Genetic Recombination: Electron Microscopic Observation of Recombination Intermediates. Proc. Natl. Acad. Sci. U. S. A. *73*, 3000–3004.

Putnam, C.D., Hammel, M., Hura, G.L., and Tainer, J.A. (2007). X-ray Solution Scattering (SAXS) Combined with Crystallography and Computation: Defining Accurate Macromolecular Structures, Conformations and Assemblies in Solution. Q. Rev. Biophys. *40*, 191–285.

Rabi, I.I., Zacharias, J.R., Millman, S., and Kusch, P. (1938). A New Method of Measuring Nuclear Magnetic Moment. Phys. Rev. *53*, 318–318.

Rajsbaum, R., Albrecht, R.A., Wang, M.K., Maharaj, N.P., Versteeg, G.A., Nistal-Villán, E., García-Sastre, A., and Gack, M.U. (2012). Species-Specific Inhibition of RIG-I Ubiquitination and IFN Induction by the Influenza A Virus NS1 Protein. PLOS Pathog. *8*, e1003059.

Reddy, T.J., Iwama, T., Halpern, H.J., and Rawal, V.H. (2002). General Synthesis of Persistent Trityl Radicals for EPR Imaging of Biological Systems. J. Org. Chem. *67*, 4635–4639.

Reginsson, G.W., Kunjir, N.C., Sigurdsson, S.T., and Schiemann, O. (2012a). Trityl Radicals: Spin Labels for Nanometer-Distance Measurements. Chem. – Eur. J. *18*, 13580–13584.

Reginsson, G.W., Hunter, R.I., Cruickshank, P.A.S., Bolton, D.R., Sigurdsson, S.T., Smith, G.M., and Schiemann, O. (2012b). W-band PELDOR with 1kW Microwave Power: Molecular Geometry, Flexibility and Exchange Coupling. J. Magn. Reson. *216*, 175–182.

Roozen, M.J.G.W., and Hemminga, M.A. (1990). Molecular Motion in Sucrose-Water Mixtures in the Liquid and Glassy State as Studied by Spin Probe ESR. J. Phys. Chem. *94*, 7326–7329.

Salikhov, K.M., and Zavoiskaya, N.E. (2015). Zavoisky and the Discovery of EPR. Resonance *20*, 963–968.

Samish, I., Bourne, P.E., and Najmanovich, R.J. (2015). Achievements and Challenges in Structural Bioinformatics and Computational Biophysics. Bioinformatics *31*, 146–150.

Sanchez, J.G., Okreglicka, K., Chandrasekaran, V., Welker, J.M., Sundquist, W.I., and Pornillos, O. (2014). The Tripartite Motif Coiled-Coil is an Elongated Antiparallel Hairpin Dimer. Proc. Natl. Acad. Sci. *111*, 2494–2499.

Sanchez, J.G., Chiang, J.J., Sparrer, K.M.J., Alam, S.L., Chi, M., Roganowicz, M.D., Sankaran, B., Gack, M.U., and Pornillos, O. (2016). Mechanism of TRIM25 Catalytic Activation in the Antiviral RIG-I Pathway. Cell Rep. *16*, 1315–1325.

Schiemann, O., Cekan, P., Margraf, D., Prisner, T.F., and Sigurdsson, S.T. (2009). Relative Orientation of Rigid Nitroxides by PELDOR: Beyond Distance Measurements in Nucleic Acids. Angew. Chem. Int. Ed. *48*, 3292–3295.

Schmalbein, H.K. (1987). ESP 380 EPR Spectrometer. 1987.

Schmidt, T., Wälti, M.A., Baber, J.L., Hustedt, E.J., and Clore, G.M. (2016). Long Distance Measurements up to 160 Å in the GroEL Tetradecamer Using Q-Band DEER EPR Spectroscopy. Angew. Chem. *128*, 16137–16141.

Schmidt-Böcking, H., Schmidt, L., Lüdde, H.J., Trageser, W., Templeton, A., and Sauer, T. (2016). The Stern-Gerlach experiment revisited. Eur. Phys. J. H *41*, 327–364.

Schöps, P., Spindler, P.E., Marko, A., and Prisner, T.F. (2015). Broadband Spin Echoes and Broadband SIFTER in EPR. J. Magn. Reson. *250*, 55–62.

Schwacha, A., and Kleckner, N. (1995). Identification of Double Holliday Junctions as Intermediates in Meiotic Recombination. Cell *83*, 783–791.

Schwede, T. (2013). Protein Modeling: What Happened to the “Protein Structure Gap”? Structure *21*, 1531–1540.

Schweiger, A., and Jeschke, G. (2001). Principles of Pulse Electron Paramagnetic Resonance (Oxford University Press).

Schwieters, C.D., Kuszewski, J.J., Tjandra, N., and Marius Clore, G. (2003). The Xplor-NIH NMR Molecular Structure Determination Package. J. Magn. Reson. *160*, 65–73.

Selth, L., and Svejstrup, J.Q. (2007). Vps75, A New Yeast Member of the NAP Histone Chaperone Family. J. Biol. Chem. *282*, 12358–12362.

Seth, R.B., Sun, L., and Chen, Z.J. (2006). Antiviral innate immunity pathways. Cell Res. *16*, 141–147.

Short, K.M., and Cox, T.C. (2006). Subclassification of the RBCC/TRIM Superfamily Reveals a Novel Motif Necessary for Microtubule Binding. J. Biol. Chem. *281*, 8970–8980.

Søndergaard, C.R., Garrett, A.E., Carstensen, T., Pollastri, G., and Nielsen, J.E. (2009). Structural Artifacts in Protein−Ligand X-ray Structures: Implications for the Development of Docking Scoring Functions. J. Med. Chem. *52*, 5673–5684.

Spindler, P.E., Zhang, Y., Endeward, B., Gershernzon, N., Skinner, T.E., Glaser, S.J., and Prisner, T.F. (2012). Shaped Optimal Control Pulses for Increased Excitation Bandwidth in EPR. J. Magn. Reson. *218*, 49–58.

Steinhoff, H.-J., Müller, M., Beier, C., and Pfeiffer, M. (2000). Molecular dynamics simulation and EPR spectroscopy of nitroxide side chains in bacteriorhodopsin. J. Mol. Liq. *84*, 17–27.

Stevens, M.A., McKay, J.E., Robinson, J.L.S., Mkami, H.E., Smith, G.M., and Norman, D.G. (2016). The Use of the Rx Spin Label in Orientation Measurement on Proteins, by EPR. Phys. Chem. Chem. Phys. *18*, 5799–5806.

Stoll, S., and Schweiger, A. (2006). EasySpin, a Comprehensive Software Package for Spectral Simulation and Analysis in EPR. J. Magn. Reson. *178*, 42–55.

Tawa, N.E., Odessey, R., and Goldberg, A.L. (1997). Inhibitors of the Proteasome Reduce the Accelerated Proteolysis in Atrophying Rat Skeletal Muscles. J. Clin. Invest. *100*, 197–203.

Tkach, I., Pornsuwan, S., Höbartner, C., Wachowius, F., Sigurdsson, S.T., Baranova, T.Y., Diederichsen, U., Sicoli, G., and Bennati, M. (2013). Orientation Selection in Distance Measurements Between Nitroxide Spin Labels at 94 GHz EPR With Variable Dual Frequency Irradiation. Phys. Chem. Chem. Phys. *15*, 3433–3437.

Todd, A.P., Cong, J., Levinthal, F., Levinthal, C., and Hubell, W.L. (1989). Site-Directed Mutagenesis of Colicin E1 Provides Specific Attachment Sites for Spin Labels Whose Spectra are Sensitive to Local Conformation. Proteins Struct. Funct. Bioinforma. *6*, 294–305.

Toledo Warshaviak, D., Khramtsov, V.V., Cascio, D., Altenbach, C., and Hubbell, W.L. (2013). Structure and Dynamics of an Imidazoline Nitroxide Side Chain With Strongly Hindered Internal Motion in Proteins. J. Magn. Reson. *232*, 53–61.

Toniolo, C., Crisma, M., and Formaggio, F. (1998). TOAC, a Nitroxide Spin-Labeled, Achiral Cα-Tetrasubstituted α-Amino Acid, is an Excellent Tool in Material Science and Biochemistry. Pept. Sci. *47*, 153–158.

Tsubota, T., Berndsen, C.E., Erkmann, J.A., Smith, C.L., Yang, L., Freitas, M.A., Denu, J.M., and Kaufman, P.D. (2007). Histone H3-K56 Acetylation Is Catalyzed by Histone Chaperone-Dependent Complexes. Mol. Cell *25*, 703–712.

Udeshi, N.D., Mertins, P., Svinkina, T., and Carr, S.A. (2013). Large-Scale Identification of Ubiquitination Sites by Mass Spectrometry. Nat. Protoc. *8*, 1950–1960.

Vámosi, G., Baudendistel, N., von der Lieth, C.-W., Szalóki, N., Mocsár, G., Müller, G., Brázda, P., Waldeck, W., Damjanovich, S., Langowski, J., et al. (2008). Conformation of the c-Fos/c-Jun Complex In Vivo: A Combined FRET, FCCS, and MD-Modeling Study. Biophys. J. *94*, 2859–2868.

Verlet, L. (1967). Computer "Experiments" on Classical Fluids. I. Thermodynamical Properties of Lennard-Jones Molecules. Phys. Rev. *159*, 98–103.

Voss, J., Salwiński, L., Kaback, H.R., and Hubbell, W.L. (1995). A Method for Distance Determination in Proteins Using a Designed Metal Ion Binding Site and Site-Directed Spin Labeling: Evaluation with T4 Lysozyme. Proc. Natl. Acad. Sci. U. S. A. *92*, 12295–12299.

Waddell, D.S., Baehr, L.M., Brandt, J. van den, Johnsen, S.A., Reichardt, H.M., Furlow, J.D., and Bodine, S.C. (2008). The Glucocorticoid Receptor and FOXO1 Synergistically Activate the Skeletal Muscle Atrophy-Associated MuRF1 Gene. Am. J. Physiol. - Endocrinol. Metab. *295*, E785–E797.

Ward, R., Zoltner, M., Beer, L., El Mkami, H., Henderson, I.R., Palmer, T., and Norman, D.G. (2009a). The Orientation of a Tandem POTRA Domain Pair, of the Beta-Barrel Assembly Protein BamA, Determined by PELDOR Spectroscopy. Structure *17*, 1187–1194.

Ward, R., Bowman, A., El-Mkami, H., Owen-Hughes, T., and Norman, D.G. (2009b). Long Distance PELDOR Measurements on the Histone Core Particle. J. Am. Chem. Soc. *131*, 1348–1349.

Ward, R., Bowman, A., Sozudogru, E., El-Mkami, H., Owen-Hughes, T., and Norman, D.G. (2010). EPR Distance Measurements in Deuterated Proteins. J. Magn. Reson. *207*, 164–167.

Watson, J.D., and Crick, F.H.C. (1953). Molecular Structure of Nucleic Acids: A Structure for Deoxyribose Nucleic Acid. Nature *171*, 737–738.

Webb, B., and Sali, A. (2002). Comparative Protein Structure Modeling Using MODELLER. In Current Protocols in Bioinformatics, (John Wiley & Sons, Inc.), p.

Weil, J.A., and Bolton, J.R. (2007). Electron Paramagnetic Resonance: Elementary Theory and Practical Applications (John Wiley & Sons).

Weinert, C., Morger, D., Djekic, A., Grütter, M.G., and Mittl, P.R.E. (2015). Crystal Structure of TRIM20 C-Terminal Coiled-Coil/B30.2 Fragment: Implications for the Recognition of Higher Order Oligomers. Sci. Rep. *5*, srep10819.

White, G.F., Ottignon, L., Georgiou, T., Kleanthous, C., Moore, G.R., Thomson, A.J., and Oganesyan, V.S. (2007). Analysis of Nitroxide Spin Label Motion in a Protein–Protein Complex Using Multiple Frequency EPR Spectroscopy. J. Magn. Reson. *185*, 191–203.

Wilkins, M.H.F., Stokes, A.R., and Wilson, H.R. (1953). Molecular Structure of Nucleic Acids: Molecular Structure of Deoxypentose Nucleic Acids. Nature *171*, 738–740.

Witt, S.H., Granzier, H., Witt, C.C., and Labeit, S. (2005). MuRF-1 and MuRF-2 Target a Specific Subset of Myofibrillar Proteins Redundantly: Towards Understanding MuRF-dependent Muscle Ubiquitination. J. Mol. Biol. *350*, 713–722.

Wright, K.M., Du, H., Dagnachew, M., and Massiah, M.A. (2016). Solution Structure of the Microtubule-Targeting COS Domain of MID1. FEBS J. *283*, 3089–3102.

Wyk, J.A. van, Reynhardt, E.C., High, G.L., and Kiflawi, I. (1997). The Dependences of ESR Line Widths and Spin - Spin Relaxation Times of Single Nitrogen Defects on the Concentration of Nitrogen Defects in Diamond. J. Phys. Appl. Phys. *30*, 1790.

Yong, L., Harbridge, J., Quine, R.W., Rinard, G.A., Eaton, S.S., Eaton, G.R., Mailer, C., Barth, E., and Halpern, H.J. (2001). Electron Spin Relaxation of Triarylmethyl Radicals in Fluid Solution. J. Magn. Reson. *152*, 156–161.

Yoo, J.-S., Kato, H., and Fujita, T. (2014). Sensing Viral Invasion by RIG-I Like Receptors. Curr. Opin. Microbiol. *20*, 131–138.

Zavoisky, E. (1945). Paramagnetic Relaxation of Liquid Solutions for Perpendicular Fields. J Phys USSR *9*, 211.

Zecevic, A., Eaton, G.R., Eaton, S.S., and Lindgren, M. (1998). Dephasing of Electron Spin Echoes for Nitroxyl Radicals in Glassy Solvents by Non-Methyl and Methyl Protons. Mol. Phys. *95*, 1255–1263.

Zhang, J., Yang, J., Jang, R., and Zhang, Y. (2015). GPCR-I-TASSER: A Hybrid Approach to G Protein-Coupled Receptor Structure Modeling and the Application to the Human Genome. Structure *23*, 1538–1549.

Zhou, X.E., Gao, X., Barty, A., Kang, Y., He, Y., Liu, W., Ishchenko, A., White, T.A., Yefanov, O., Han, G.W., et al. (2016). X-ray Laser Diffraction for Structure Determination of the Rhodopsin-Arrestin Complex. Sci. Data *3*, 160021.

Zou, P., and Mchaourab, H.S. (2010). Increased Sensitivity and Extended Range of Distance Measurements in Spin-Labeled Membrane Proteins: Q-Band Double Electron-Electron Resonance and Nanoscale Bilayers. Biophys. J. *98*, L18–L20.

Appendix:

Additional Contributions:

Chapter 4: Determining the Structure of the 16 N Terminal Residues of Endo I.	Protein Expression and purification: Alasdair Freeman, Adam Leahy, Katherine Mackay PELDOR Measurements: Hassane El-Mkami
Chapter 5: Using EPR to Analyse the Conformation of the Coiled Coil Domain from MuRF 1.	PELDOR Measurements: Hassane El-Mkami
Chapter 6: Using Protein Duteration to Measure Spin Label Distances greater than 100 Å within the Coiled Coil Region of Trim 25.	PELDOR Measurements: Hassane El-Mkami
Chapter 7: Suitability of the Rigid Spin Label Rx for Orientation Selective PELDOR	Vps 75 A19-K20Rx Buttressing residue mutations: James Robson PELDOR Measurements: Hassane El-Mkami

Chapter 5: Using EPR to Analyse the Conformation of the Coiled Coil Domain from MuRF 1.

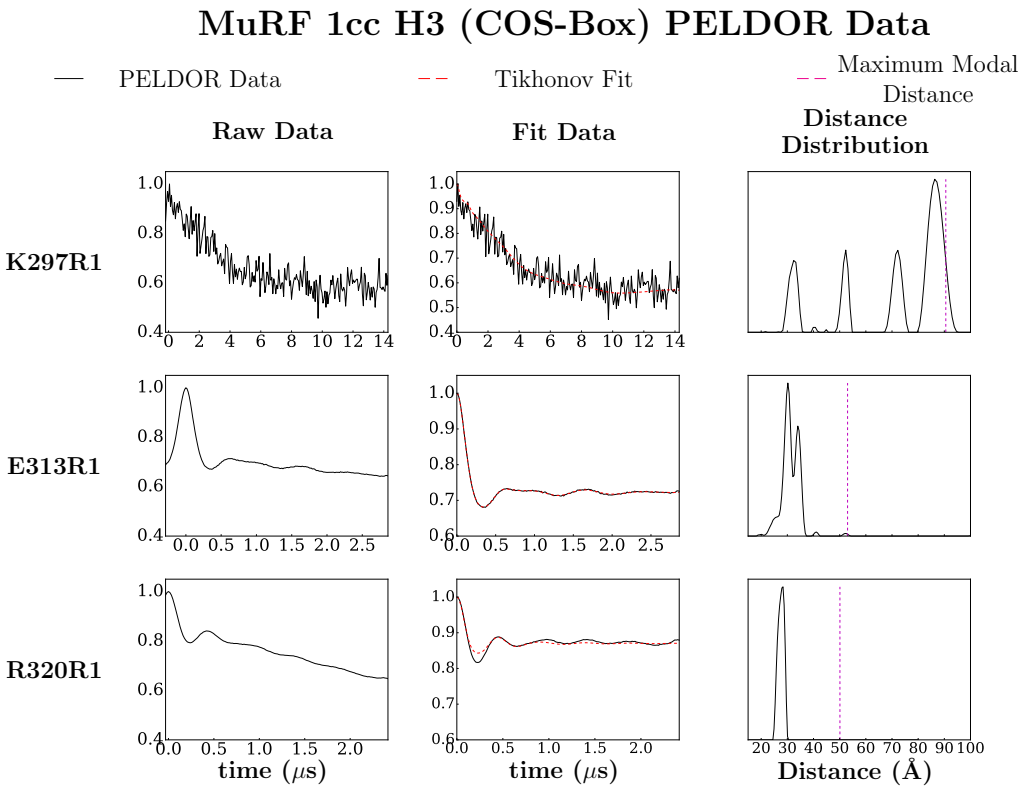

Figure S5.1: Raw, background corrected (Fit) and Tikhonov distance distributions from PELDOR of R1 bound to the MuRF 1cc COS-Box domain. The solid black line represents the PELDOR data, or analysed PELDOR data, the dashed red line is the Tikhonov fit, and the dashed magenta line is the distance measurable from a single oscillation in the raw PELDOR data with a wavelength equivalent to the experimental time period.

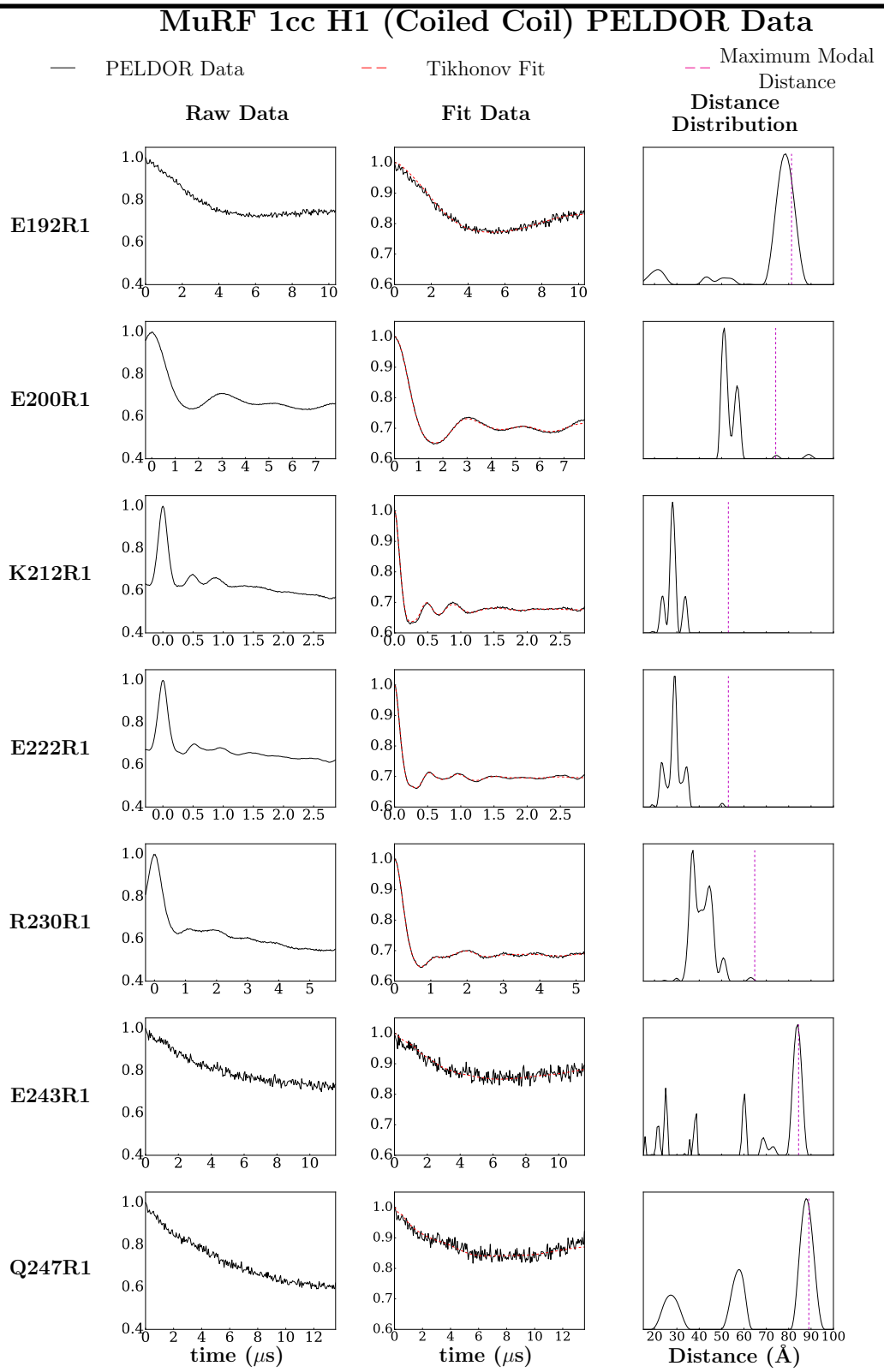

Figure S5.2: Raw, background corrected (Fit) and Tikhonov distance distributions from PELDOR of R1 bound to the MuRF 1cc coiled coil domain. The solid black line represents the PELDOR data, or the modified PELDOR data, the dashed red line is the Tikhonov fit, and the dashed magenta line is the distance measurable from a single oscillation in the raw PELDOR data with a wavelength equivalent to the experimental time period.

Chapter 6: Using Protein Duteration to Measure Spin Label Distances greater than 100 Å within the Coiled Coil Region of Trim 25.

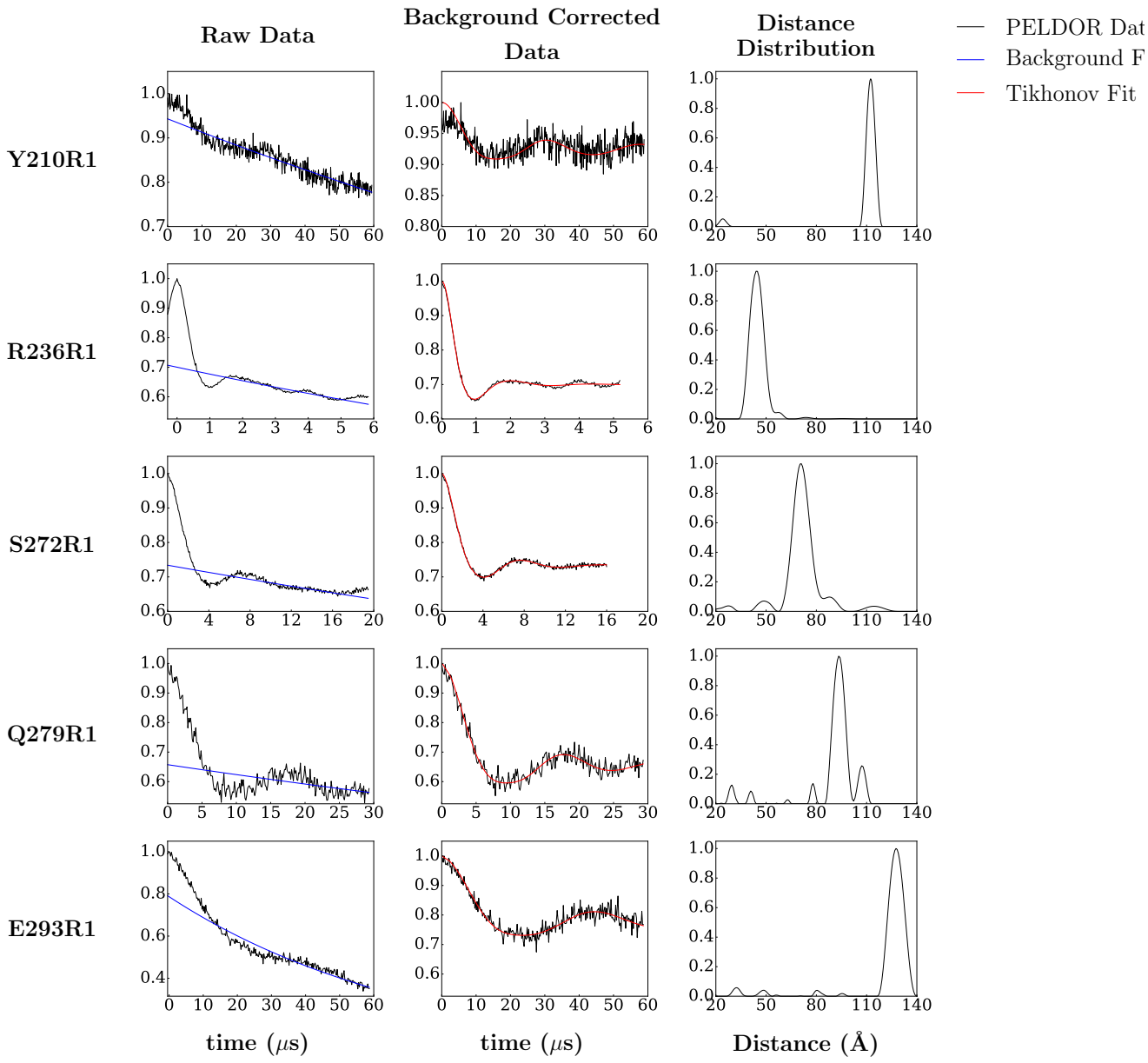

Figure S6.1: Raw, Background Corrected and the Distance distribution from the Tikhonov fit for PELDOR data of R1 at a series of different binding positions on the Trim 25cc construct. The raw and analysed data are displayed as black lines, fits are displayed as solid blue (background correction) or red (Tikhonov fit) data.

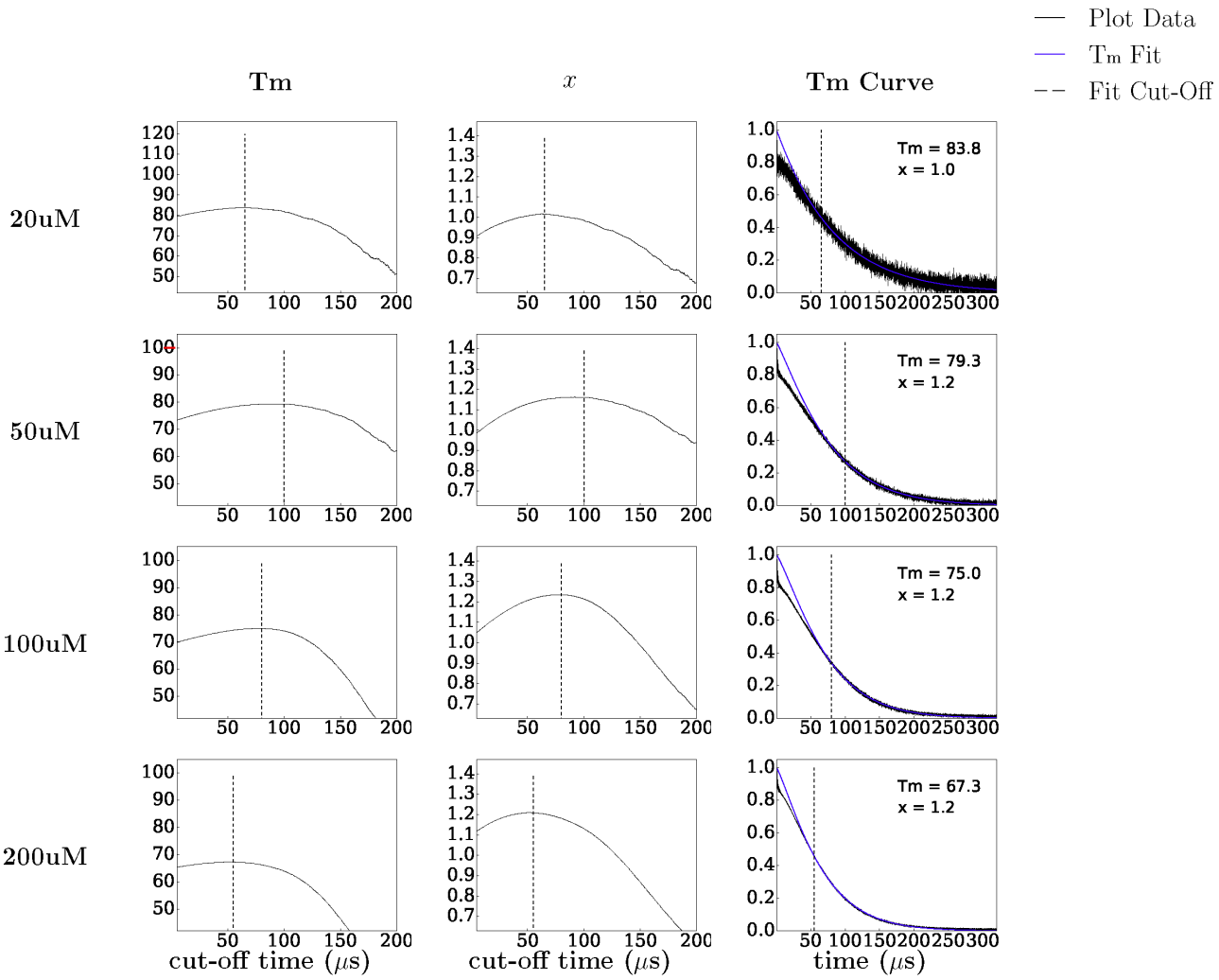

Figure S6.2: T_m Data from various different concentrations of 4'-amino TEMPO. The T_m curve was fit from a series of different time periods until the end of the data to a stretched exponential of the form: $P(t) = P(0)e^{(\frac{-1}{T_m})^x}$. All T_m curves were normalised so that their maximum was 1 allowing P(0) to be treated as 1. The plots show the T_m and x values for fits to the experimental data against the different truncation times used for the fit. The dashed line was the time period determined to give the highest T_m outside the noise of the fit values. The T_m curve plots the experimental data (black line) alongside the final fit (blue line) with the fit values of T_m and x displayed.

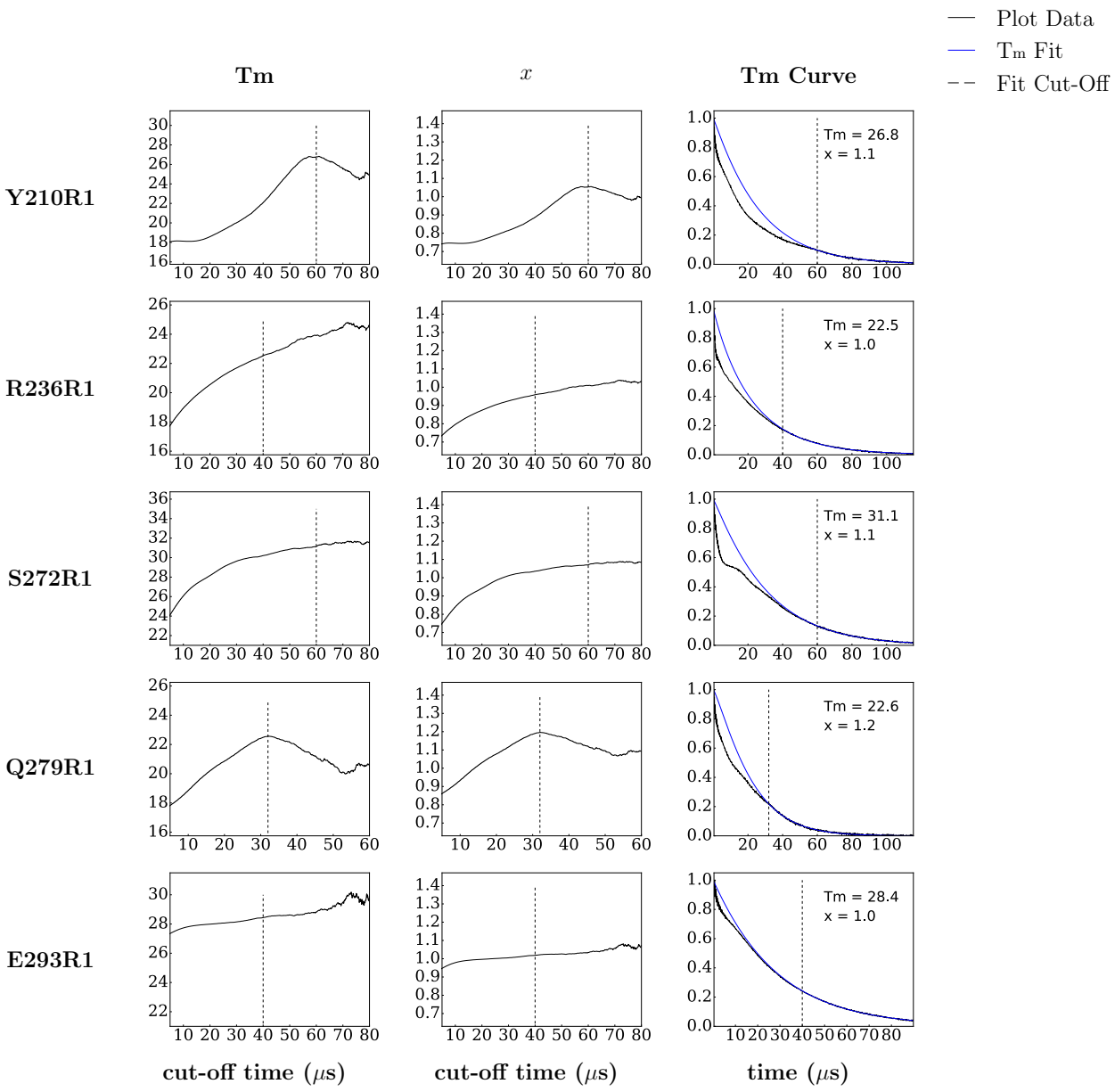

Figure S6.3: T_m Data from binding positions on Trim 25cc which PELDOR was measured from. The T_m curve was fit from a series of different time periods until the end of the data to a stretched exponential of the form: $P(t) = P(0)e^{(\frac{-1}{T_m})^x}$. All T_m curves were normalised so that their maximum was 1 allowing P(0) to be treated as 1. The plots show the T_m and x values for fits to the experimental data against the different truncation times used for the fit. The dashed line was the time period determined to give the highest T_m outside the noise of the fit values. The T_m curve plots the experimental data (black line) alongside the final fit (blue line) with the fit values of T_m and x displayed.

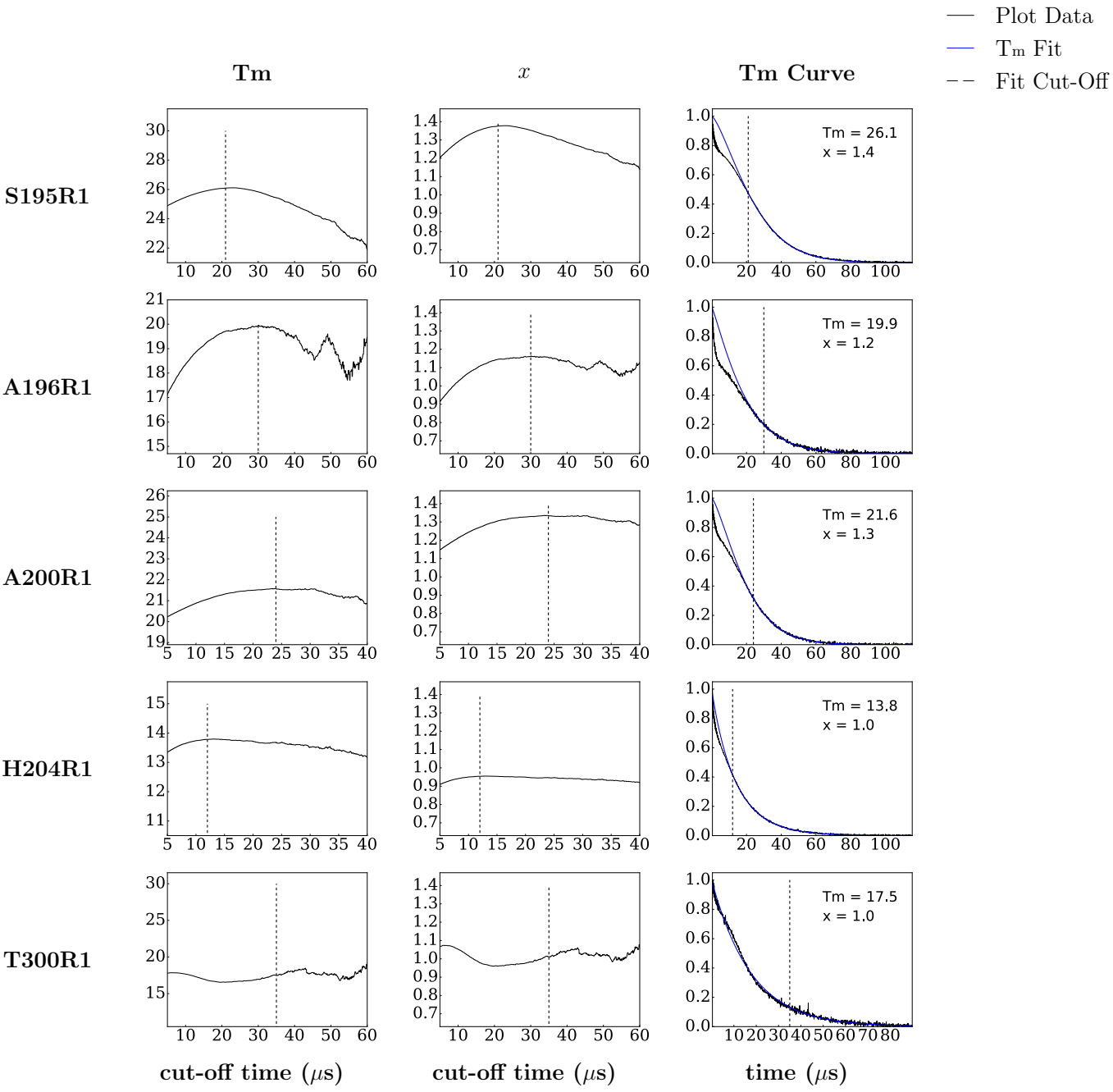

Figure S6.4: T_m Data from binding positions on Trim 25cc that did not produce PELDOR data. The T_m curve was fit from a series of different time periods until the end of the data to a stretched exponential of the form: $P(t) = P(0)e^{(\frac{-1}{Tm})^x}$. All T_m curves were normalised so that their maximum was 1 allowing P(0) to be treated as 1. The plots show the T_m and x values for fits to the experimental data against the different truncation times used for the fit. The dashed line was the time period determined to give the highest T_m outside the noise of the fit values. The T_m curve plots the experimental data (black line) alongside the final fit (blue line) with the fit values of T_m and x displayed.

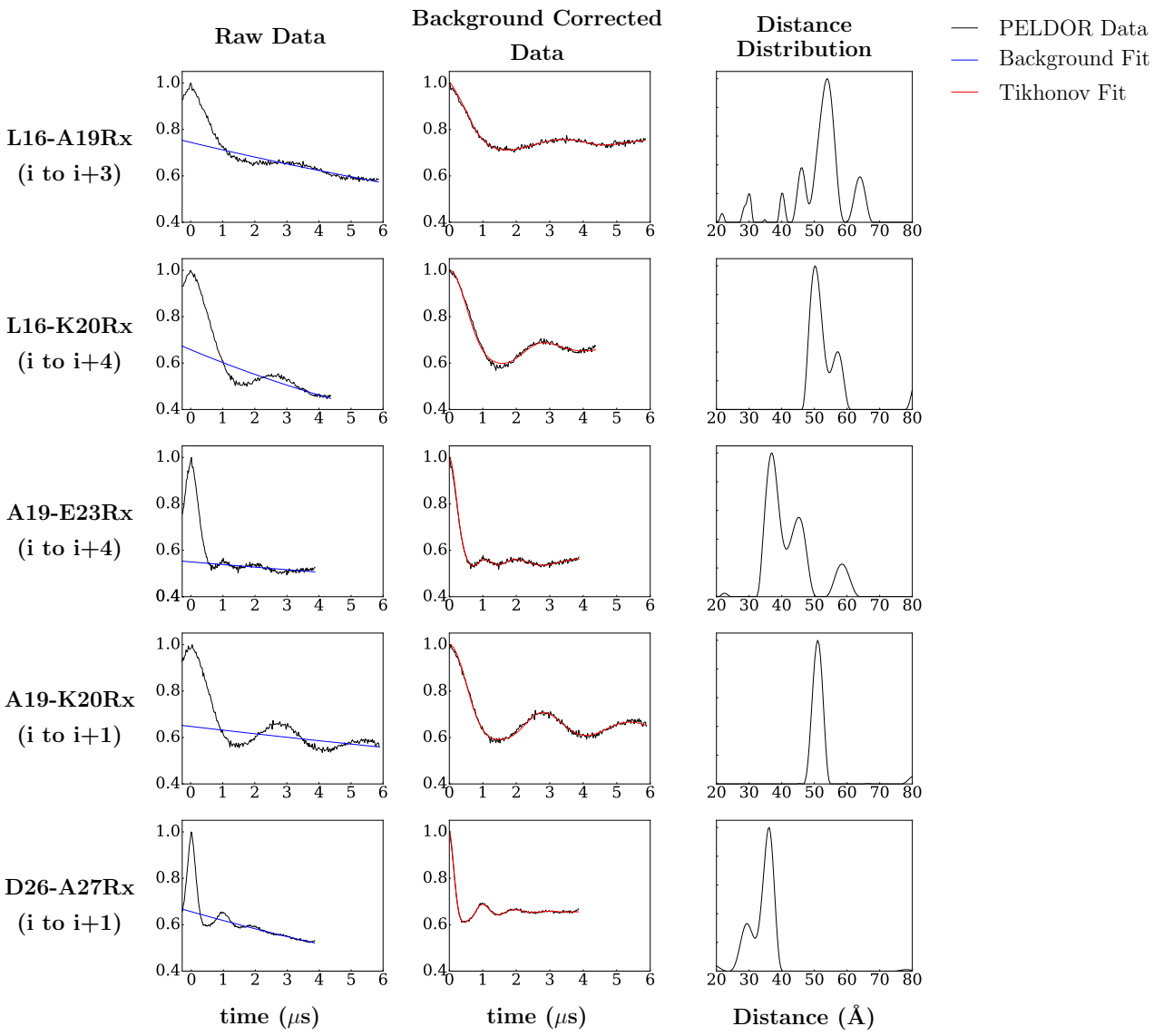

Figure S7.1: Raw data, background corrected data, and distance distributions derived from PELDOR of Rx bound to the Vps 75 dimerization α-helix. The raw PELDOR data along with results from background correction and the Tikhonov fit are displayed as solid black lines, the background correction is displayed as a solid blue line and the Tikhonov fit as a solid red line for each Rx construct.

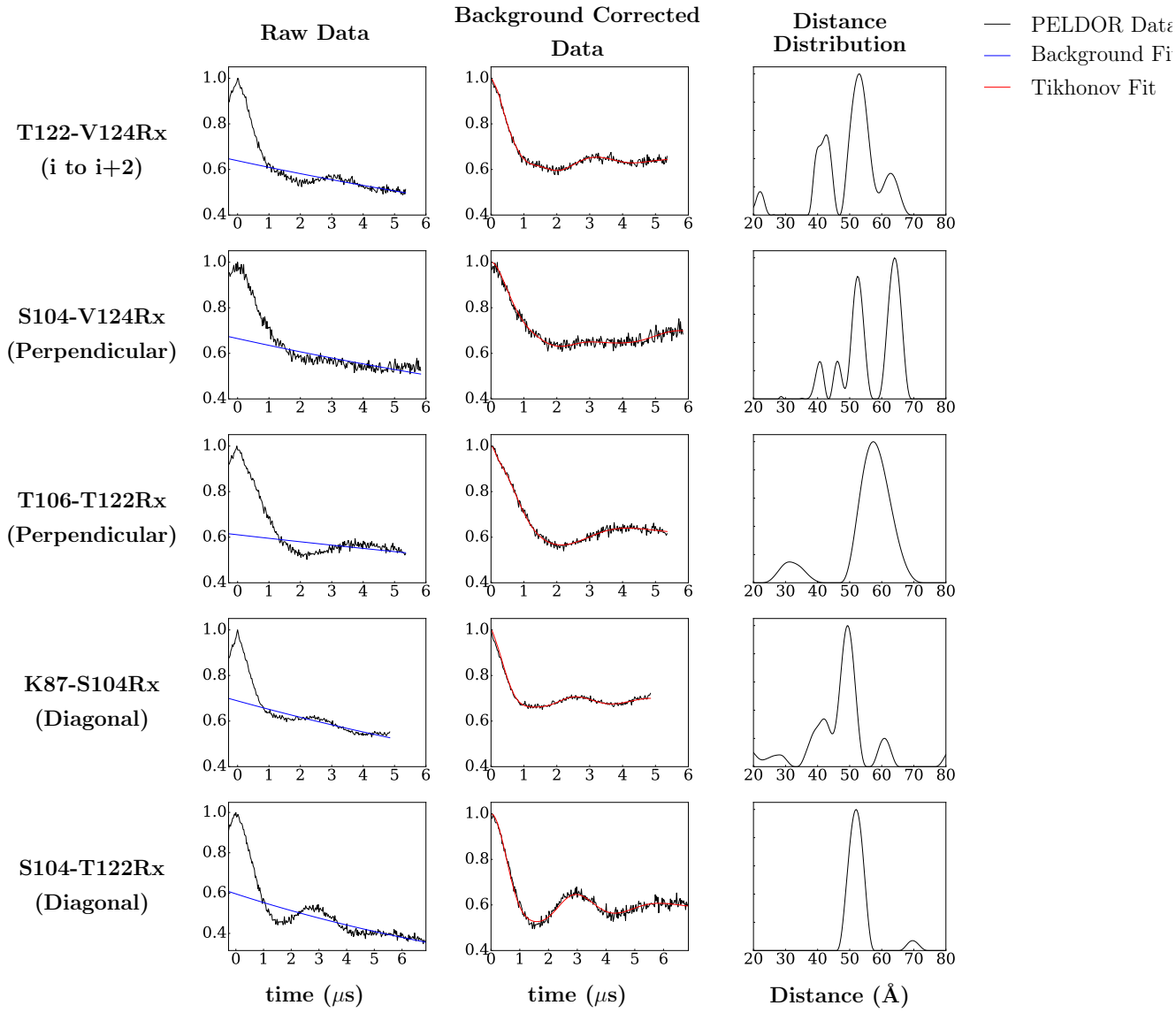

Figure S7.2: Raw data, background corrected data, and distance distributions derived from PELDOR of Rx bound to the β-sheet. The raw PELDOR data along with results from background correction and the Tikhonov fit are displayed as solid black lines, the background correction is displayed as a solid blue line and the Tikhonov fit as a solid red line for each Rx construct.

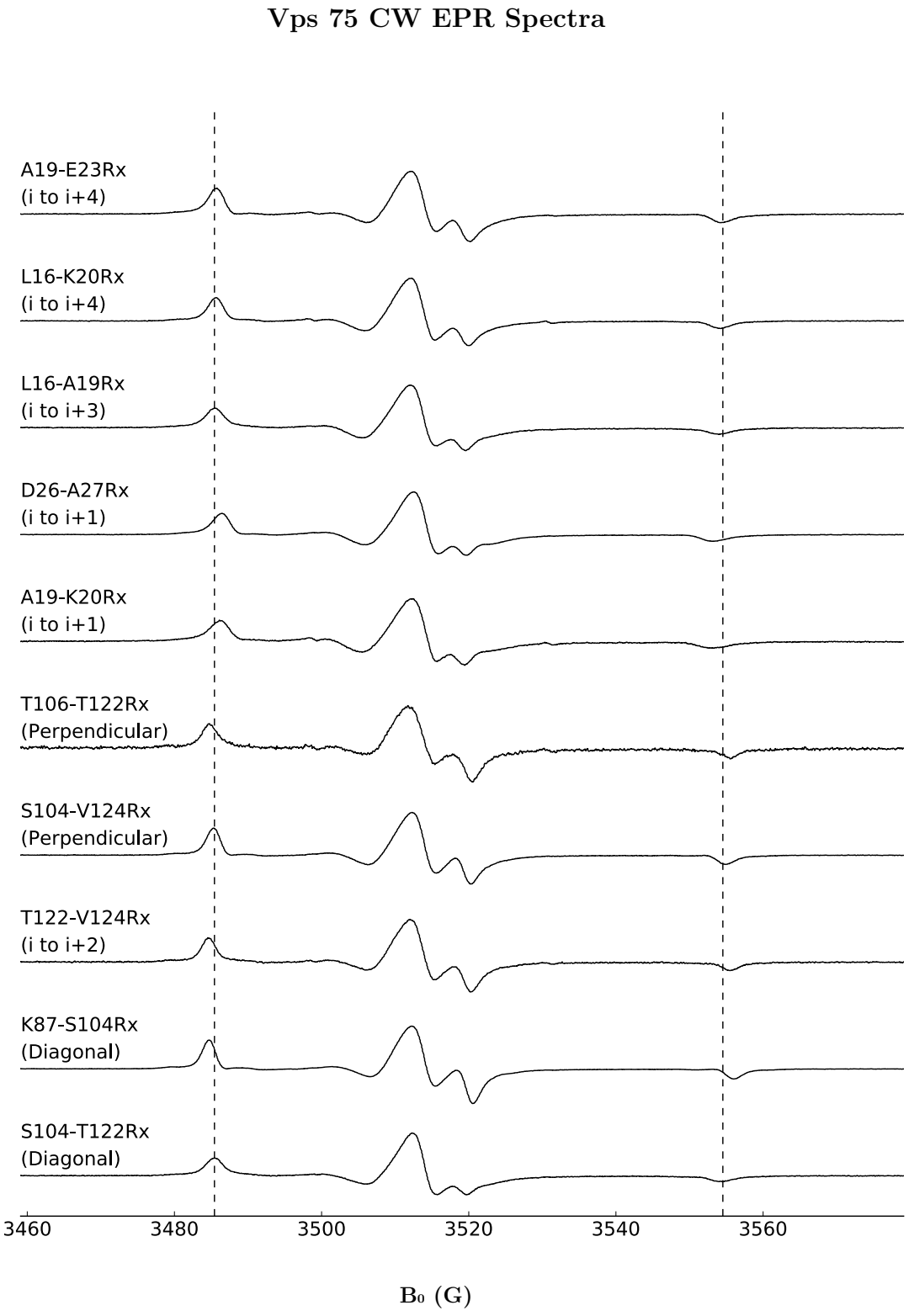

Figure S7.3: CW-EPR spectra of Rx bound to Vps 75, with dashed lines representing average positions of the low field peak or high field trough.

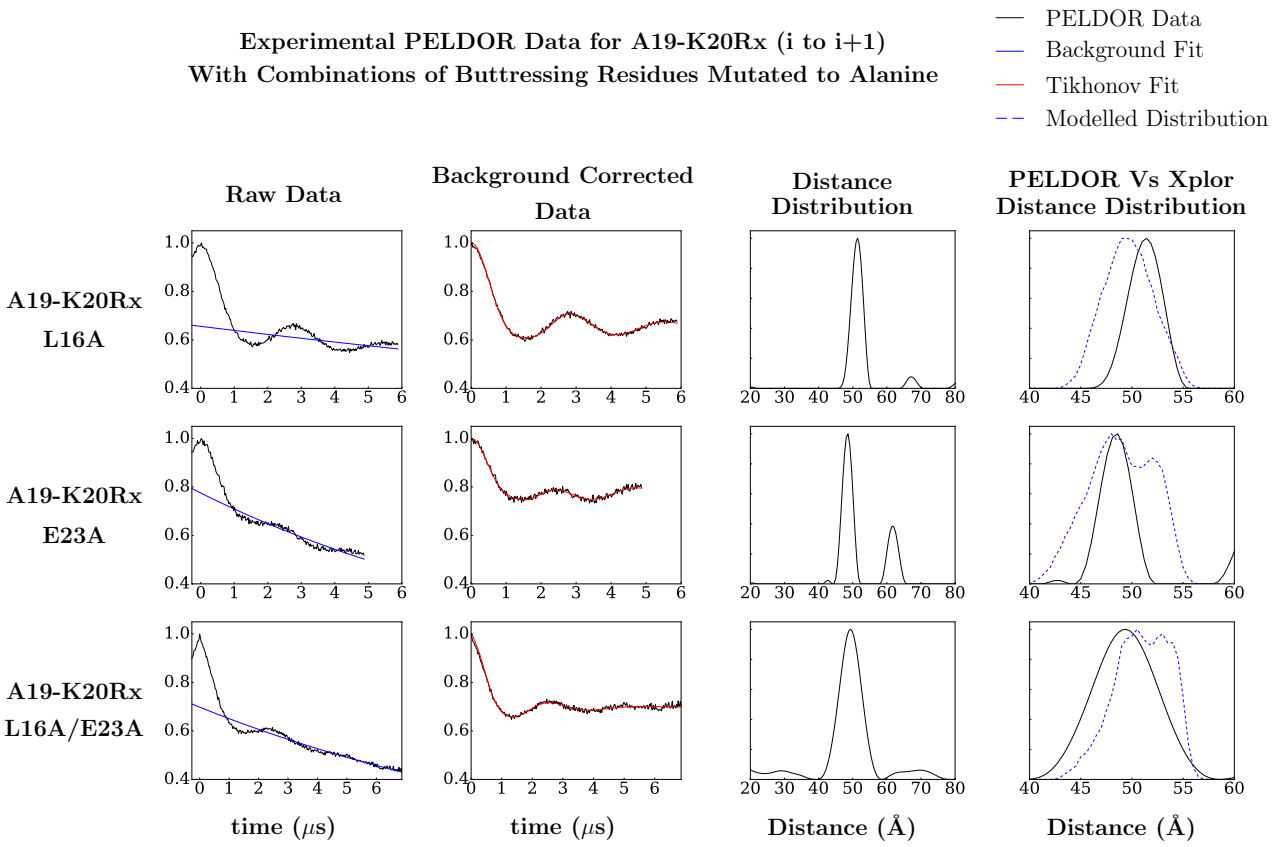

Figure S7.5: Raw data, background corrected data, and the distance distribution derived from PELDOR data of the A19-K20Rx buttressing residue mutations alongside the comparison between distance distributions of Rx modelled onto the Vps 75 crystal structure and the PELDOR distance distribution. The raw PELDOR data along with results from background correction and the Tikhonov fit are displayed as solid black lines, the background correction as a solid blue line, the Tikhonov fit as a solid red line, and the modelled distance distribution is displayed as a dashed blue line.